Spatial Analysis of Volcano Distribution in the Hawaii-Emperor Seamount Chain

SMITH, ALEXANDER,PATRICK,WILLIAM

Spatial Analysis of Volcano Distribution in the Hawaii-Emperor Seamount Chain

Alexander Patrick William Smith

Supervisors:

Prof Colin G. Macpherson

Prof. Kenneth J. W. McCaffrey

Department of Earth Sciences

Durham University

2023

This thesis is submitted in fulfilment of the requirements of the degree

MScR Geological Sciences.

Spatial Analysis of Volcano Distribution in the Hawaii-Emperor Seamount Chain

By Alexander Smith

Abstract

The distribution of ocean island Volcanoes is a topic surrounded with much uncertainty. We employ spatial recognition algorithms utilising the Hough Transform to determine the best fitting geometry of the Hawaii-Emperor Seamount Chain. Through the use of statistical analysis algorithms such as the Akaike Information Criterion (AIC), we demonstrate that the best fitting geometry of these seamount chains is a segmented great circle, in comparison to single and segmented small circle distributions, both of which have previously been proposed as a best fitting model. We show that the Hawaiian Chain is segmented into 10 great circles, and the Emperor Chain, is best described by 5 great circles. We also identified through the use of the AIC, that the Emperor Seamount chain is significantly better fitted to a segmented great circle distribution in comparison to the Hawaiian Chain. After consulting plate reconstructions, we propose that the segmentation of the Hawaiian Emperor seamount chain is influenced by tectonic events at the edge of the Pacific plate which are contemporaneous with ocean island magmatism, which we refer to as 'neo-tectonic events'. These neo-tectonic events are believed to affect the stress regimes within the plates, for example over the Hawaiian mantle plume. This can then lead to a preferential area for the intrusion of magma into the oceanic lithosphere, creating these focused zones of magmatism we observe as segmented great circles. We also show that controls which may be linked to the creation of segments are not linked to the formation and creation of seamounts and that these are likely to be under the influence of local forces such as gravitational loads. Finally, we note that due to the complexity, intricacy and lack of data surrounding the Hawaii-Emperor Bend, our model may not be the best fitting for this part of the Seamount Chain.

Table of contents:

List of Figures

Declaration

All of work that is within this thesis has been completed solely by the author and has not been submitted elsewhere unless referenced otherwise in the text.

Chapter 1. Introduction

1.1 This Spatial Distribution of Volcanism:

The genesis of ocean island volcanic chains is a topic of much debate, with a range of arguments advocating either for a plate control model or a plume model for the creation of these volcanoes. Spatial relationships between volcanoes have previously been used in a multitude of ways to shed light on reasons as to why volcanoes form where they do. On a broad scale, the identification of spatial relationships between volcanoes helps to identify the volcanic setting as well as the main driving forces behind the volcanism in this setting (i.e. arcuate and along a plate boundary for arc island volcanism, or linear, within the centre of a tectonic plate, for ocean island volcanism). On a finer scale, spatial relationships between volcanoes are able to shed light on the smaller processes which control where a volcano is formed locally within its unique volcanic regime. The spatial relationships between volcanoes can then, in turn, prove to be a very helpful tool in identifying the processes which have caused these volcanoes' genesis. If the expected shape of volcanism related to certain geodynamic processes within a volcanic setting is known, then comparisons can be drawn between what might be expected and what is actually observed. This, in turn, allows for hypotheses to be drawn as to the genesis of individual groups of volcanoes that share a spatial relationship. This project aims to explore the spatial relationships of the volcanoes in the Hawaii-Emperor seamount chain using quantitative techniques and provide an explanation for the driving/controlling processes which might influence the distribution of these volcanoes.

1.2 Geodynamic hypotheses for intraplate volcanism:

A common assumption within Earth Sciences is that the formation and location of ocean island volcanoes a controlled by mantle plumes and processes within the mantle Morgan, (1971, 1972a, 1972b). However, there are many other alternative explanations for ocean island volcanism such as the structure lithosphere or alternatively the stresses within the lithosphere. This section lays out the multiple standing hypotheses for intraplate volcanism

as well as laying foundations for the area of study and methods used for this study as a whole. Many theories have been proposed in order to explain the geodynamics of intraplate volcanism, some of which include mantle plumes, lithospheric extension, and the reactivation of ancient faults. The ongoing scientific debate surrounding this area reflects the complexity of the processes which drive intraplate volcanism and further emphasises the need for further research.

1.2.1 Mantle Plume Hypothesis:

Our area of interest, the Hawaii-Emperor Seamount Chain, is a series of volcanoes and seamounts located within the middle of the North Pacific Ocean. Its location within the Pacific Plate clearly demonstrates that its volcanism is unrelated to the Pacific plate's active plate boundaries. The controls and sources of such volcanism have sparked much interest into how this long chain of seamounts has formed. There are many theories as to how seamount chains form, however the most widely accepted of these is that when tectonic plates move over mantle plumes they leave behind a trail or chain of volcanoes on the Earth's surface Wilson, (1963) Morgan, (1971, 1972a, 1972b) Figure 1.1. Morgan argued that these plumes result from rising thermal currents originating deep within the mantle, and these currents promote the rising of ancient mantle material. This material will then partially melt, and the magma produced here rises through fractures or conduits, erupting through vents, forming the tholeiitic parts of the Hawaiian Islands.

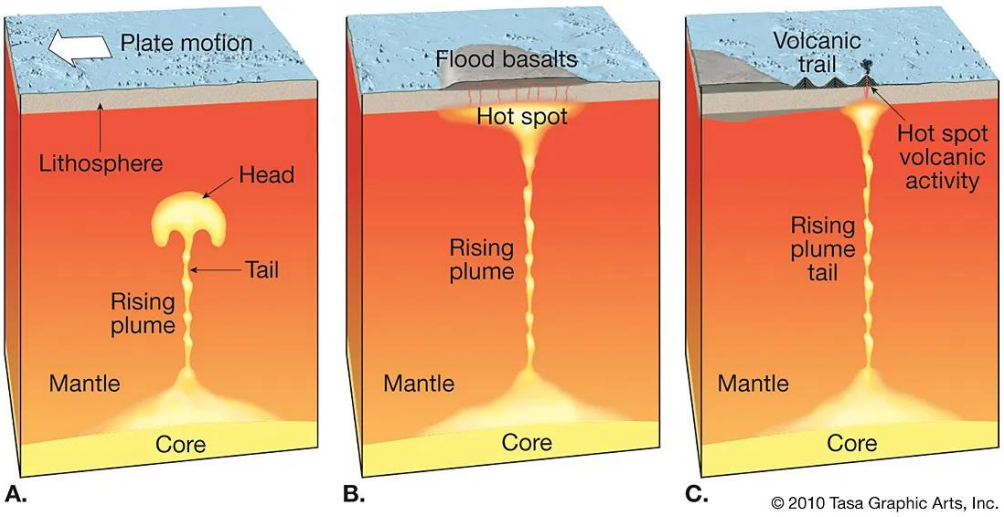

Figure 1.1: A schematic showing the genesis of ocean island chains, from (a) the rising of the mantle plume over a moving tectonic plate (b) the formation of Large Igneous Provinces (c) and the creation of a linear volcano chain (https://exploringtheearth.com/2013/05/25/galapagos_islands/)

Morgan (1972a) calculated that as few as 20 mantle plumes exist within the mantle. Morgan's initial hypothesis has been developed by many authors over time into a multitude of explanations for the origin of Ocean island volcanism. For example, Steinberger, (2000) later proposed that there are in fact 44 hot spots/mantle plumes each of which have been attributed to separate ocean island tracks/chains, and Clouard and Bonneville (2001) have discovered that there are 14 Pacific hotspots , of which 4 are fed by deep mantle plumes. Courtillot et al., (2003) had a deeper look into the origin of mantle hotspots and resulting from this, distinguished three types of hotspots within the Earth. They found that from a list of >40 hotspots, only 7 actually met the criteria laid out to be from a deep mantle origin, of which Hawaii, Louisville and Reunion were included. The criterion Courtillot et al, (2003) used consisted of: the presence of a linear chain of volcanoes with monotonous age progression; that of a flood basalt at the origin of this track; a large buoyancy flux; consistently high ratios of the three to four isotopes of helium; and a significant low shear wave velocity in the underlying mantle. The second type of hotspot they attribute to the transition zones at the top of superswells, and the final type they believe to be related to

upper mantle features and plate structure changes. This study poses interesting questions surrounding the geodynamics of the mantle and emphasises the further work required to understand these problems.

Experimental studies have been carried out to further understand how mantle plumes behave. Schubert et al. (1989); Olson and Christensen (1986); Whitehead (1982)and Griffiths and Campbell (1990) utilised rising coloured oil in a column of water or a combination of ethyl alcohol and sucrose to explore the pulsing of a mantle plume within its conduit. These studies have discovered that the initial formation of a conduit initiated with a large rising ‘diapir’, representing the plume head. What was also recognised was that this conduit comprised of large amplitude waves propagating upwards at a similar speed to the ‘plume head’, as can be seen in Figure 1.2. A critical ‘release’ size is attributed to these propagating waves within the conduit, where the source region has a conduit too narrow to transport all the material being channelled to it, leading to the growth of a diapir until its release at a critical size. The rising diapir from this conduit has been attributed to the ‘head’ of volcanic chains and formation of Large Igneous Provinces (LIPs) Richards et al., (1989) and Weis et al., (2011).

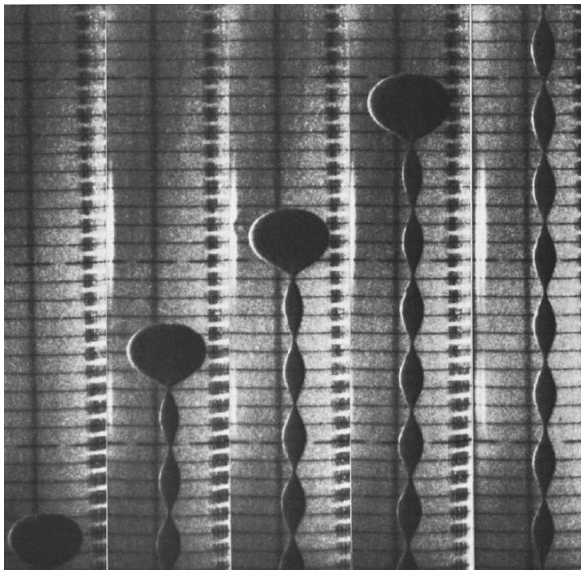

Figure 1.2: A sequence of images taken from Olson and Christensen, (1986), demonstrating an experimental approach utilising ethyl alcohol in a highly concentrated sucrose solution. This experiment aimed to further develop the origins and propagation of mantle plumes as well as provide an explanation for the evident pulsing made clear from this experiment.

More recently, studies into mantle plumes and hotspots encompass computer modelling such as Hieronymus and Bercovici (2001)'s insights into spacings of volcanic edifices as well as Olson and Yuen, 1982; Ballmer et al. (2011) studying the entrainment of material into mantle plumes, outlining the idea that mantle plumes are thermochemical plumes and not solely thermal plumes. Koppers et al. (2021) review multiple theories surrounding the formation and evolution of mantle plumes through their ascent within the mantle. They mention how mantle plumes take millions of years to propagate to the surface of the lithosphere to create hotspots. Furthermore, Koppers et al. (2021), explores, in detail, the shapes and stabilities of thermochemical plumes rising through the mantle, as opposed to how many geodynamic models represent them as vertical-axisymmetric plume.

Overall, mantle plumes and the hypotheses surrounding them prove to be an aspect of the Earth's geodynamics which provides ample opportunity to further understand the long-term evolution of the Earth's structure and dynamics. However, as Natland and Winterer (2005) state that the 'hypothesis of plates moving over fixed plumes is strongly dependant on

the perceptions of alignment of volcanoes' along their chains. Mantle plumes therefore should without doubt be the subject of further research to fully understand their role within the mantle and the Earth.

The mantle plume hypothesis is most easily described as a magmatic upwelling at a (mostly) fixed point over which a lithospheric 'cap' rotates or moves. The expected shape of a volcanic chain which has been derived from this process would be a small circle. This is because, it is understood that a mantle plume remains mostly stationary (a fixed spot). As a lithospheric cap moves over this plume, the cap would rotate around its own rotational axis. A single point which would be rotating on a cap of a sphere (or globe) would follow the shape of a small circle. The radius of this small circle is reliant upon the location of the lithospheric cap's axis of rotation, where the closer the axis of rotation is to being perpendicular to the axis of magma upwelling, the greater the small circle radius. The only exception to this is in cases where the rotation of the cap is perpendicular to the axis of magma upwelling, when the volcanic chain would have a radius similar to that of the Earth, creating a great circle distribution of volcanoes.

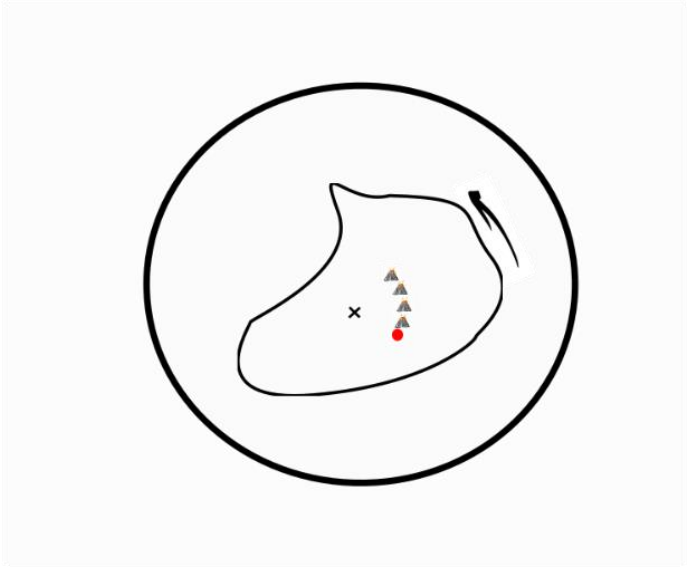

Figrue 1.3: Schematic showing how a rotating cap (obscure shape) rotating (in direction shown by arrow) over a mantle plume, represented by a red circle is able to produce a small circle

distribution of volcanoes (arc or segment of circle), about the cap's axis of rotation shown by the cross.

1.2.2 Plate Structure Hypothesis:

An alternative explanation of intraplate volcanism is focussed on the form or structure which the lithosphere takes. This plate structure-oriented explanation can encompass variations of the plates' architecture, thickness or composition. We explore each of these aspects of plate structure and the effects in which they have in causing melting anomalies or ocean island chains.

Lithospheric thickness appears to exert a significant level of control over the distribution of intraplate volcanism, with correlations between volcano spacing and lithospheric thickness having been found (Brink, 1991;Hieronymus and Bercovici, 1999). A thinner lithosphere allows a greater amount of magma within the mantle to rise to fill these undulations or thinner regions within the lithosphere. An increased amount of magma within the mantle rising results in adiabatic/decompression melting to occur here resulting in a greater expected volume of volcanism in these areas White, (1993); Keller et al., (2000); Regelous et al., (2003); Niu, (2021). A thicker lithosphere, however, will cause less volcanism as less adiabatic melting is occurring White, (1993). Since this hypothesis has been proposed, it has been widely accepted as being the leading cause of fluctuations in volumes of volcanism, although Harrison et al (2017) oppose this as being a primary cause of volcanism. They state that 'high degrees of melting will result in lavas … with lower radiogenic Pb' and in this study they were unable to find a correlation between radiogenic Pb and lithospheric thickness along the North West Hawaiian Ridge, which would have been expected if lithospheric thickness did influence the volume of magma erupted.

Lithospheric erosion builds upon the idea that a thinned lithosphere leads to an increased volume of erupted magma. Concepts based upon the mantle's dynamics, such as mantle plumes and convection, have been used to explain why we may observe thinned areas

of the lithosphere. Using a numerical model of the mantle's dynamics beneath Hawaii, Ballmer et al. (2011) find that, small scale convection-cells (Figure 1.3) are able to erode away the base of oceanic lithosphere, creating a 'washboard topography' on the underside of the plate. These varying thicknesses within the lithosphere then facilitate a larger amount of adiabatic melting, which in turn allows for increased levels of volcanism. The likely pattern in which volcanism is expected to arise resulting from this geodynamic model would consist of a line of volcanoes, aligning parallel with the 'washboard topography' produced by the small-scale convection-cells. Other plate structures are expected to produce different shapes of volcanism. For example, if lithospheric thickness was a leading driver for the production of ocean island volcanoes, it would be expected that they would appear to be concentrated to the areas where lithosphere is at its thinnest.

The composition and type of the lithosphere also controls the volume of magma erupted Davies et al., (2015). However, this particular element of this hypothesis is not entirely relevant to this project as the area of study lies entirely on Pacific oceanic lithosphere, hence it is beyond the scope of this project to explore this this in further detail.

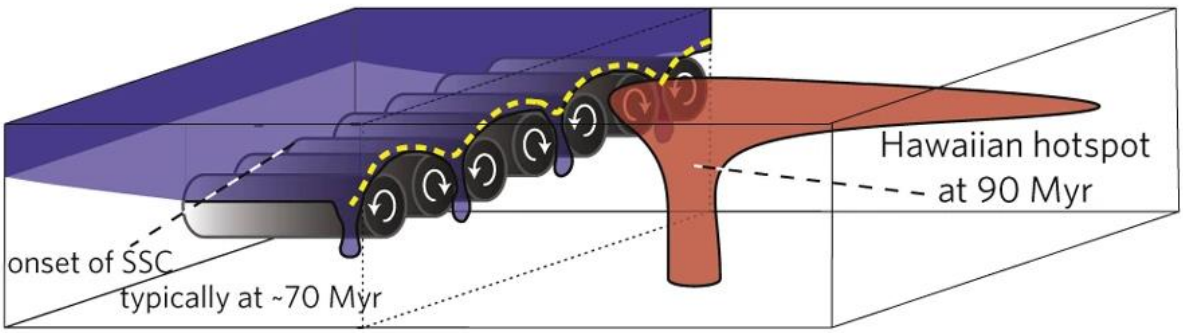

Figure 1.3: Schematic representation of how small-scale convection cells may appear within the mantle, as well as interact with the lithosphere and mantle plumes Ballmer et al., (2011). The yellow dashed line represents the 'washboard topography' on the lithosphere which these convection cells make.

1.2.3 Plate Stress Hypothesis:

This hypothesis draws on similar ideas to the plate structure hypothesis, in particular the idea that, local, regional, and large-scale stresses all have a control in the formation of linear volcanic chains. James Dwight Dana initially identified the alignment of seamounts along the Hawaii-Emperor seamount chain in 1849. Dana explained ocean island volcanism as resulting from en-echelon fractures which allow magma to create conduits and reach the surface, facilitating the emplacement of volcanoes on the surface of the lithosphere, demonstrated by figure 1.4.

Additionally, Michon et al. (2007) builds upon previous work by Le Gall et al. (2004), attributing lithospheric uplift from mantle processes to the reactivation of ancient faults, leading to a preferential input into the location of volcanic edifices. This theory has been explored on a large scale and improved upon over many years, eventually incorporating hypotheses such as plate stresses, cooling and contraction of the lithosphere, pre-existing geological features, cracks resulting from plate stresses or even ancient rift zones and fractures Turcotte and Oxburgh, (1973); Anderson, (2000) and Clague et al., (1989).

Through the concept of differential motion of intra-lithospheric sheets (lithic sheets/layers which make up the entirety of the lithosphere and are able to move independently of one another) as well as the comparison of morphologies of structural assemblages and their development in both continental and oceanic lithosphere, Utkin (2006) showed that strike-slip faulting has a major control over the formation of volcanic belts within the Pacific plate, between the Darwin Rise and the Polynesian rise such as those within the Pukapuka Seamount Chain.

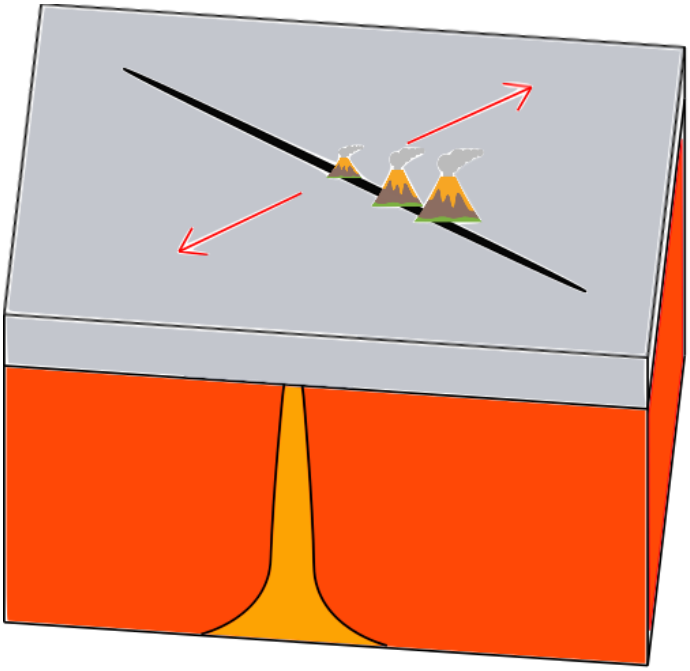

Figure 1.4: A schematic demonstrating tensional stresses (shown by red arrows) creating a fracture zone or crack in oceanic lithosphere (in grey). The mantle or a rising plume is then able to exploit the weakness in the lithosphere, creating ocean island volcanoes. It is worth noting that the illustrated fracture zone is represents a weakness in the lithosphere at an unspecified depth (not the entire thickness of the lithosphere). This weakness is able to be exploited by magma asynchronously to create conduits through the lithosphere forming volcanoes.

It has been found that the formation of rift zones results from gravitational forces and stresses within individual edifices and is not majorly affected by regional stresses (i.e. stresses within the oceanic lithosphere which are spread much more widely, and on a larger scale than stresses such as those impacted by gravitational loads) Fiske and Jackson, (1972) if not otherwise influenced by neighbouring volcanoes Jackson and Shaw, (1975). However, there are numerous seamount chains (Louisville, Foundations, Gilbert, Caroline, Pitcairn, Macdonald amongst others) within the Pacific Ocean which are aligned mostly parallel to the Hawaii or Emperor seamount chains Rose and Koppers, (2019), and from this observation conclusions have been drawn that a uniform regional stress is influencing the positioning of

all of the chains in the Pacific Ocean MacDonald, (1955). These findings suggest that gravitational stresses exert control over ocean island volcanism at a ‘smaller’ scale such as seamount shape, morphologies, and formation of rift zones, whilst regional stresses exert control over ocean island volcanism at a significantly ‘larger’ scale such as the spatial distribution and alignments of volcano chains.

Finally, there has been much disagreement over this hypothesis, with many suggesting that the linear nature of seamount chains is more consistent with a mantle plume model Richards et al., (1989). However, Perez-Torrado et al. (2023) explore the idea that the spatial distribution of the Fuerteventura and Lanzarote volcanoes in the Canary islands (thought to have been formed as a result of hotspot volcanism) result from a propagating fracture, causing the observed direction of development between these edifices. Although there is not a clear age progression between volcanic edifices in the Canary Island volcanic chains, the directional development of these edifices along a propagating fracture has the potential to be explored in other volcanic chains which demonstrate strong directional development between volcanic edifices such as the Hawaii Emperor Seamount Chain. The uncertainty surrounding this hypothesis only serves to reinforce the significant uncertainties surrounding the genesis of ocean island volcano chains, emphasising the need for further investigation into local and regional plate lithospheric stresses.

Each three of these hypotheses predict a different spatial relationship between ocean island volcanoes. The mantle plume hypothesis predicts that ocean island volcanoes would be fitting a small circle distribution. The plate structure hypothesis predicts that, spatial relationships of volcanoes would line up with differences in the plate structure (i.e. where there is thinning of the lithosphere volcanoes would be built more preferably. Finally, the plate stress hypothesis, is able to predict that volcanoes are built and exploit weaknesses in the lithosphere brought about by changes in stress regimes (either on a large ‘regional’ scale or a small ‘local’ scale). Ways in which these predictions could be tested is through comparing with examples which may occur naturally, or to create geodynamic models which simulate the hypotheses

above and comparing whether the outputs of this model are similar to the predictions made about the spatial relationships of the volcanoes which are built with these mechanisms.

1.2.4 Multiple Geodynamic Processes Constructing Ocean Island Volcanoes?

Ultimately, these three hypotheses for the formation of ocean island volcano chains are all viable explanations of intraplate volcanism, and the likelihood that more than one of these contributes to building an individual volcanic island chain is very high. Figure 1.5 has been created as a visual aid to show how the construction of different volcanic chains may be influenced by more than one of the geodynamic processes previously mentioned. This diagram consists of 3 ‘endmembers’ (Plume, neo-tectonic and palaeotectonic) which each represent a separate influence over the spatial distribution of ocean island volcanism. We use the term neo-tectonic processes to refer to tectonic events which occur contemporaneously with magmatism which has the potential to lead to a change in distribution of ocean island volcanoes. Palaeotectonic controls over the spatial distribution of ocean island volcanism refer to significantly older or ancient seafloor features which may influence the distribution of ocean island magmatism. With this knowledge, we are able to qualitatively position different individual ocean island volcano systems on different areas on this graph based off of what is currently understood to be the main influences of the genesis of these ocean island volcanoes.

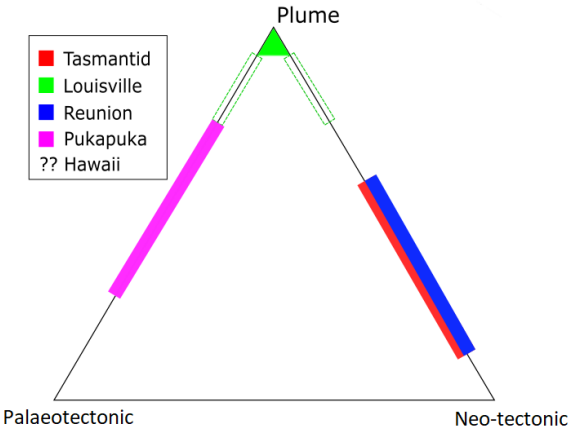

Figure 1.5: 'End-member' diagram, demonstrating the ways in which different geodynamic controls may have a primary or partial influence over the formation of separate, independent ocean island seamount chains Peive, (2007); Cheng et al., (2013); Richards et al., (2018). Bars along the edges of the triangle represent an ocean island volcano chain that is understood to be under the influence of the geodynamic controls at either end of that line (for example the reunion chain is believed to be under the control of both a mantle plume and Neo-tectonic processes). Those areas which encompass the centre of the triangle are done so qualitatively as there is not enough certainty or data at present to be able to definitively determine the extent by which certain geodynamic processes influence the building of volcanoes at a certain ocean island chain.

Both the plate structure and plate stress hypotheses are predicated upon the theory that either pre-existing features or other factors such as stresses have an influence on the formation of volcanic ocean island chains. Volcanic features which occur as a result of the processes described in these hypotheses are expected either to follow a similar overall shape to the structure of the lithosphere or to follow the orientation of the specific lithospheric plate stresses that they are exploiting.

1.3 Spatial analysis and observations of volcanic features:

1.3.1 Hough Transform spatial analysis:

The Hough Transform, an analytical transformation used in this project (Appendix B.1), which was initially set out to extract and identify geometrical features from images., Duda and Hart, (1972). Within Earth Sciences the Hough Transform has previously been utilised to identify aligned points within spatial datasets i.e. lines. For example, over time there have been multiple attempts to constrain the alignment of volcanic features utilising the Hough Transform, one example of which is the identification of alignments within volcanic fields Wadge and Cross, (1988); Von Veh and Németh, (2009); Cebriá et al., (2011). Both Pacey et al (2013) and Andikagumi et al. (2020) built upon this work and have identified, using the Hough Transform approach, great circle segmentation in both the Sunda and Mariana arcs respectively, as can be seen in Figure 1.6. This has led to the conclusions that these linear volcanic segments in volcanic arcs can be attributed to weaknesses of the lithosphere, allowing a much easier route for magma transport, leading magmatic pathways to align.

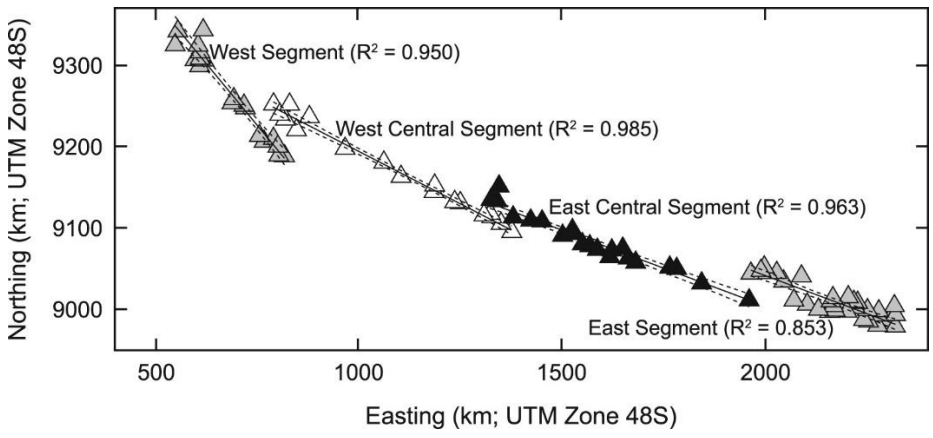

Figure 1.6: Diagram taken from Pacey et al (2013) demonstrating the alignments and segmentation found within the Sunda Arc utilising the Hough Transform approach. Where, black lines represent individual segments identified, triangles of differing colours represent volcanoes sitting on separate segments, R^2 values represent values for the least squares

regression for each identified segment and dashed lines represent the 95% confidence interval for the least squares regression.

1.3.2 Volcanic Rift zones:

One very distinct feature of Hawaiian volcanism is volcanic rift zones. Rift zones are areas of prolonged fissure eruption along the flanks of a volcano, creating large elongate structures composed of multiple dykes Nakamura, (1982); Walker, (1999); they tend to diverge radially from a centre point (i.e. a magmatic centre) with around a 120° separation MacDonald, (1955), as seen in Figure 1.6.

There has been a lot of work focusing on the formation of rift zones on volcanoes. For example, Fiske and Jackson, (1972) explore how regional and gravitational stresses have impacts on the orientation and growth of rift zones in Hawaiian volcanoes whilst Klügel et al., (2005) investigated the internal structure of rift zones and how gravitational stresses affect the formation of dykes within them. These studies found that both regional and local stresses have a major impact on the formation of rift zones. Fiske and Jackson showed that 'isolated' edifices which grew on their own (away from other nearby volcanoes) tend to have rift zones which align with the general trend (overall azimuth) of the Hawaiian Archipelago (Figure 1.7), whereas 'clustered' edifices were greatly affected by regional stresses causing their rift zones to form at a more oblique angle with the general trend of the Hawaiian Archipelago (Figure 1.8).

As volcanic rift zones are composed of swarms of dykes, gaining a deeper understanding of the formation of dykes can prove to be beneficial to the understanding of how volcanic rift zones are built. It is therefore important to further understand the formation of dykes within rift zones. It is believed that deep faults form where at the points where the volcano contacts the weak oceanic sediment layer. These faults allow the volcano to continually adjust to additional and new intrusions of magma as well as create the correct

stress patterns for continued propagation of dykes along the rift zones axis Nakamura, (1982); Dieterich, (1988).

1.3.3 Double trend Seamount chains:

Another distinctive feature of ocean island volcanism and the Hawaii-Emperor seamount chain is that, towards the youngest end of the Hawaii-Emperor seamount chain, there are what appear to be two separate, geochemically distinct chains of volcanoes, referred to as the Loa and Kea trends Jackson et al., (1972); Hieronymus and Bercovici, (1999) Figure 1.9. These two chains of volcanoes are thought to sample the same part of the mantle Harrison et al., (2017). However, these two volcanic chains appear to have different Pb isotope systematics, as identified by Tatsumoto, (1978). This has raised questions surrounding what processes may be affecting the Hawaiian mantle plume in order to lead to this varying isotopic trend.

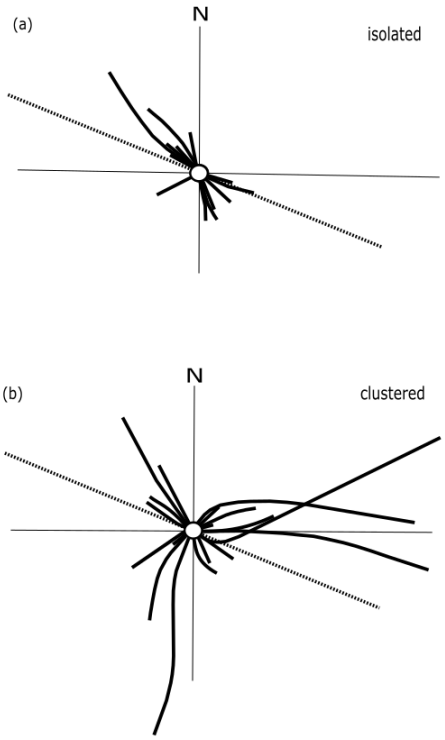

Figure 1.7: Rose diagrams showing the orientation of rifts belonging to 'clustered' and 'isolated' volcanoes (solid black lines) in comparison to direction of plate motion (dashed line). Taken from Fiske and Jackson (1972).

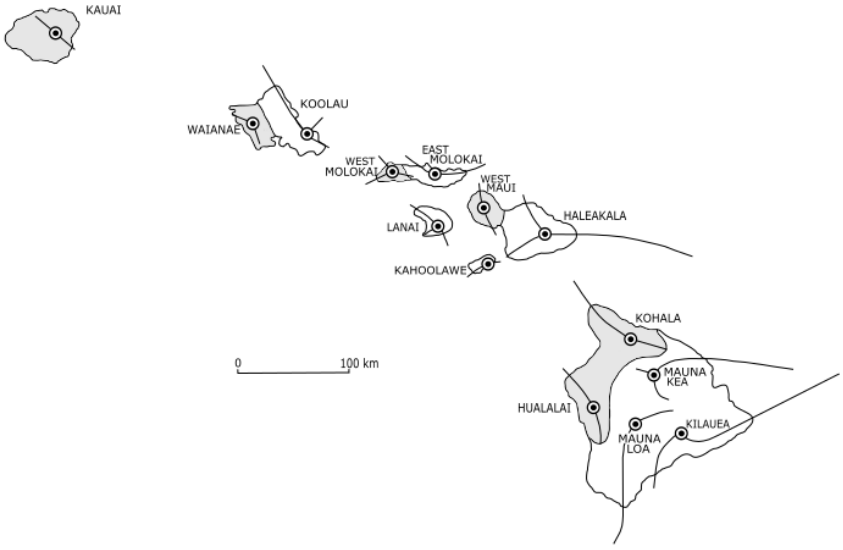

Figure 1.8: Map of the Hawaiian archipelago, outlining 'isolated' volcanoes (shaded) as ones which form before 'clustered' volcanoes, along with their rift zones. Taken from Fiske and Jackson (1972).

One explanation for the formation of two spatially separate chains of volcanoes draws on the idea that flexure and stresses within the lithosphere can influence the creation of a double chain. It is thought that the double trend occurs because compressive forces from a volcanic load placed off the hotspot axis limit the formation of another volcano on the same side of the hotspot axis, forcing the next volcano to be formed to be on the opposite side of the axis Hieronymus and Bercovici, (1999); Hieronymus and Bercovici, (2000). Hieronymus and Bercovici (1999) then attribute a separate geochemistry in the volcanoes to the two volcanic lines sampling different parts or sides of the mantle plume. This idea has been built upon by Harrison et al. (2017) where the rising mantle plume is sampling heterogeneities within the mantle source, causing variations within the chemistries of lavas erupted in the Hawaiian Islands. Harrison et al. (2017) also explores the idea that the Hawaiian mantle plume which samples predominantly 'Kea type' magmas, incorporates an increasing amount of 'Loa type' magmas after the Hawaiian-Emperor Bend, and the 'Loa-Kea trend' is not just located at the youngest end of the Hawaii-Emperor Seamount Chain.

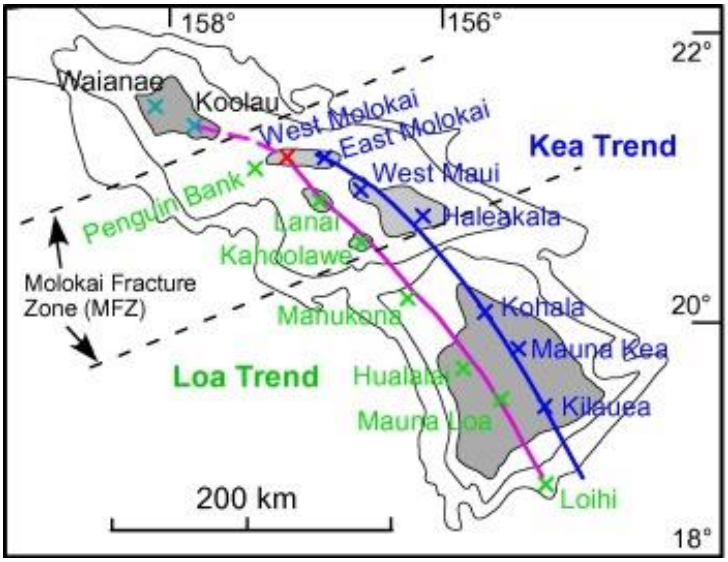

Figure 1.9: A map demonstrating the spatial distributions of the Kea and Loa trends within the Hawaiian Archipelago as well as noting the locality of the Molokai Fracture zones Frey et al., (2016).

1.4 This Study:

The Hawaii Emperor seamount chain is located in the North Pacific Ocean, extending >6000km from the main Hawaiian Islands to the Meiji and Detroit seamounts in the far north west of the Pacific ocean where the Pacific plate is subducting beneath the North American and Eurasian plates. Edifices are interpreted to be, for the most part, evenly spaced along the seamount chain Vogt, (1974). The Hawaii-Emperor Seamount Chain is often used as a 'textbook' example for ocean island volcanism due to its very clear age progression Clague and Dalrymple, (1973), and its 60° change in direction demonstrating what is thought to be a distinct change of plate movement at ~45Ma and at ~25Ma Jicha et al., (2018).

Uncertainty still currently surrounds the nature of volcanoes in marine intraplate settings, such as those in the Hawaii-Emperor Seamount Chain, and how the volcanoes along them are aligned. There have been multiple attempts to constrain the alignment of volcanism along ocean island Chains, stating that they are made up of multiple en-echelon 'loci' of individual shield volcanoes Jackson, et al (1972); Jackson et al., (1975); Jackson and Shaw, (1975). The primary issue with this is that these 'loci' appear to be qualitatively identified and added to the map, favouring points of highest elevation along the chain to be volcanic centres. The danger of this is that the location of ancient edifices, which have been the subject of both subaerial and submarine erosion, have not been fully considered Scott and Rotondo, (1983). The alignment of volcanoes, especially in an intraplate setting, is therefore an important area for further investigation using more quantitative approaches such as the Hough Transform method.

The spatial analysis of volcanic island chains proves to be a very useful tool, it aims to help identify trends in magmatic pathways/loci within the lithosphere to form ocean island seamount chains. The spatial trends identified between magmatic pathways can help inferences to be made regarding the formation of volcanic features. For example, both Pacey et al (2013) and Andikagumi et al (2020) utilised spatial analysis to determine that magmatic

loci within volcanic arcs best follow multiple great circle distributions. The use of great circles, in comparison to small circles will also be used within this study. We will utilise spatial analysis tools to determine the best-fitting geometries of ocean island volcanism within the Hawaii-Emperor Seamount Chain in order to evaluate current hypothesis for the genesis of ocean island volcanism and potentially propose a separate model for the controls over the distribution of this form of volcanism.

Building upon this previous work we are able to form the following aims for this project:

- To utilise tools to place quantitative constraints upon the spatial distribution of ocean island volcanoes along the Hawaii-Emperor Seamount Chain.
- To determine the best-fitting geometry of alignments identified along the Hawaii-Emperor Seamount Chain.
- To identify seafloor features which may have impacted or indicate the formation of multiple segments within the Hawaii-Emperor Seamount chain or lead to different observed seamount morphologies.
- To draw on previous research to build a geodynamic model which best explains an orderly, segmented, and aligned Hawaii-Emperor Seamount Chain, potentially providing a re-evaluation of mechanisms involved with the creation of ocean island volcanoes.

Chapter 2. Methods:

Throughout this project a variety of methods were used. Location data was collated in order to build an accurate spatial database of the Hawaii-Emperor Seamount Chain. Spatial recognition tools were used in so that alignments between seamounts within the Hawaii-Emperor Seamount Chain could be recognised. Morphologies of seamounts were analysed as a means to identify potential preferential forces or stresses which may have given rise to certain seamounts within the Hawaii-Emperor Seamount Chain.

2.1 Locating volcanic centres:

In order to create a database of locations for volcanic centres in the Hawaii-Emperor Seamount Chain an assumption has been made that the locus of volcanism is a valid representation of the main point of magma flux through the lithosphere. Pacey et al., (2013) were able to directly use digital elevation models to locate volcanic features, such as volcanic vents, indicating volcanic centres. In this project, the use of digital elevation models for the locating of volcanic features such as volcanic vents was not able to be done to the same accuracy. This was as a result of the vast submarine portions of the Hawaiian ridge which, being exposed to large amounts of erosion, make volcanic features indicating volcanic centres significantly more difficult to identify on bathymetric maps.

In order to map the submarine volcanoes more accurately along the Hawaii Chain, we built upon the idea that a common characteristic of Hawaiian volcanism is rifting Nakamura, (1982); Dieterich, (1988);Walker, (1999), in some cases, such as Kilauea and Haleakala, producing very distinct and long rift zones and submarine ridges. These ridges are distinct, being steep-sloped and having elongate features Nakamura, (1982). Utilising the ‘slope gradient tool on ArcGIS pro, the axes of submarine rift zones were able to be identified as those with the shallowest gradient. Figure 2.1 demonstrates how this ‘slope gradient’ tool was used to identify submarine ridges of West Northampton Bank Seamount, where the axes of three prominent rift zones, separated ~120º from one another are able to be followed along a path of minimal gradient. Using the strong topographic signature of the Hawaii-Emperor

Seamount Chain, and individual seamounts, the presence of rift zones and submarine ridges were able to be identified.

Confirming Jackson et al (1972)'s hypotheses, lines along volcanic rift zones were traced, showing that these rift zones can be followed back to their corresponding volcanic centres where they overlap with other rift zones (Figure 2.1). Given the repeatability of this method to be able to position all the subaerial Hawaiian volcano magmatic centres accurately (i.e., rift zones are able to be traced back to Kilauea's caldera/the peaks of Mauna Loa or Mauna Kea), this method was continued for the submarine portion of the Hawaii Emperor Seamount Chain. Singular points were used to represent volcanic loci/centres which were determined by the region in which rift zones and submarine ridges of individual seamounts overlap. Further to this, the bathymetric data acquired in the Northern Pacific Ocean surrounding the Hawaii Emperor Seamount Chain has also been used to identify 'cross chain features' which may have some relation to some form of underlying lithospheric structure or transform zones. These 'cross chain features' have been identified all the way along the Hawaii-Emperor Seamount Chain and are best described by well-defined and spaced sets of seamounts aligning oblique to perpendicular against the expected general trend of the Hawaii-Emperor Seamount Chain. Figure 2.2 demonstrates this spatial trend of 'cross-track' seamounts.

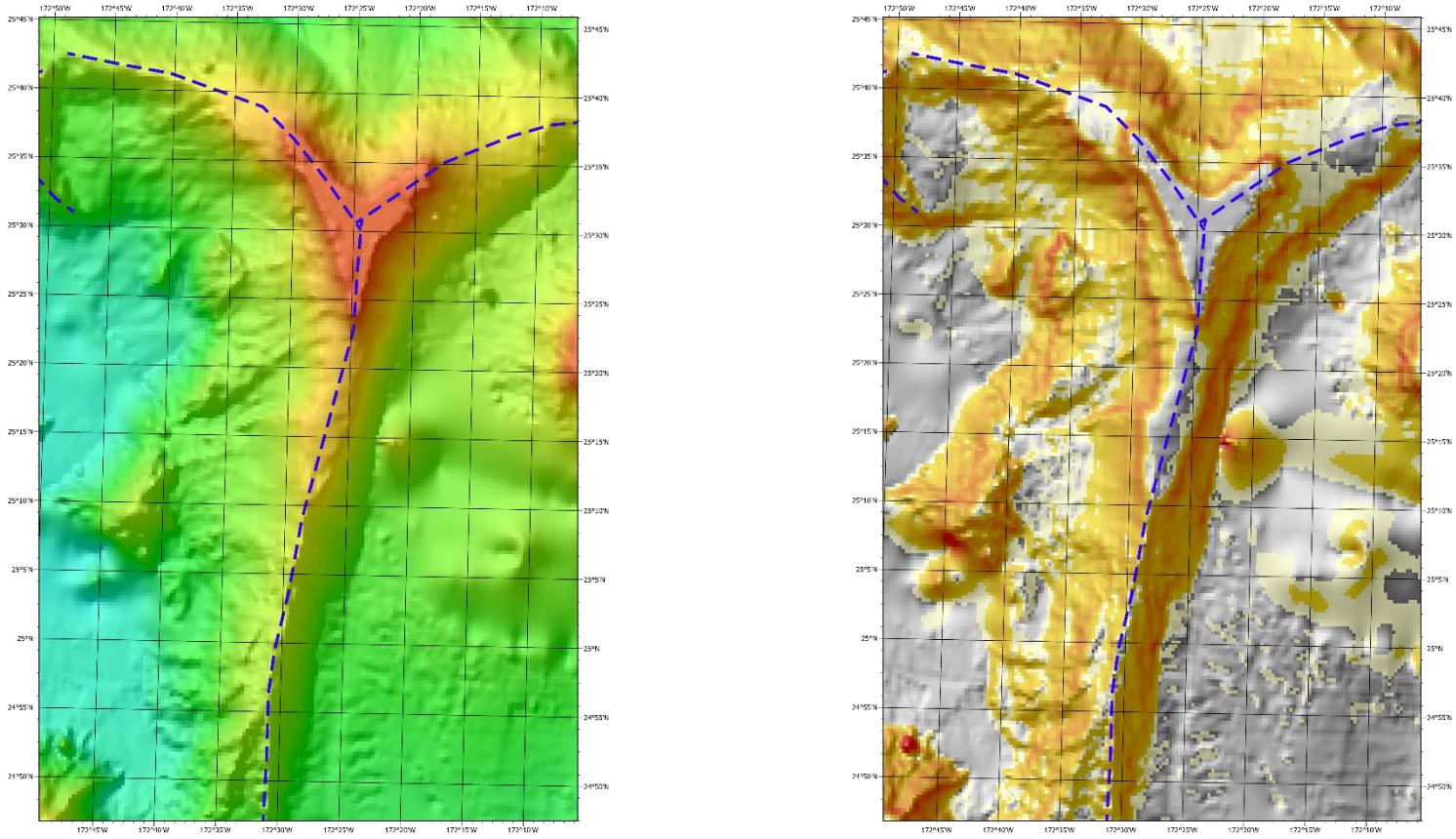

Figure 2.1: Map showing rift zones (blue dashed) on West Northampton Bank, converging back to its inferred volcanic centre (red triangle). Panel a, showing the gradient of the seamount and its surrounding area, enabling the rift zones to be more easily mapped. Darkest colours representing the steepest slope, and lightest representing the shallowest slope. Where there is no colour on top of the hill shade this represents gradients <5°. Panel b, showing the elevation of the seamount.as a simple colour gradient where Red is the shallowest and light blue the deepest.

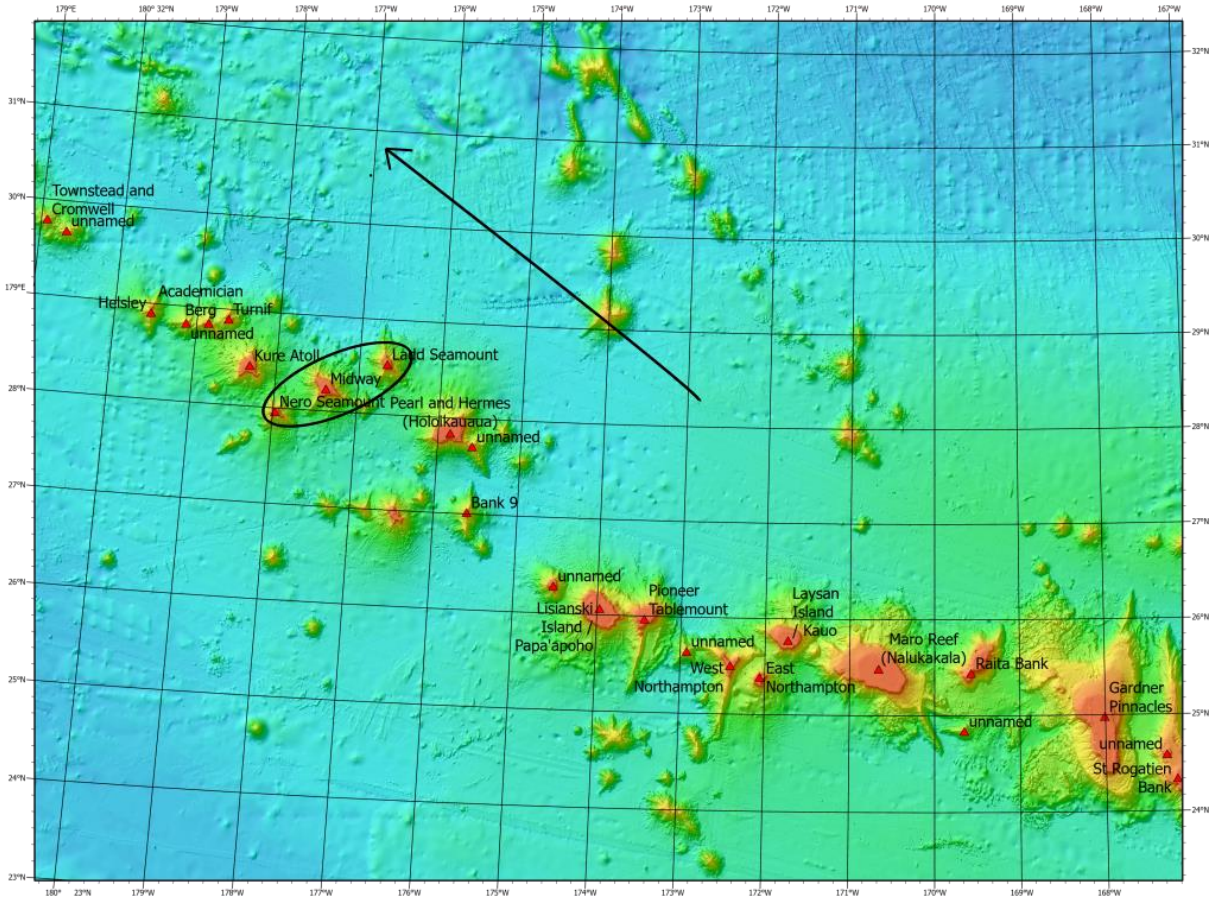

Figure 2.2: A map showing an example of the presence of ‘cross track seamounts’ within the Hawaii-Emperor Seamount chain. Red triangles represent individual volcanic edifices within the Hawaii-Emperor seamount chain. The arrow demonstrates the direction of which the general trend of the Hawaiian seamounts tend to follow (North-West). The circled seamounts are seamounts which sit along a point in the Hawaii-Emperor Chain, which is multiple seamounts wide, where the trend of these volcanoes is also significantly different to that of the entire Seamount Chain

Each individual seamount and volcano is then recorded as a single point, representing its underlying magmatic systems. In cases where bathymetric data is not at a high enough resolution to identify the rift zones, terraces formed by millions of years of marine erosion were used to distinguish youngest parts of seamounts. Additionally, in a few areas where bathymetry was not even this clear, a bathymetric high was used as the volcanic centre of the

seamount. The locations of all volcanic centres in the Hawaiian Chain used in this study can be seen in Figure 2.3 and are listed in Appendix A.

2.1.1 Seamount rift and elongation orientations:

Many studies have investigated the effects of regional stresses and plate structure on the morphology of seamounts. Chayton et al. (2007) explores the morphologies of seamounts within both the Kodiak-Bowie and the Cobb Seamount Chains. They argue that, in comparison to the other flat-topped circular seamounts, the formation of two anomalous elongate and linear seamounts is as a result of fossil transform faults and fracture zones which are at a similar orientation to their elongation. Additionally, Richards et al. (2018) explores the morphologies of the Tasmantid seamounts and their relation to a proximal extinct spreading zone. They discover a range of different seamount morphologies, each of which are found to correlate with the tectonic setting. Richards et al (2018) attribute elongate terraced and rugged seamounts to areas with strong brittle deformation such as fracture zones, conical seamounts to areas with less frequent faulting, and the single shield seamount present to thinned oceanic crust. These studies clearly highlight the importance of understanding the morphologies and shapes of seamounts when trying to understand the processes behind their formation, as it has been found that basement structure can have a significant influence on seamount morphology.

The study of seamount rift orientation and orientation elongation has greatly benefited previous research aiming to understand lithospheric controls over ocean island chains Richards et al., (2018). Similar to the work of Richards et al, the orientations of rift zones and principal axes of elongation for seamounts in the Hawaii-Emperor Seamount Chain were mapped by identifying the longest axes of seamounts (Figure 2.5), and then plotted against orientation of individual segments, as well as in one case against fracture zone orientation. This aims to distinguish if there are any trends along segments which could help to explain the segmentation of seamounts along the Hawaiian Chain.

2.2 The Hough Transform and Geometric Fitting:

In order to discover if the Hawaii Seamount Chain is aligned into great circle segments, the Hough Transform was employed. This study utilises and builds upon the same methods as Andikagumi et al. (2020) and Pacey et al. (2013), both of which are specific to volcanic arcs. This method aims to identify a potential alignment between volcanoes in the Hawaii-Emperor Seamount Chain through the application of the Hough Transform.

2.2.1 The Hough Transform:

The Hough Transform has been widely used in Physics, computer vision technology and in Earth Sciences in order to recognise geometric features in images. It is understood that in space, a line is described by two parameters, ρ and θ, the length of the normal of the line which passes through (0,0) and the angle which the normal makes with the x axis respectively. Using this idea, Duda and Hart (1972) are able to graphically show how the Hough Transform is able to effectively find best fitting alignments within images; this has been clearly illustrated by Pacey et al (2013) (Figure 2.4).

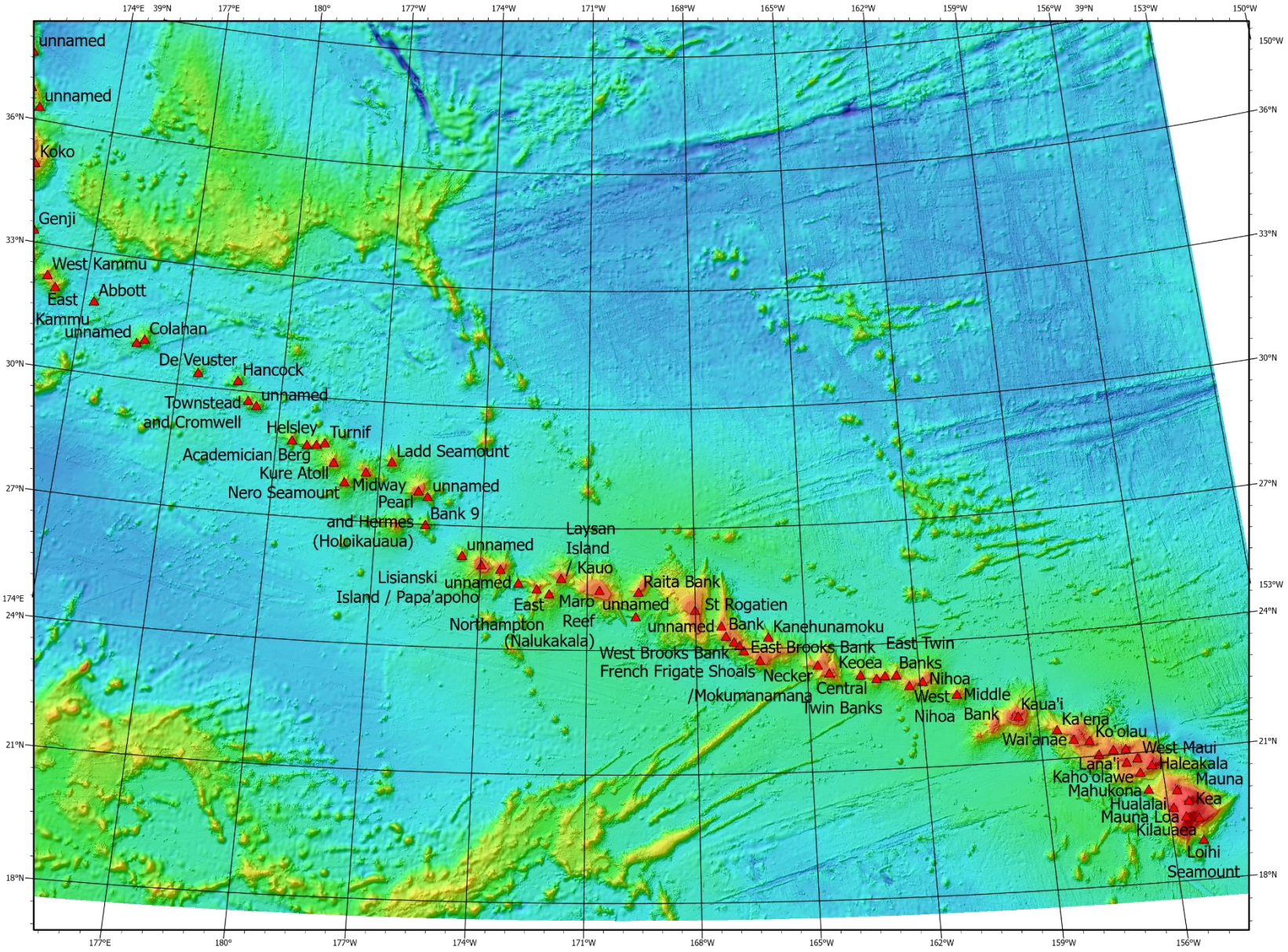
unnamed
unnamed
Koko
Genji
West Kammu
East Kammu
Abbott
unnamed
Colahan
De Veuster
Hancock
unnamed
Townstead and Cromwell
Helsley
Turnif
Academician Berg
Kure Atoll
Nero Seamount
Midway
Ladd Seamount
unnamed
Pearl and Hermes
Bank 9
(Holoikauaua)
unnamed
Lisianski Island / Papa'apoho
unnamed
Laysan Island / Kauo
East Maro Reef
Northampton (Nalukakala)
Raita Bank
unnamed
St Rogatien Bank
unnamed
Kanehunamoku
West Brooks Bank
East Brooks Bank
East Twin Banks
French Frigate Shoals
Necker
Keoea
Nihoa
Central /Mokumanamana
West Nihoa
Middle Bank
Iwin Banks
Kaua'i
Ka'ena
Ko'olau
Wai'anae
West Maui
Lana'i
Haleakala
Kaho'olawe
Mauna
Mahukona
Kea
Hualalai
Mauna Loa
Kilauaea
Loihi Seamount
150°W
36°N
33°N
30°N
27°N
24°N
21°N
18°N
153°W
174°E
177°E
180°
177°W
174°W
171°W
168°W
165°W
162°W
159°W
156°W

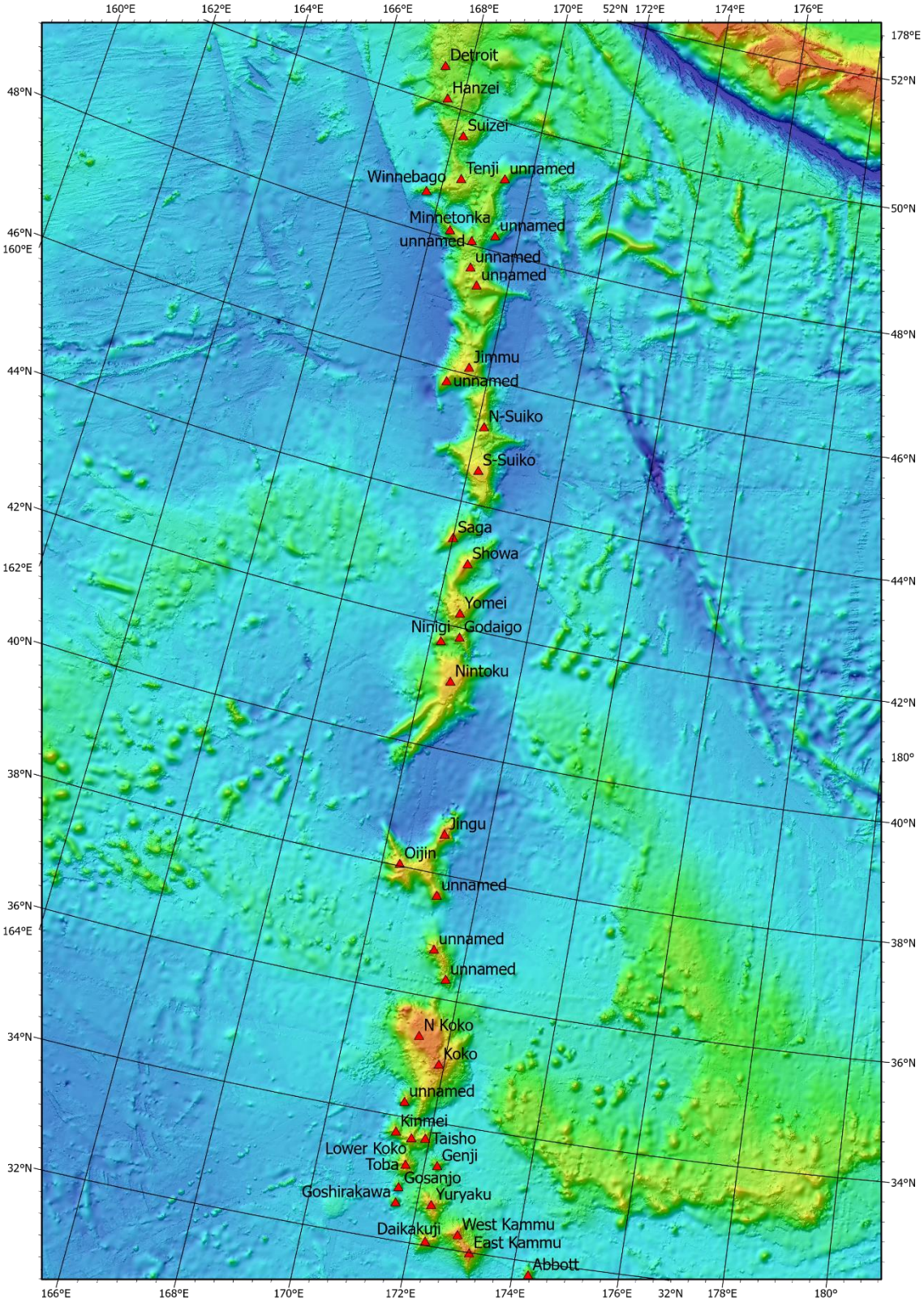

Figure 2.1: Maps Showing the locations of volcanic centres used in this study for the Hawaiian Seamount chain (a) and the Emperor Seamount chain (b).

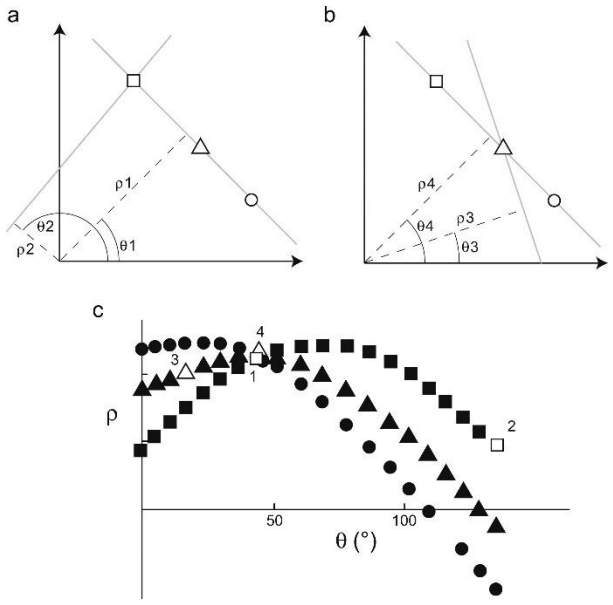

Figure 2.2: Graphical illustration demonstrating the application and workings of the Hough Transform from Pacey et al (2013) in order to recognise alignment. The Hough transform passes lines with all possibly azimuths through each point in the dataset. Grey lines in both panels, a and b show two of these possible lines for the square and triangle respectively. For all these lines the normal that passes through the origin, represented by dashed lines, is identified. The length of this normal (ρ) and angle to the x-axis (θ) are plotted against each other, resulting in a sinusoidal-shaped trace for each point (panel c). In this panel white points represent the azimuths/grey lines in panels a and b, and black points represent other normal to lines with different azimuths. Points which return the same $\rho - \theta$ values are aligned (points 1 and 4). An increased frequency of points returning the same $\rho - \theta$ values can therefore be a means of identifying alignments in datasets.

Figure 2.2, which shows the fitting of the Hough Transform, can be summarised according to Duda and Hart (1972): one point within an image represents a single sinusoidal curve within the graphical plane; one point within the graphical plane resembles a singular straight line within the image; points which lie on the same straight line within an image are all curves which cut through a common point within the graphical plane; points which lie on the same curve in the graphical plane are representative of lines which cut through the same

points within the image. Furthermore, the Hough Transform operates within x-y space and not on a Mercator or other common map projections, hence, when using latitude and longitude points in the Hough Transform, a gnomonic projection (a map projection where the centre of projection is the centre of the Earth, allowing for great circles to be shown cartographically as straight lines (allowing for an x-y space to be used for the Hough Transform) is used to correct for this. The use of the Hough Transform on the Hawaii Seamounts' spatial database has produced a wide variety of suitable alignments (Figure 2.4); the quality of the fit for each of these alignments, distinguished by an individual RMS-misfit value (Table 3.1).

Lines identified by the Hough Transform describe alignments between two volcanoes at each end. These are not necessarily best fit lines for the set of volcanoes which are encompassed by those end points. In order to find the best fits for each alignment, linear transformations had to be iteratively applied to the length, centre point and orientation for each alignment in order to minimise the rms-misfit for each segment, as was done in Andikagumi et al. (2020). Figure 2.3 shows how these transformations were altered.

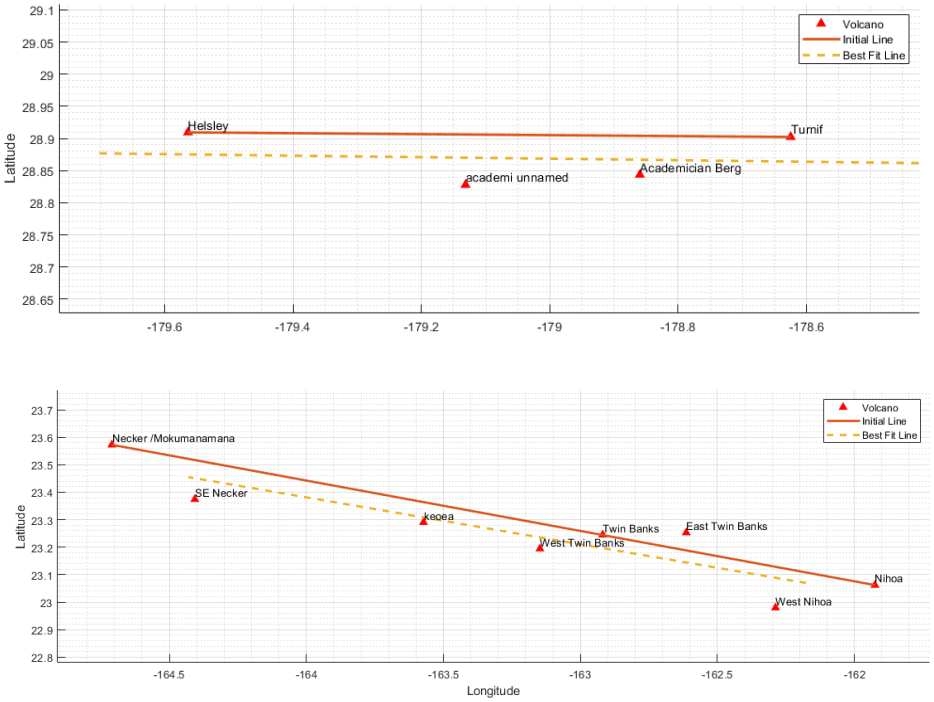

Figure 2.3: Graphs showing the effect of the linear transformations applied to segments along the Hawaiian chain. The best fitting lines are decided by those produced with the smallest RMS values, which are able to be seen in Table 3.1

2.2.2 Refining Identified Segments:

As multiple alignments identified have been across the Hawaii-Emperor seamount chain the quality of these alignments had to be assessed and the best fitting combination of segments determined. A combination of methods was therefore used in order to select the best segments for the Hawaii-Emperor seamount chain these are as follows. Firstly, an assumption has been made that (if the individual volcanoes of interest are independent of one another) separate processes which might influence the creation of two different segments would not both impact the creation of a single volcano which has the potential to lie on both of these segments. As a result of this assumption, this would mean that each volcano created along an ocean island chain is only able to be associated with one segment. Furthermore, a set of criteria were developed in order to help determine with the determination of which great circles were to be included and to distinguish which volcanic centres were not related to each other. They include:

- Spacing between separate volcanoes being <170km.
- The perpendicular distance of a volcanic centre from an alignment must be <35km.

This meant that a segment could not include two volcanoes whose spacings were >170km between each other and if a volcano had a perpendicular distance >35km from an alignment it was assumed to not be a part of the segment. Where there was uncertainty surrounding which volcanoes belonged to a segment, geochemical and radiometric data were used in order to distinguish whether these volcanoes had entirely anomalous dated ages or had ages correlating to separate segments, as the Hawaii Chain has very clear age progressions and in parts very distinct geochemical trends Regelous et al., (2003); Ballmer et al., (2011); Gaastra et al., (2022). Volcanoes which have been deemed off segment/chain have been done so based on their distance from segments, their morphologies (i.e. volcanoes being extensions of rift zones) as well as their radiometric ages. Further discussion on excluded volcanic centres is found in their relevant sections within Chapter 3 and 4. Finally, the best fitting segments were able to be determined by trying to find the minimum number of segments which fit these criteria that were required to make up the ocean island chain.

The code for the application of the Hough Transform and constraining of great circles, developed by Andikagumi et al (2020) has been modified. The now modified code outputs a graph showing the misfits of the segment for each initial alignment which had linear transformations applied to it. This code can be found in Appendix B, as well as tables showing properties of the final segmented great circles identified can be found in Section 3.1.2 and 3.2.2.

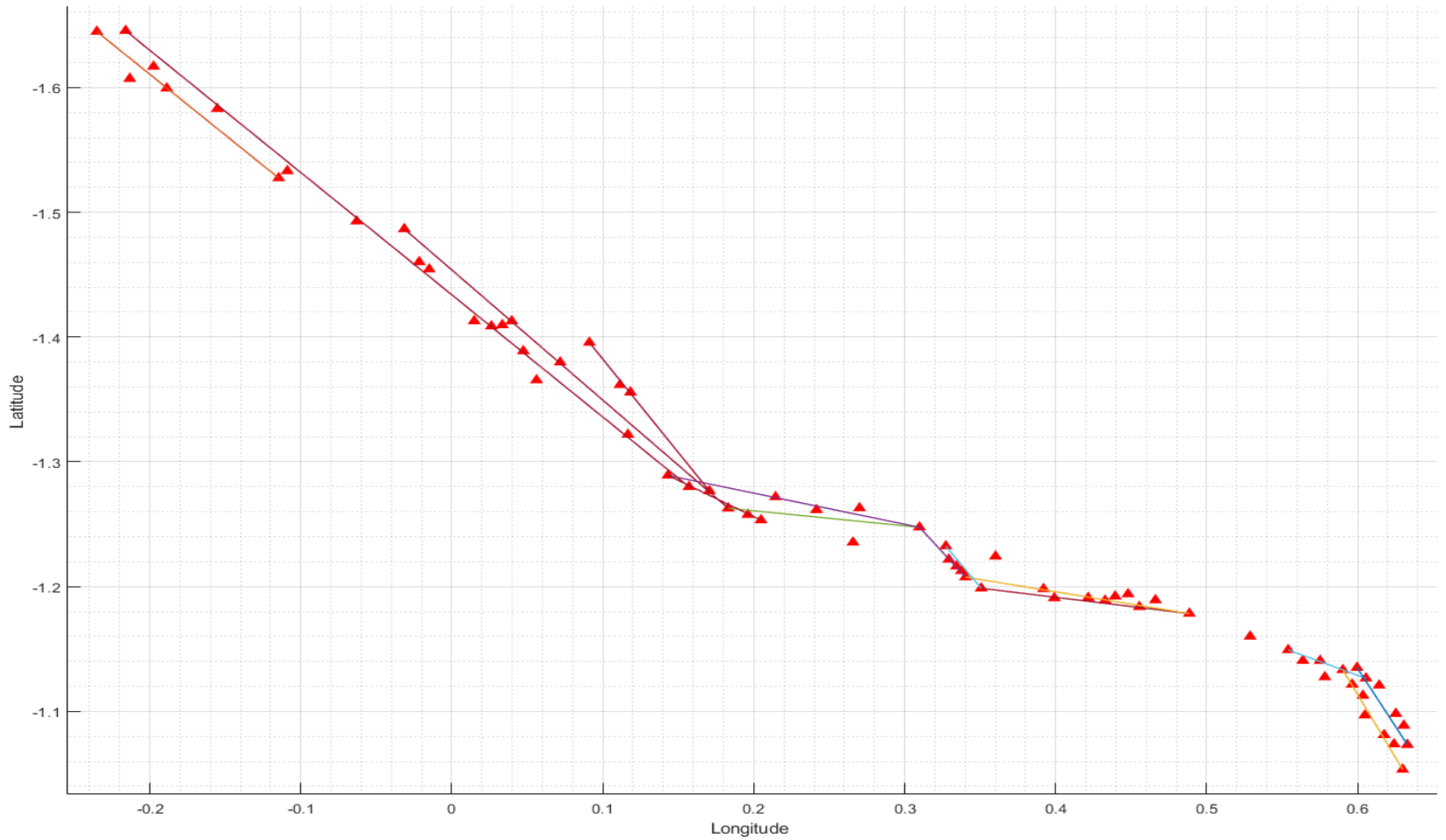

Figure 2.4: A graph showing the distributions of volcano alignments, as calculated by the Hough Transform where each red triangle represents a volcanic centre between Loihi Seamount and Daiakiuiji Seamount. Each straight line represents a great circle distribution for a group of volcanoes of which a minimum of four was allowed.

2.2.3 Small Circle Identification:

The geometry of ocean island chains being described by small circles has been adopted by multiple authors. Small circle geometries of ocean islands has been used to explain the distribution of volcanoes and plate motions as well as being used to draw comparisons between separate Ocean Island chains Lonsdale, (1988); Gaastra et al., (2022). Further to this, Fiske and Jackson (1972), Jackson et al. (1972, 1975) and Jackson and Shaw (1975) promote the use of a model similar to what could be interpreted as segmented small circles, where each small circle represents the loci of magmatic activity. In this project, best fitting small circle distributions were found for each of the previously identified individual segments. This was done by iterating through different values for the small circles centre coordinates and radius aiming to minimise an RMS-misfit of the volcanoes (the code for this can be found in Appendix A).

2.2.4 Comparison of Small Circles to Great Circles.

Initially, the use of residual plots, which can be seen in Chapter 3, can show how well-fitting different segments are to either great circle or small circle distributions. The shape/distribution of volcanoes along a great circle or small circle can help to give an initial idea as to which of these distributions is best fitting for the volcanoes in each individual segment. However, in order to draw more accurate comparisons between great circles and small circles the Akaike Information Criterion was used, expressed below (Andikagumi et al 2020).

$$AIC = n\log(\hat{\sigma}^2) + 2k$$

Eq. 1

Where, n is the number of volcanoes, k is the number of adjustable parameters (in this case for either a Great Circle or Small Circle). For example, a Great Circle has 2 adjustable parameters, the longitude and latitude of its centre point, and a Small Circle has three adjustable parameters, its centre point location as well as its radius. $\hat{\sigma}^2$ represents the

statistical estimator (in the case of these great circles, RMS-misfit) Burnham and Anderson, (2004); Andikagumi et al., (2020). $\hat{\sigma}^2$ is described below.

$$\hat{\sigma}^2 = \frac{\sum {d_n}^2}{n}$$

Eq. 2

Where, d_n refers to the individual misfits for each volcano perpendicular to a segment. Due to the number of volcanoes within the datasets being relatively small in comparison to adjusted parameters, a correction is needed in order to ward off any bias between the two different spatial distribution models (great circle vs small circle) which both have a different value for k Andikagumi et al, (2020). Doing this gives us the Akaike Information Criterion correction (AICc), as seen below,

$$AICc = AIC + \frac{2k(k+1)}{n-k-1}$$

Eq. 3

Combining Eqs 1, 2 and 3 the AICc can therefore be expressed as, Eq. 4:

$$AICc = n\log\left(\frac{\sum {d_n}^2}{n}\right) + 2k + \frac{2k(k+1)}{n-k-1}$$

Eq. 4

Both the Akaike Information Criterion and its correction are measures of the amount of data which is lost, when fitting a data set to a specific model Akaike, (1974); Burnham and Anderson, (2004); Andikagumi et al., (2020). A best-fitting model would be one which has the least amount of data lost, meaning that the lower AICc values are better.

Chapter 3. Results and analysis:

3.1 The Hawaiian Seamount chain:

The Hawaiian Seamount Chain is the younger, more active end of the Hawaii-Emperor Seamount chain. It is ~3500km long, stretching from Loihi Seamount (Kama'ehuakanaloa) North West to the Hawaii-Emperor bend, where it ends with the Kammu Seamounts. In this section, the spatial distributions of the Hawaiian Seamount chain are discussed, comparing both Great and Small Circles.

As previously mentioned, some volcanic edifices within the data base have been removed from the spatial analysis following running the spatial analysis model using the criteria set out in section 2.2.2. These edifices are as follows: Penguin Bank; Ni'ihau; Ka'ula; Kanehunamoku; unnamed (Raita); Bank 9; Nero; and Ladd. The locations, ages and further information on these volcanoes and seamounts can be found within Appendix A. Both the furthest west volcanoes of the subaerial portion of the Hawaii Seamount chain have been disregarded based on their radiometric dating as well as their positioning. Both of these volcanoes (Ka'ula and Ni'ihau), have younger radiometric ages than the volcano 'after' them in the Hawaii seamount chain (Ka'ena). As well as this, as can be seen in Figure 3.1, the general trend of these volcanoes from Ka'ena, is different in comparison to the rest of the Hawaii Seamount Chain. As a result of this evidence used in tandem with observations of their morphologies, both Ni'ihau and Ka'ula volcanoes have been attributed to be parts of the Ka'ena volcanoes' South West rift zone, which have broken above sea level.

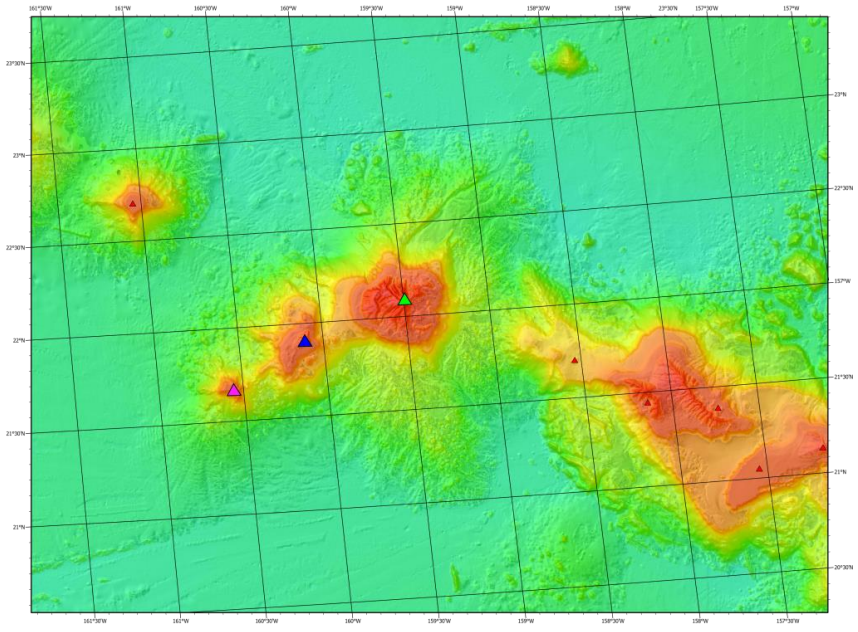

Figure 3.1: Image showing the spatial relationship between Ka'uai (green), Ni'ihau (blue) and Ka'ula (pink) volcanoes.

Based upon similar reasoning, Penguin Bank Seamount was also disregarded. This seamount appears, morphologically, to be an extension or acting as part of a 'rift zone' or submarine ridge (Figure 3.2). Using age data, these volcanoes also demonstrate an unexpected age trend. The two Molokai volcanoes have ages of 1.51 Ma and 1.89 Ma, for East and West respectively, whereas further west, Penguin Bank has a radiometric age of 1.5 Ma instead of an older age as expected. Additionally, the formation of the two Molokai volcanoes have been postulated to have been influenced by multiple weaknesses in the lithosphere in the form of the Molokai Fracture Zone Anchieta et al., (2011) and references within. As Penguin Bank extends from the Molokai volcanoes at a very similar azimuth to the Molokai Fracture zone, it is plausible that this weakness within the lithosphere has allowed magma to be channelled forming a submarine ridge.

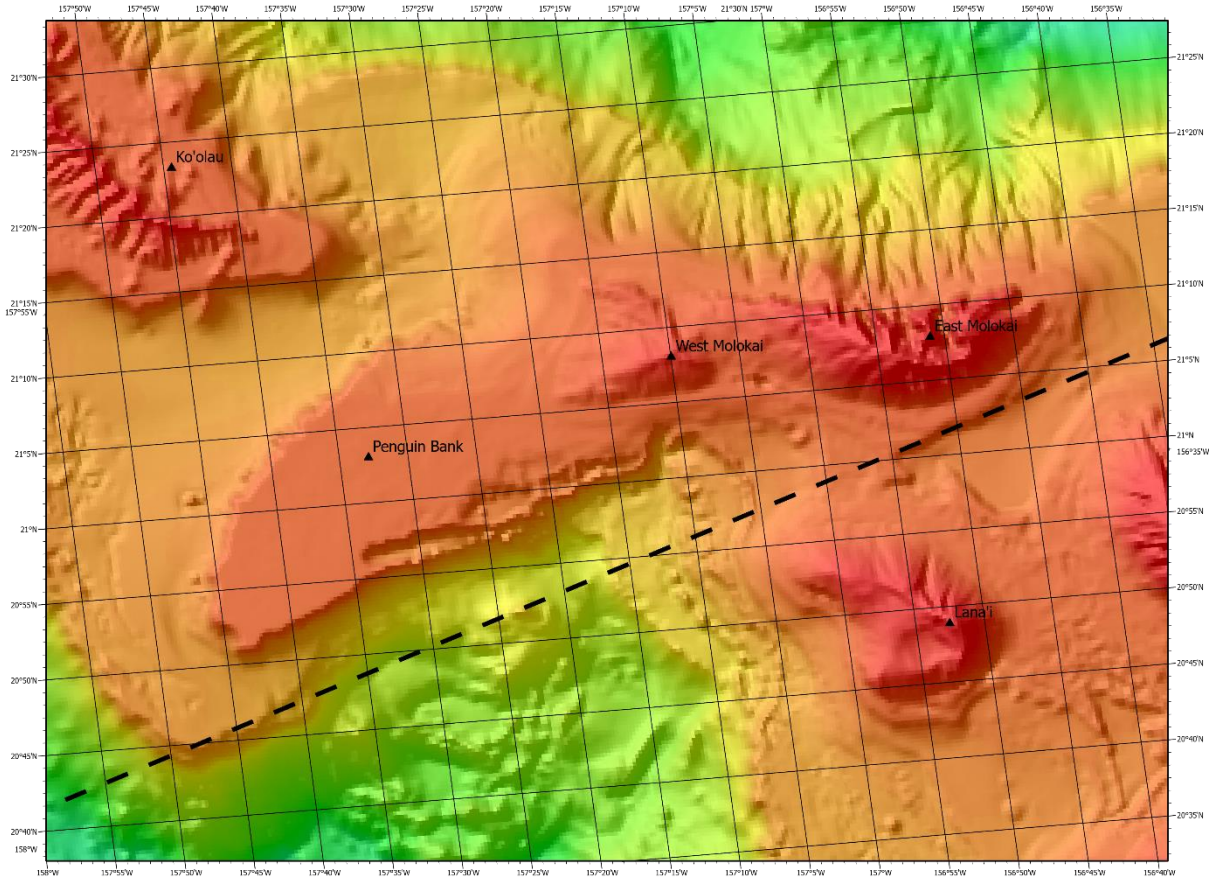

Figure 3.2: Image showing the spatial relationship between Penguin Bank and the East and West Molokai volcanoes. Black triangles represent volcanic edifices, and the dashed line represents the inferred position of the Molokai Fracture Zone.

Both the Ladd and Nero Seamounts have very peculiar positionings within the Hawaii Seamount Chain. They are found both North East and South West of Midway Atoll, forming a very clear trend (SW,NE) in contrast to the general trend of the Hawaii Seamount Chain (trending NW-SE). As a result of this shape, these volcanoes have been classified as ‘cross track’ seamounts, as previously mentioned. These seamounts are positioned far from their expected positions when considering the rest of the Hawaiian Ridge as an example, giving the midway portion of the Seamount chain a more ‘clustered’ appearance opposed to the significantly more linear nature that it has along the rest of its track. It is uncertain what is the exact cause of the organisation of these seamounts. However, it has been hypothesized that they have formed from exploited weaknesses in the oceanic lithosphere, in the form of older,

Cretaceous seamounts from the Wentworth seamount chain, forming composite seamounts, or from smaller transform zones within the lithosphere, with a similar azimuth to the Mendocino and Murray fracture zones which cross-cut the Hawaii Seamount chain. As a result of this, these two seamounts have been left out of the spatial analysis.

Somewhat similar to the Ladd and Nero Seamounts, Bank 9 has been left out of the spatial analysis due evidence suggesting it is a composite seamount, forming 'in tandem?' with an older cretaceous seamount which is present on its Southern Flank Kelley et al., (2015) which will have influenced the distribution of volcanism at this part of the Hawaii Seamount Chain. Figure 3.3 is a map illustrating Bank 9.

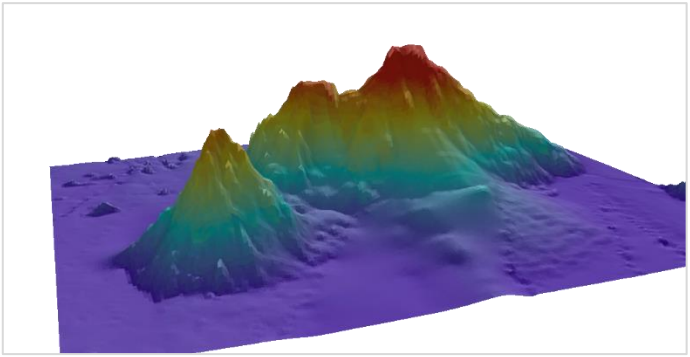

Figure 3.3: Images depicting the morphology and spatial distribution of Bank 9 Seamount. This figure shows a 3D model showing the relationship between Bank 9 (furthest right peak) and the older cretaceous seamount that is hypothesized to have influenced its formation (central peak).

3.1.1 Spatial Distributions of seamounts and trends along the Hawaiian Seamount Chain:

A common misconception with the Hawaii Seamount Chain is that it is comprised of regularly spaced, edifices Brink, (1991); Hieronymus and Bercovici, (2001). What has become more apparent following analysis of the distribution and spacing of volcanoes along this chain is that the Hawaiian Seamounts are not regularly spaced this is able to be seen in Figure 2.1. Between the Hawaii-Emperor Bend and the Midway Seamounts there appears to be

significantly less regularly spaced volcanic centres (with spacings between volcanic centres ranging between 279km and 28km), this is significantly different in comparison to the volcanoes between the Midway Seamounts (~27Ma) and the main Hawaiian Islands (subaerial volcanic edifices) appear to be a lot more regularly spaced (<14% of the spaces between volcanoes are greater than 100km (6 out of 45) with the largest space in volcanism being 170km before the most recent change in direction of the Hawaiian chain).

Whitehead (1982) argues that the idea of regularly spaced volcanic edifices is without doubt over-simplified. They have produced a depth profile along the Hawaii-Emperor seamount chain (Figure 3.5) which in fact shows that there are multiple ridge-like clusters of which the Hawaii-Emperor seamount chain is comprised of. The lack of regularly spaced edifices along the Hawaiian chain then led towards discussion surrounding the potential variations of magma production rates. Vidal and Bonneville (2004) utilised a filtering method on 2 dimensional grids in order to calculate the volumes of volcanic edifices along the Hawaii-Emperor Seamount Chain (Figure 3.4) They showed that volumes of magma erupted along the Hawaii Seamount chain have vastly increased towards the youngest ends of chain (as much as up to 300% in comparison to older ages). When comparing these trends in volcanic volumes, it is possible that ‘spikes’ in apparent magma flux could occur in turn with changes in direction of the seamount chain for example, at ~12/13 Ma, one at the Hawaii Emperor Bend one at the bend in the chain currently being formed.

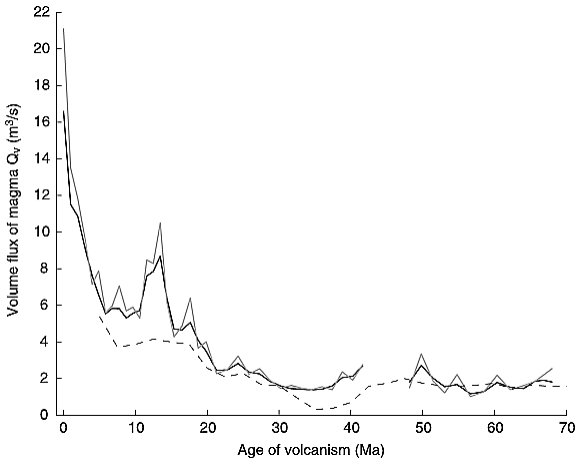

Figure 3.4: A graph demonstrating the significant changes in volumes of volcanic edifices throughout the history of the Hawaii-Emperor Seamount chain Vidal and Bonneville, (2004).

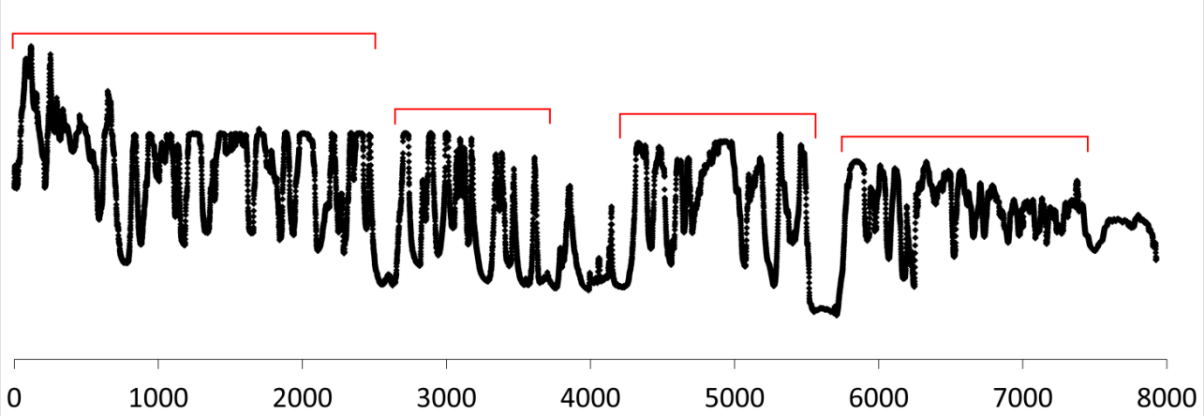

Figure 3.5: Schematic showing the depth profile along the Hawaii-Emperor Seamount chain (y-axis) following the track of minimum elevation. Where red bars represent seperate 'ridge-like clusters'each separated by areas of conderably lower bathymetry. Modified from Whitehead, (1982).

3.1.2 Great Circle Distributions:

The Hough Transform was able to identify 16 potential alignments for the Hawaiian chain, each of which had been rationalised and refined. This process led to incorporated into

other segments, leaving 6 alignments being disregarded. This led to 10 optimal great circles encompassing the Hawaii Seamount Chain (seen in Table 3.1 and represented visually in Figure 3.6). The combined rms-misfit for all 10 of these segments is 11.52km The identified segments which make up the Hawaii Seamount chain are as follows, starting from the youngest end of the chain to the oldest: HAWAII-01 (rms = 6.9km); HAWAII-02 (rms = 5.7km); HAWAII-03 (rms = 3.8km); HAWAII-04 (rms = 7.6km); HAWAII-05 (rms = 4.8km); HAWAII-06 (rms = 7.3km); HAWAII-07 (rms = 4.9km); HAWAII-08 (rms = 27.1km); HAWAII-09 (rms = 4.2km); HAWAII-10 (rms = 14.3km).

	Initial rms-misfit (km)	Optimised rms-misfit (km)	Length (km)	Point A Lon (°W)	Point A Lat (°N)	Point B Lon (°W)	Point B Lat (°N)	Azimuth (clockwise from N)
HAWAII-01	19.1	6.9	288.7	155.5855	19.8734	157.0054	21.3779	312°
HAWAII-02	17.4	5.7	364.6	155.2414	18.917	157.1659	21.1362	315°
HAWAII-03	11.8	3.8	403.2	157.8167	21.3828	161.0178	22.6983	290°
HAWAII-04	19.3	7.8	303.3	161.9385	23.0312	164.7314	23.5087	278°
HAWAII-05	9.9	4.8	147.4	166.7315	23.9953	167.2414	24.4971	310°
HAWAII-06	19.9	7.3	393.4	168.0305	25.014	171.7332	25.7791	283°
HAWAII-07	11.2	4.9	271.1	172.0807	25.3813	173.9609	26.0712	294°
HAWAII-08	10.4	2.9	275.6	175.6873	27.7747	178.3864	28.4739	286°
HAWAII-09	10.8	4.2	94.8	178.8068	28.8757	179.896	28.8505	273°
HAWAII-10	39.2	14.3	704.3	-178.8764	29.9216	-172.4808	32.3157	301°

Table 3.1: Great Circle properties and rms-misfits for identified segments along the Hawaii Seamount chain.

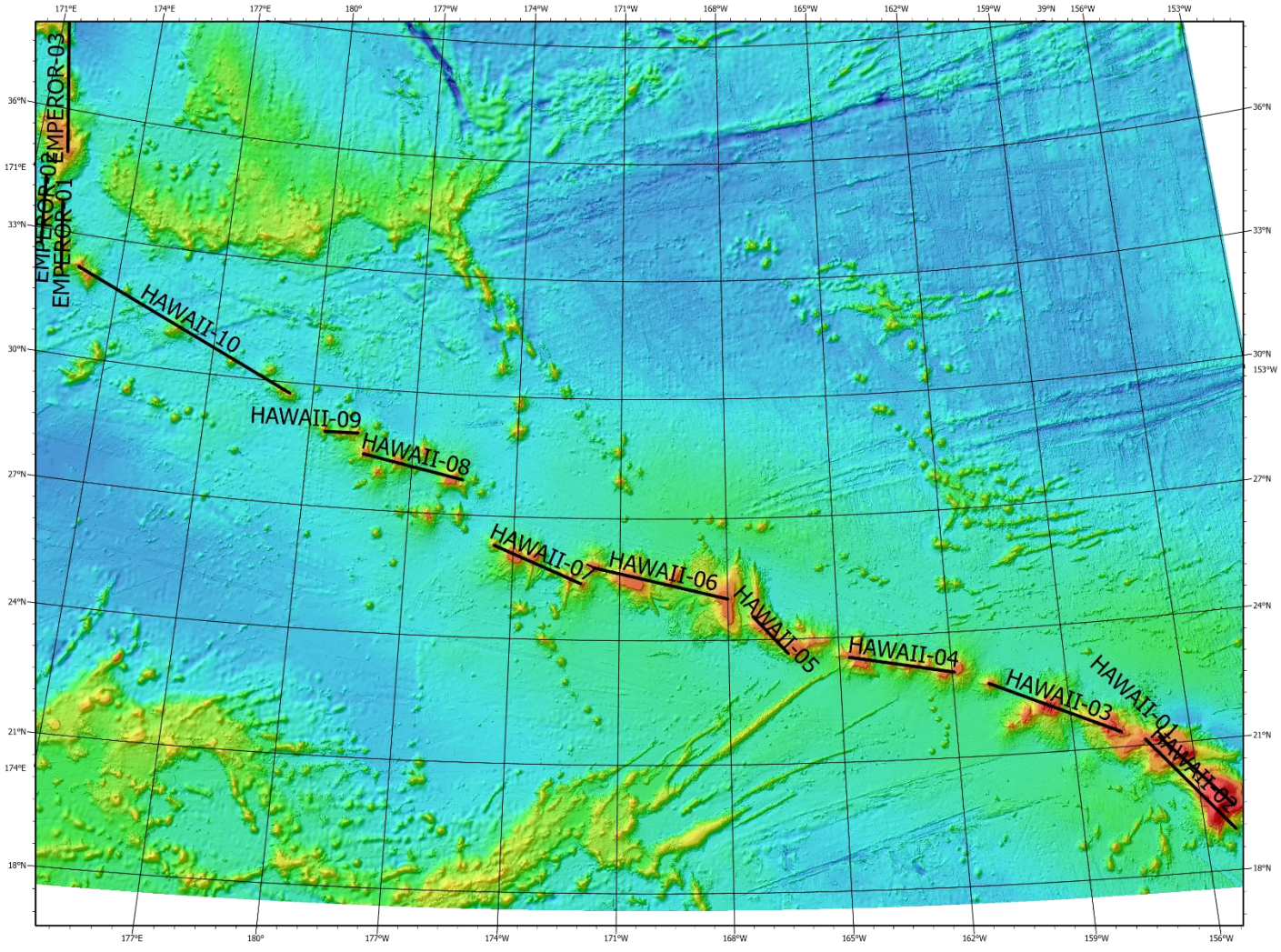

Figure 3.6: Map on a gnomonic projection demonstrating the segmentation of volcanoes within the Hawaii Seamount Chain. Red triangles denote identified volcanic edifices, and black lines represent identified Great Circle Segments using the Hough Transform analysis.

3.1.3 Small Circle Distributions:

The distribution of volcanic centres along the Hawaii Seamount Chain has previously been analysed as representing a singular small circle Gaastra et al., (2022), and segmented small circles or en-echelon 'loci' Fiske and Jackson, (1972); Jackson and Shaw, (1975); Jackson et al., (1975). In this study, the Hawaii Chain has been tested as both a whole, singular Small Circle and as segmented Small Circles, the segments being comprising of the same volcanoes as the great circles were. The singular Small Circle gave an rms-misfit of 368.9km. In comparison, the segmented small circle model had rms-misfits between 0.06km and 21.2km, for each segment and a combined misfit of 53.4km. All of the rms-misfits and properties of these segmented and singular small circles are as follows: HAWAII-01 (rms = 14.8km); HAWAII-02 (rms = 9.1km); HAWAII-03 (rms = 9.0km); HAWAII-04 (rms = 9.5km); HAWAII-05 (rms = 2.5km); HAWAII-06 (rms = 10.4km); HAWAII-07 (rms = 7.3km); HAWAII-08 (rms = 21.2km); HAWAII-09 (rms = 0.1km); HAWAII-10 (rms = 17.7km).

	Misfit (km)	Radius (km)	Centre Latitude (^{o}N)	Centre Longitude (^{o}W)
HAWAII-01	14.8	3627.4	1.33711	-183.214
HAWAII-02	9.1	684.6	23.8637	151.0751
HAWAII-03	8.9	792.3	28.4322	156.1938
HAWAII-04	9.5	597.6	28.4981	162.2990
HAWAII-05	2.5	227.2	25.6166	165.3525
HAWAII-06	10.4	826.4	18.2410	171.4988
HAWAII-07	7.3	563.8	21.1985	175.3311
HAWAII-08	21.2	185.1	26.7556	177.1555
HAWAII-09	0.1	121.2	29.9163	179.0855
HAWAII-10	17.7	1344.9	41.7250	182.5366

Table 3.2: Small Circle properties and rms-misfits for identified segments along the Hawaii Seamount chain.

3.1.4 Great and Small Circle distribution comparison:

Figure 3.8 shows the shape of the first segment within the Hawaii seamount chain in comparison to both great circle and small circle distributions in order to determine the true shape of volcano segments Andikagumi et al (2020). Figure 3.7 demonstrates how residuals along either a great or small circle distribution help to distinguish the true shape of a volcanic segment. A group of volcanoes which produce a great circle distribution, the observed ΔGC residuals should produce a line close to $y = 0$. Likewise, for a group of volcanoes which actually produce a small circle distribution on a sphere, the observed ΔSC residuals should produce a line close to $y = 0$.

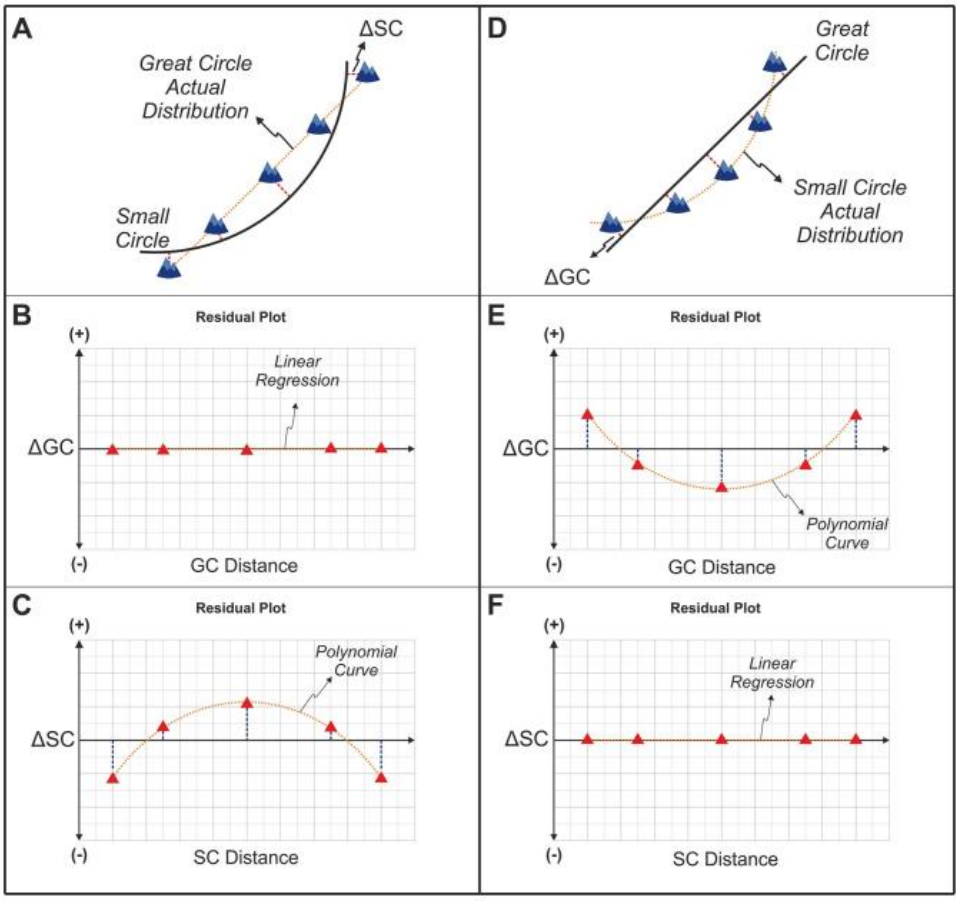

Figure 3.7: a schematic from Andikagumi (2020) demonstrating the use of residuals for the determination of the shape of volcanic segments. Panels A and D show separate distributions of volcanic segments, on a great circle and small circle distribution respectively.

Panels B and C, compare the residuals of volcanoes in Panel A along both great circle and small circle distributions respectively, expected residuals if a distribution of volcanoes were ideally fitting to a great circle. Similarly, Panel E and F compare the residuals of volcanoes in Panel D along both great circle and small circle distributions respectively, showing the expected residual if a distribution of volcanoes were ideally fitting to a small circle.

Using panels A, B and C from Figure 3.7 we can therefore understand that, if the distribution of a segment is actually a great circle, the residuals from a great circle (ΔGC) should align along a straight line. As well as this, the residuals for this segment about a small circle distribution (ΔSC) will be positioned along an arc if it is actually a great circle. However, this is the opposite if the segments distribution actually follows a small circle, with ΔSC following a straight line and ΔGC following a curved trend.

The graphical comparison between great and small circle fitting in the first segment of the Hawaii seamount chain (HAWAII-01) is shown within Figure 3.8. A distribution of volcanoes about the which doesn't best follow a linear distribution about the origin can be seen within Panel A, compared to a more regular distribution surrounding an arc distribution in Panel B. Using this information, the segment HAWAII_01 can be classified as having a great circle distribution. Due to the uncertainty surrounding the ΔGC residuals for this segment, it highlights the need for further statistical analysis to shed greater light on determining between great and small circle distributions.

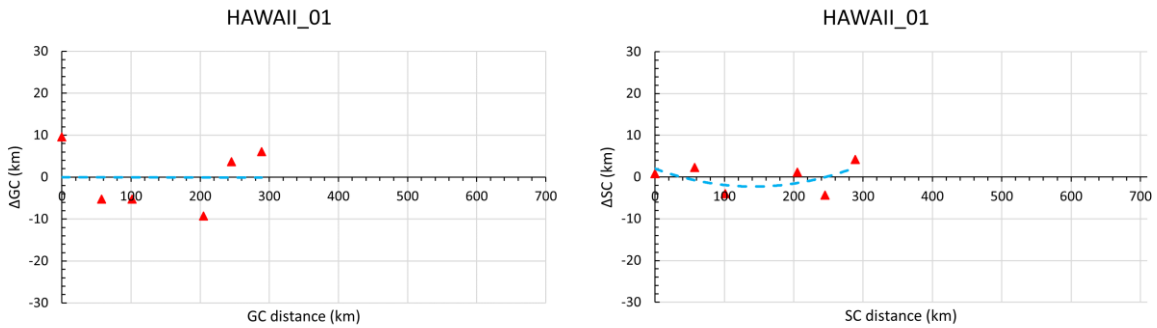

Figure 3.8: Residual plot showing the great circle and small circle distributions of volcanoes within the segment HAWAII-01. Red triangles represent individual volcanic centres. The blue dashed line represents either the respective great circle or small circle the volcanoes are distributed along.

Similar to the first segment of the Hawaii seamount chain, Figure 3.9 shows the shape of the second segment (HAWAII-02) within the Hawaii seamount chain as both a great circle distribution. A strong random distribution of volcanoes along a line can be seen within Panel A, compared to a more regular distribution surrounding an arc in Panel B, similar to that seen in HAWAII-01. Both of these distributions suggest that the second segment within the Hawaiian Seamount Chain also is more likely to follow a great circle distribution.

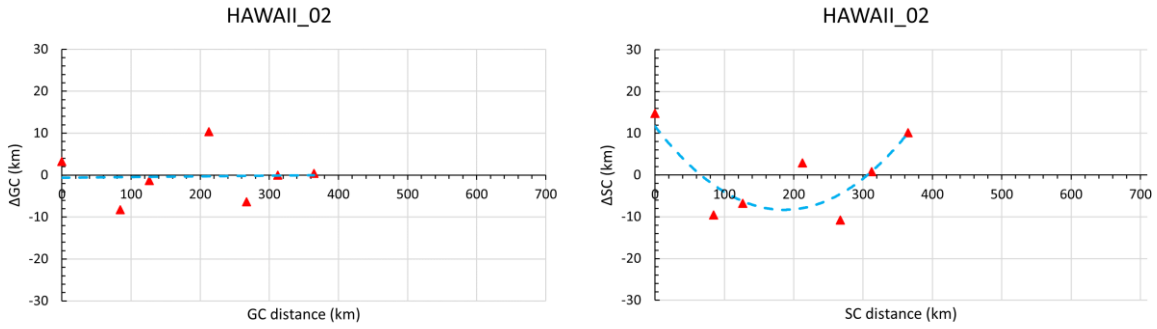

Figure 3.9: Residual plot showing the great circle and small circle distributions of volcanoes within the segment HAWAII-02.

Both HAWAII-03 and HAWAII-04 demonstrate more convincing great circle trends in comparison to small circle trends. In Panel A of both Figure 3.10 and Figure 3.11, a scattered,

random distribution is shown. HAWAII-03 has a significantly better fitting linear distribution for ΔGC in comparison to HAWAII-04 with only one of the volcanoes located along the segment deviating further than 6km from the best fitting great circle. HAWAII-04 has ΔGC fitting a great circle distribution worse than the previous three segments with >3 volcanoes deviating from the best fitting great circle >6km however it still can be seen in Panel B of figure 3.11 that an arcuate distribution for volcanic edifices is shown for ΔSC, hence favouring a great circle distribution describing the distribution of this group of volcanoes in HAWAII-04. Likewise, a very strong ΔSC trend fitting an arc can be seen in panel B of Figure 3.10 suggesting that the volcanoes on the segment HAWAII-03 follows a strong great circle distribution.

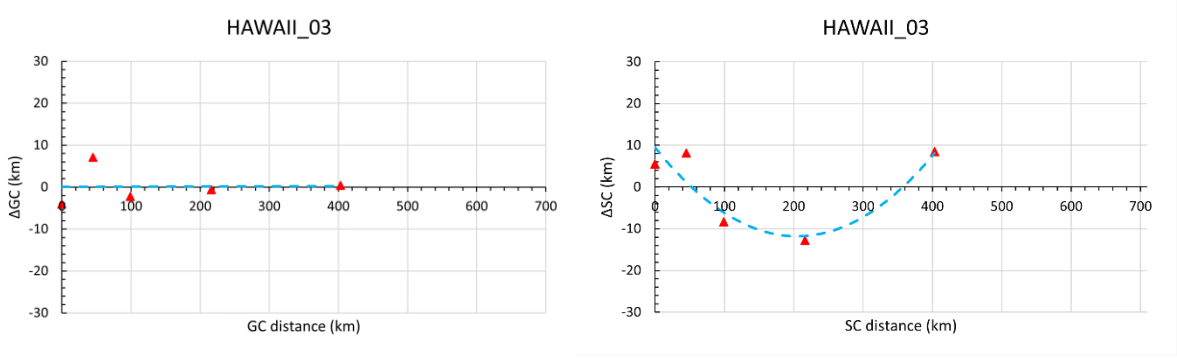

Figure 3.10: Residual plot showing the great circle and small circle distributions of volcanoes within the segment HAWAII-03.

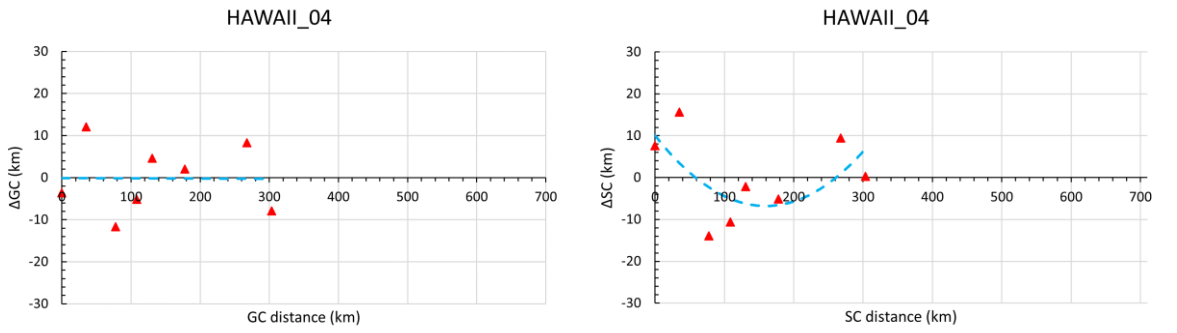

Figure 3.11: Residual plot showing the great circle and small circle distributions of volcanoes within the segment HAWAII-04.

The residuals of HAWAII-05, as seen in Figure 3.12 is somewhat anomalous in comparison to the four previous segments. It can very clearly be seen that a linear distribution does not best describe the distribution of volcanoes within this segment for ΔGC. This is because in Panel A, the distribution of volcanoes along the great circle segment have a very arcuate formation and, in Panel B of Figure 3.12 the volcanoes follow the small circle line well. Large misfits within both of these models further reinforce the need for statistical analysis to help determine between either a great or small circle fit for this segment.

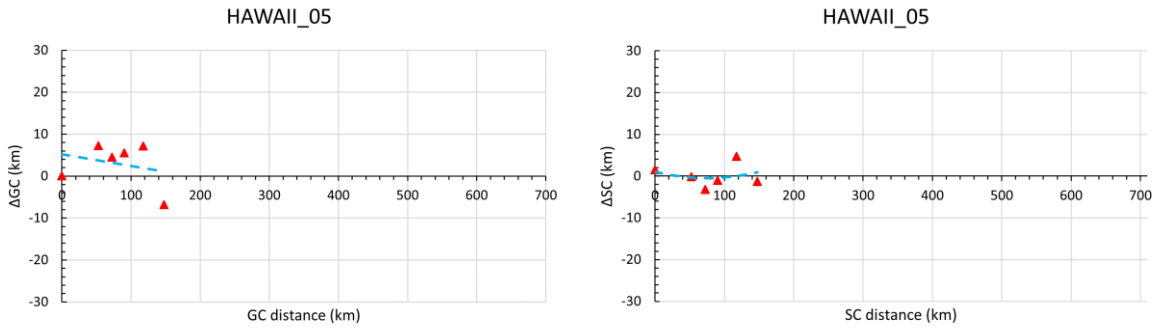

Figure 3.12: Residual plots showing the great circle (Panel A) and small circle (Panel B) distributions of volcanoes within the segment HAWAII-05.

HAWAII-06 in comparison to the other segments has fewer edifices sitting along its segment, having only 4. This can make decisions into whether a great or small circle is the best distribution more difficult. However, despite this when comparing both Panel A and Panel B within Figure 3.13, a random organisation of volcanoes along a line for ΔGC in tandem with an arcuate organisation of volcanoes for ΔSC highlight that this segment is best described by a great circle in comparison to a small circle.

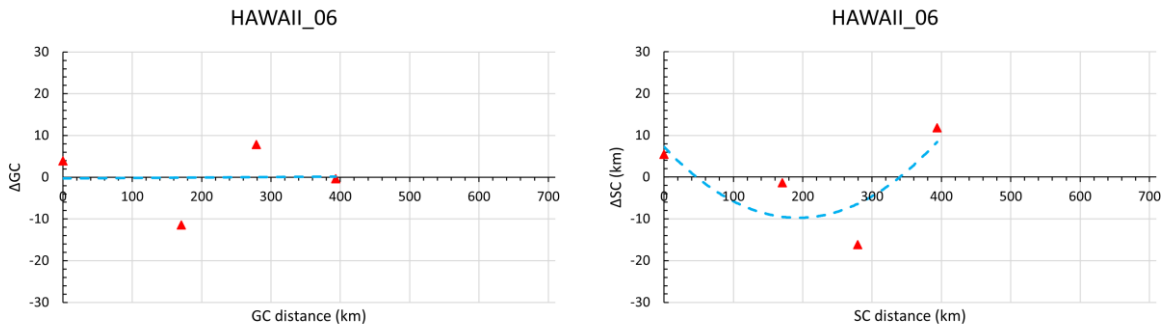

Figure 3.13: Residual plot showing the great circle and small circle distributions of volcanoes within the segment HAWAII-06.

HAWAII-07, similar to the first four segments of the Hawaii Seamount Chain, also shows a better resemblance to a strong great circle fit, this can be seen in Figure 3.14. The four volcanoes on either end of this segment all fit extremely well when looking at both Panel A and Panel B of figure 3.14 (< 2km), whereas the middle two volcanoes (Pioneer Tablemount and an unnamed seamount) are both much worse fitting, both being > 6 km from either the small circle or great circle. ΔGC clearly fits a random distribution about a line whilst ΔSC has an arcuate distribution. This shows that the segment HAWAII-07 is follows a great circle distribution.

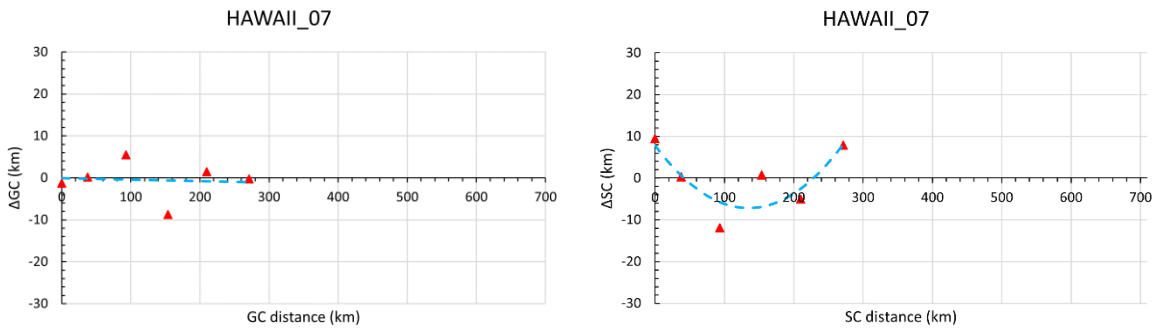

Figure 3.14: Residual plot showing the great circle and small circle distributions of volcanoes within the segment HAWAII-07.

In the segment Hawaii-08, there are only four volcanoes lying along it, due to the anomalous cross-track volcanoes (Ladd and Nero Seamounts) which are present at this point in the

Hawaii-Emperor seamount chain. It can be seen in Figure 3.15 that the volcanoes along both their ΔGC and ΔSC residual distributions best follow a straight line for ΔGC and an arc for ΔSC. However, the shape which these volcanoes make along each of these distributions can prove to be difficult to distinguish on the basis that there are not more data points. This yet again can highlight the need for further statistical analysis to distinguish whether great circle or small circle distributions best describe certain segments.

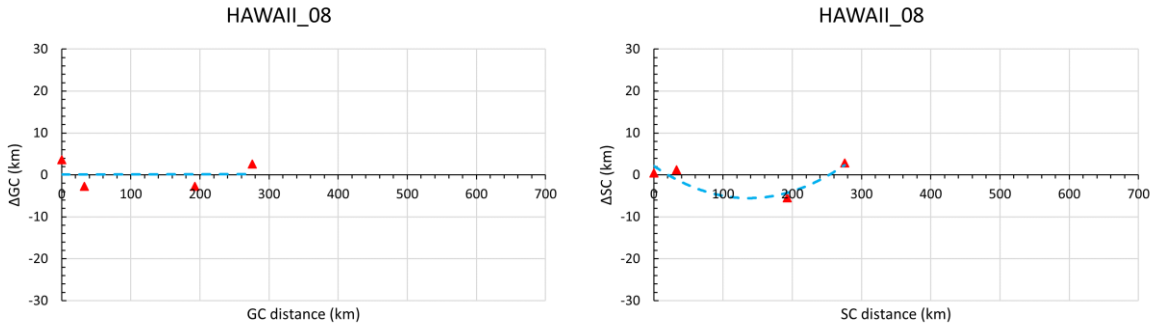

Figure 3.15: Residual plot showing the great circle and small circle distributions of volcanoes within the segment HAWAII-08.

According to figure 3.16 HAWAII-09, is better described by a segmented small circle distribution. The four volcanoes on this segment, make an arced shape in the ΔGC residual graph and very closely follow a straight-line distribution in the ΔSC residual graph this therefore means that these volcanoes are best described by a small circle distribution as shown and described in figure 3.7. The segment HAWAII-09 consists of only four volcanoes all of which are very closely spaced apart in comparison to volcanoes on other segments such as HAWAII-03 and HAWAII-02 potentially being a cause for this distribution.

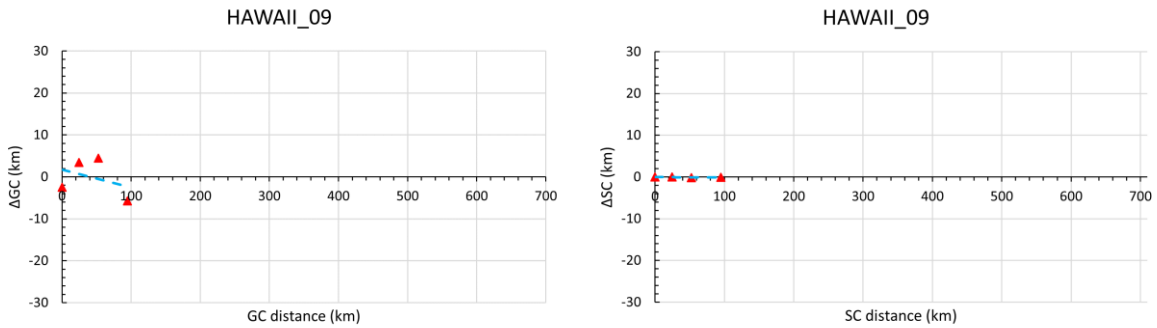

Figure 3.16: Residual plot showing the great circle and small circle distributions of volcanoes within the segment HAWAII-09. Red triangles represent individual volcanic centres. The blue dashed line represents either the respective great circle or small circle the volcanoes are distributed along.

HAWAII-10 is evidently the longest segment of the Hawaii seamount chain (~700km) (Figure 3.17). As well as this, HAWAII-10 is also the segment with the greatest deviation from both ΔGC and ΔSC residual distributions. Three volcanoes within this segment (Hancock, an unnamed seamount and Abbott) all have ΔGC misfits >10km, with the largest misfit being just under 30km for Hancock Seamount. A random organisation of volcanoes along a great circle distribution can be seen in Panel A, demonstrating that a great circle distribution can fit the volcanoes within this segment. As seen in Panel B of Figure 3.17, it is a bit more ambiguous whether a great circle distribution is a good fit for these volcanoes due to a few volcanoes such as Hancock which have large misfits. In this case, similarly with HAWAII-05 and HAWAII-09 further statistical analysis can prove to be beneficial in discriminating between whether a great circle or a small circle distribution is best suited to these volcanoes.

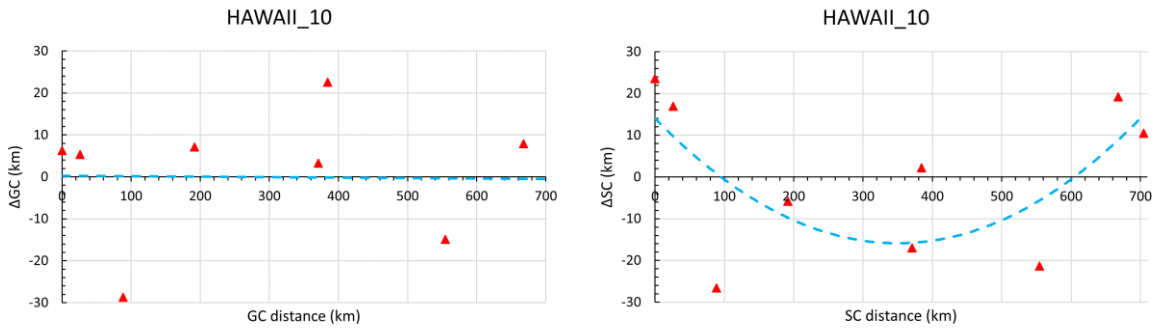

Figure 3.37: Residual plot showing the great circle and small circle distributions of volcanoes within the segment HAWAII-10.

Due to the ambiguity of the results from some of the residual plots for certain segments further statistical analysis was carried out using the Akaike information Criterion coefficient (AICc). For the comparison of both great circle and small circle segments of the Hawaii seamount chain, the AICc statistic was used in order to reduce bias between datasets which have a varying number of adjustable parameters. Table 3.3 shows a direct comparison between the AICc values obtained for the Hawaii Seamount Chain segments. It can be clearly seen that for all segments which allow comparison between great circles and small circles, a segmented great circle distribution is significantly better fitting in comparison to a small circle distribution. Across the Hawaii Seamount Chain, the average great circle AICc misfit is 19.9 and the average small circle misfit is 29.42.

	Segmented GC	Segmented SC
HAWAII-01	18.03	23.97
HAWAII-02	17.58	27.44
HAWAII-03	15.81	39.54
HAWAII-04	20.62	27.67
HAWAII-05	17.16	22.79
HAWAII-06[1]	22.87	-
HAWAII-07	15.59	28.36

HAWAII-08	25.20	33.92
HAWAII-09[1]	20.99	-
HAWAII-10	25.90	31.67

Table 3.3: Comparison of AICc values for the Hawaii seamount chain segments for both great and small circles. [1] Denotes a segment where the AICc is not available for small circles due to having a too small sample size of volcanoes.

It has been noted that the great circle segmentation of the Hawaii Seamount Chain fits significantly between the segments HAWAII-07 and HAWAII-01 (after 23 Ma) when compared to the full 10 segments. This change in the closeness of alignment can be very clearly seen within Table 3.3, however AICc values for these two have also been compared in their entireties as well. The AICc misfit for the entire 10 segments is 189.88, whereas the AICc misfit post 23 Ma is 109.76. This trend certainly points towards some form of geodynamic process leading to the alignments of segments being significantly closer fitting post 23 Ma in comparison to all of the segments from the Hawaii Seamount Chain.

3.1.5 Morphologies of Seamounts Along the Hawaii Seamount Chain:

Both the orientation of rift zones and principal axes of elongation were plotted for each separate segment along the Hawaii Seamount Chain in order to further understand if processes leading to segmentation of volcanoes could potentially impact individual edifices as well. Figure 3.18 shows orientations of rift zones and principal axes of elongation for the segment HAWAII-01. As can be seen in Panel A, the main largest rift zones along this segment all diverge away from the orientation of the segment, mostly E/ENE, whereas the shorter rift zones tend to follow the azimuth of the segment more closely but do tend to stray from this trend. Looking at Panel B of Figure 3.18 it can be seen very clearly that only one of the principal axes of elongation aligns with the azimuth of the segment, offset by ~10º.

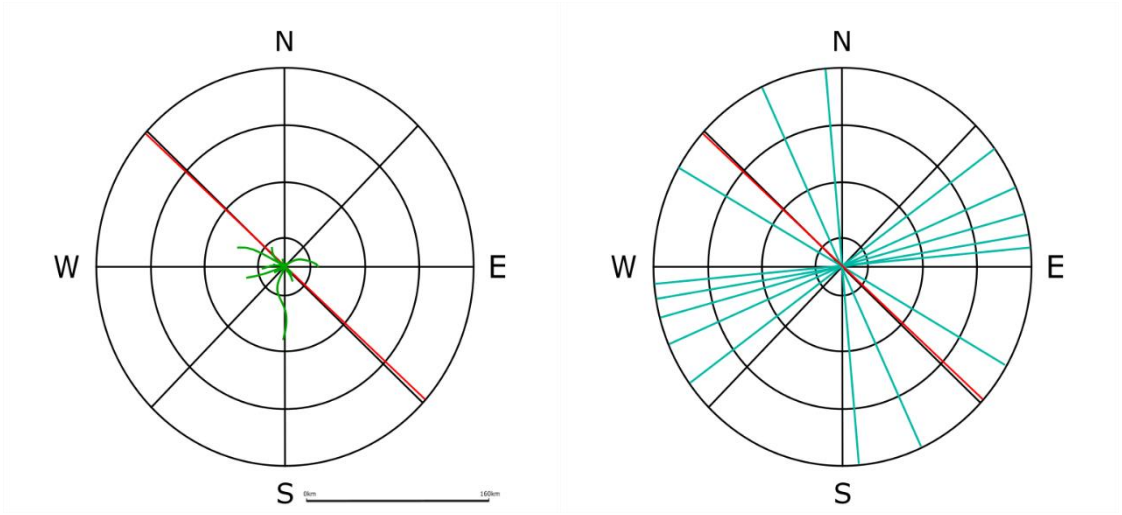

Figure 3.18: (a) Rose diagram showing the orientations of volcanic rift zones (green lines) compared to the overall azimuth of the segment (HAWAII-01) which the volcanoes lie on (red line). (b) Rose diagram showing the orientation of principal axes of elongation (blue lines) for separate volcanic edifices in comparison to the overall azimuth of the segment (HAWAII-01) which the volcanoes lie on.

HAWAII-02, similar to HAWAII-01 has both volcanic rift zones diverging and aligning with the orientation of its segment (Figure 3.19). Looking at Panel A of figure 3.19, it can be seen that four rift zones predominantly diverge from the segment orientation. In contrast the rest of the volcanic rift zones along this segment either mostly align with it or initially align with the segment and begin to diverge the further they reach from the volcanic centre. Elongations of volcanoes within this segment appear to form in clusters or preferred orientations. Examples of this being, clusters between 120º and 135º as well as between 65º and 80º. Some of these elongations are within 20º of the orientation of the segment.

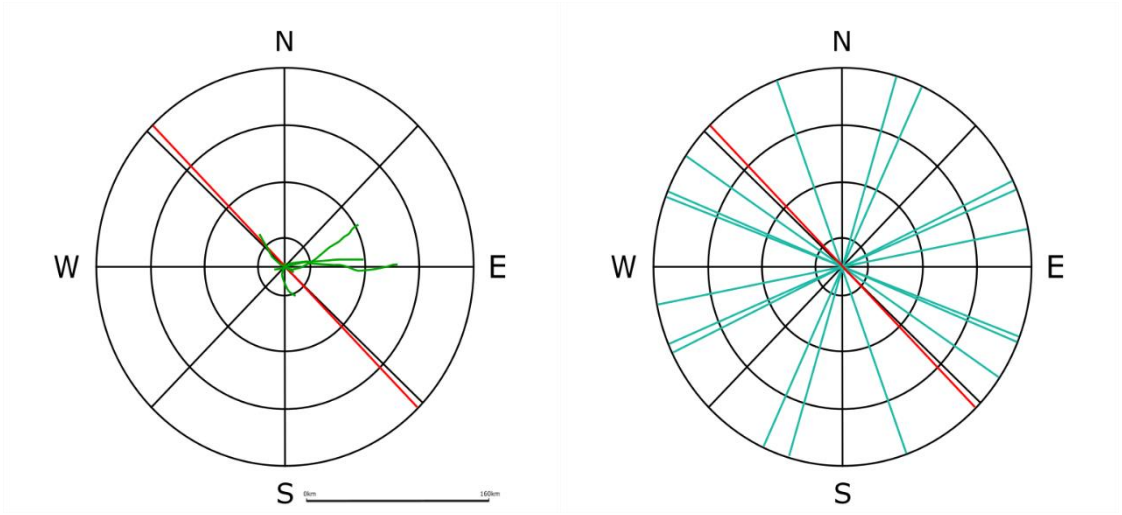

Figure 3.49: Rose diagram showing the orientations of volcanic rift zones (green lines) compared to the overall azimuth of the segment (HAWAII-02) which the volcanoes lie on (red line).

In the segment HAWAII-03, Panel a of figure 3.20 shows significantly shorter rift zones in comparison to those on both HAWAII-01 and HAWAII-02. It is apparent on this segment that there is a larger amount of rift zones aligning with the segment azimuth, either having started off propagating in a different direction and eventually aligning with the segment or continuing in that direction for its entirety. Very few volcanic rift zones do not align with the segments, and, similar to HAWAII-01, the majority of the longest rift zones do not follow the trend of the segment. As can be seen in Panel b of figure 3.20, all of the principal axes of elongation for the volcanoes within this segment lie within a 90º arc, however only one of these aligns well with the orientation of this segment.

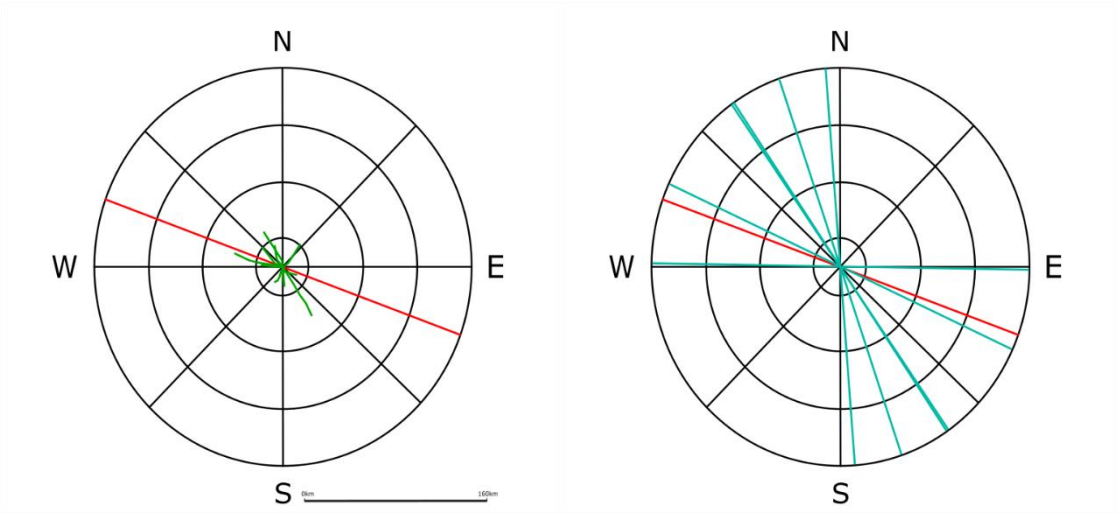

Figure 3.20: Rose diagram showing the orientations of volcanic rift zones (green lines) compared to the overall azimuth of the segment (HAWAII-03) which the volcanoes lie on (red line).

As can be seen within Panel a of figure 3.21 only three of the rift zones which lie along the segment HAWAII-04 align with the azimuth of the segment or follow a preferential direction. As with previous segments, the longest rift zones within this segment are those which are most orthogonal/misfit the most from the segment. Additionally, similar to previous segments, only one few principal axes of elongation within this segment align with its overall orientation.

The segment HAWAII-05 has only four volcanoes within it, hence why Panel a of Figure 3.22 has fewer rift zones than previous figures. Despite this, the rift zones along this segment are poorly fitting, and only two small rift zones align along the segment's orientation. Looking at Panel b of Figure 3.22, it can also be seen that very few elongations are in the same direction as this segment, but mostly appear within 50º and 100º of the actual orientation of this segment.

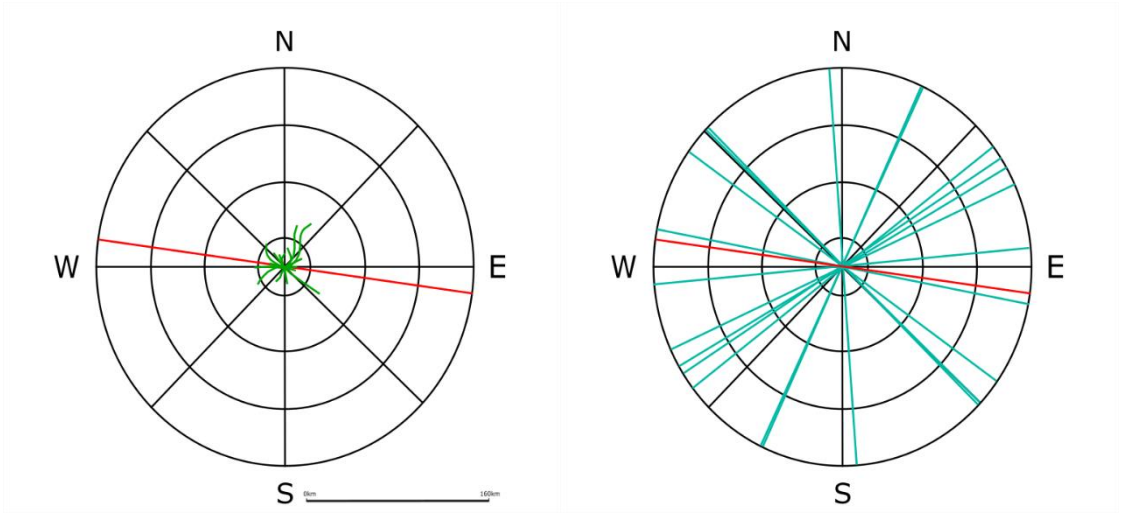

Figure 3.21: Rose diagram showing the orientations of volcanic rift zones (green lines) compared to the overall azimuth of the segment (HAWAII-04) which the volcanoes lie on (red line).

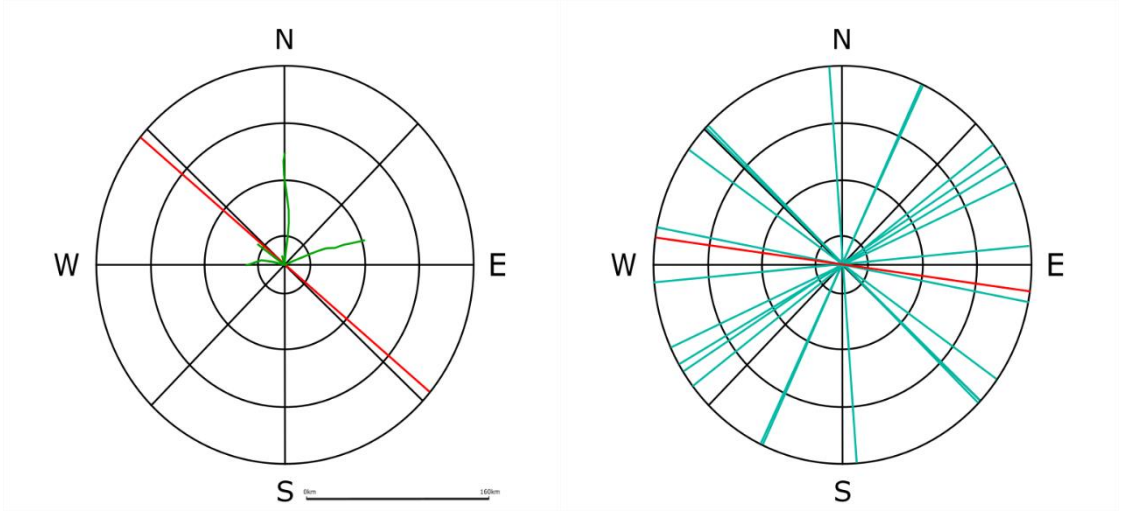

Figure 3.22: Rose diagram showing the orientations of volcanic rift zones (green lines) compared to the overall azimuth of the segment (HAWAII-05) which the volcanoes lie on (red line).

Panel A within figure 3.23 clearly demonstrates what has been mentioned about rift zones within previous segments. There are numerous volcanic rift zones within this segment where the initial propagation initiates in a direction not directly aligned with the segment,

however the rift zones grow more aligned with the segment the further they propagate. However, a continuous trend remains to be that the longest rift zones of each segment are the worst aligned with the segment direction. As with previous segments, volcanoes along the segment are mostly oblique to orthogonal to the segment orientation.

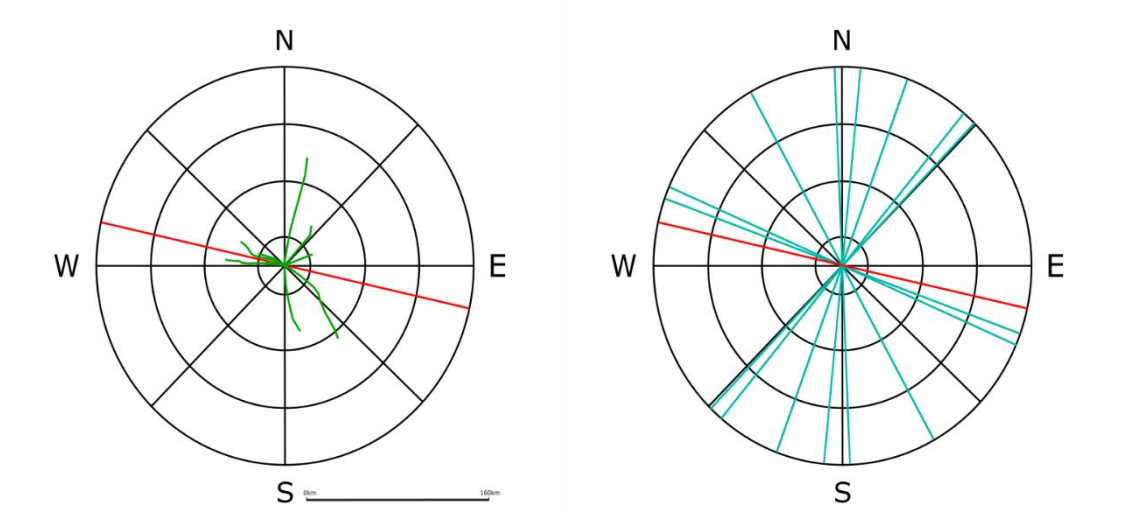

Figure 3.23: Rose diagram showing the orientations of volcanic rift zones (green lines) compared to the overall azimuth of the segment (HAWAII-06) which the volcanoes lie on (red line).

Figure 3.24 shows the rift zones and elongations of the segment HAWAII-07, a seamount from which was used as a great example of rift zones along the Hawaii-Emperor Seamount Chain in figure 2.1, within Section 2.1. As with HAWAII-06, the longest rift zones are poorly aligned with the segments' azimuth, with some shorter segments however also being poorly aligned as well. As well as this, multiple rift zones can be seen to have 'corrected' themselves as in previous segments where they do not align initially but after they have propagated for longer, they grow more aligned with the segment. As seen in Panel B of Figure 3.24 only two principal axes of elongation from all the volcanoes in this segment lie within 10º of the azimuth of the segment.

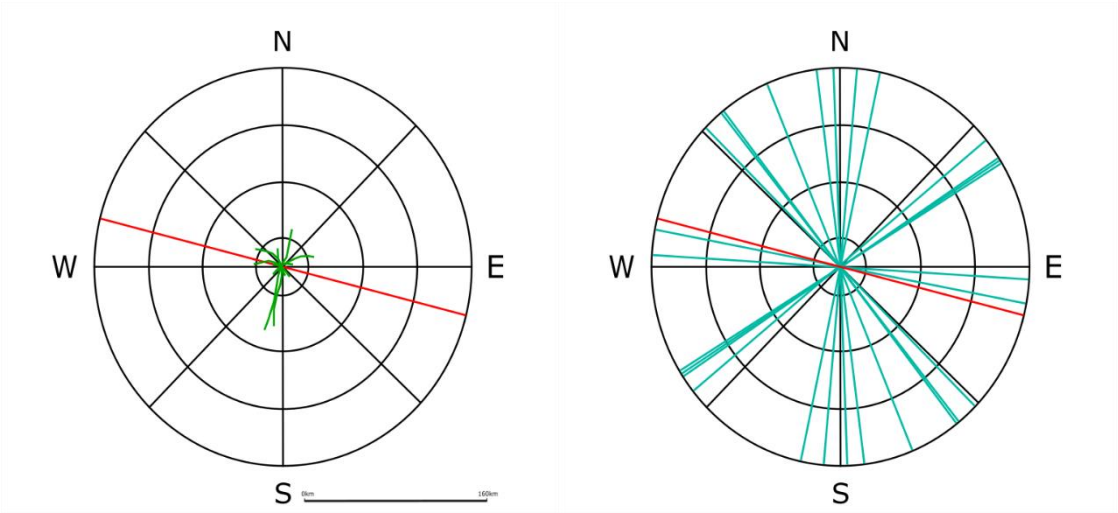

Figure 3.24: Rose diagram showing the orientations of volcanic rift zones (green lines) compared to the overall azimuth of the segment (HAWAII-07) which the volcanoes lie on (red line).

The segment HAWAII-09 has significantly shorter volcanoes and rift zones in comparison to other segments along the Hawaii Seamount Chain, as can be seen from Figure 3.25. It can be seen in Panel A that only two rift zones align with the segments' azimuth, in comparison to the rest which are at a significantly different angle. As with previous segments, there is no change in direction of these rift zones to favour alignment with the segments' azimuth, potentially as a result of rift zones not propagating far enough to correct themselves. Elongations of volcanoes, as seen in panel b of figure 3.25 follow the same trend as identified within the other segments. Only one axis of elongation, aligns well with the segments' orientation, while the other axes span a range of angles oblique to the segment.

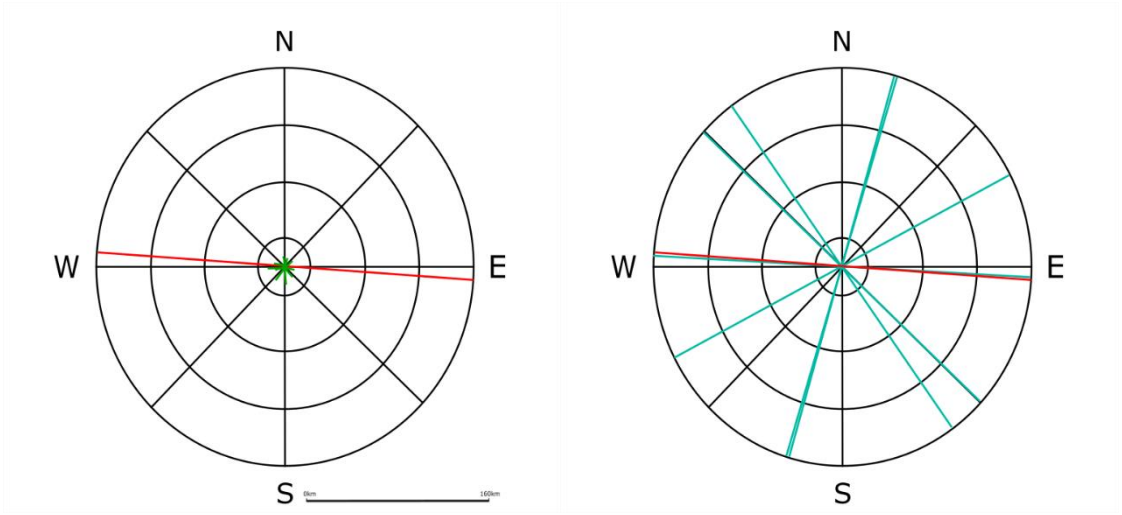

Figure 3.25: Rose diagram showing the orientations of volcanic rift zones (green lines) compared to the overall azimuth of the segment (HAWAII-09) which the volcanoes lie on (red line).

The tenth segment along the Hawaii Seamount Chain, HAWAII-10, appears very similar to HAWAII-09 in regard to rift zone orientation and axes of elongation orientations, this could potentially be as a result of these volcanoes being located at the older end of the Hawaii Seamount Chain (where the preservation of rift zones and volcanic edifices is significantly poorer), or due to these mostly being significantly smaller seamounts in comparison to the rest of the Hawaii Seamount Chain. As can be seen in Figure 3.26, only one of the rift zones associated with this segment is aligned with its azimuth whilst the rest extend in directions oblique to the segment. In contrast, HAWAII-10 has the most principal axes of elongation which aligning within 10º of the segments' azimuth whilst the other elongations, like in previous segments all lie oblique to the segment.

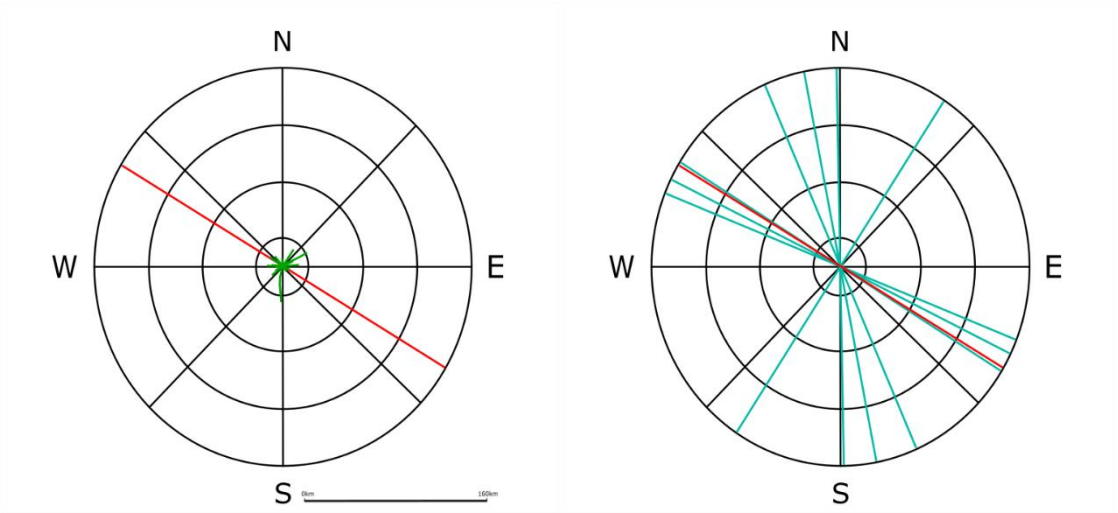

Figure 3.26: Rose diagram showing the orientations of volcanic rift zones (green lines) compared to the overall azimuth of the segment (HAWAII-10) which the volcanoes lie on (red line).

3.2 The Emperor Seamount Chain:

3.2.1 Spatial Distributions of seamounts along the Emperor Seamount Chain:

Despite the similarities between the Hawaii Seamount Chain and the Emperor Seamount Chain, they have a large number of differences as well. The spatial distribution of seamounts along the Emperor Seamount Chain is less clear in comparison to the Hawaii Seamount Chain. Due to the poor quality and lack of high-resolution bathymetric data available in this area of the Pacific Ocean, the identification of volcanic edifices and seafloor features are significantly more difficult to distinguish. Despite this, even to the naked eye, the spatial distribution of the Emperor Seamounts appears significantly better aligned in comparison to the Hawaiian Seamounts. However, there appear to be significantly greater and clearer hiatuses in volcanism along this seamount chain, for example between Jingu and Nintoku Seamounts (Figure 3.27).

The morphologies of the Emperor Seamounts also appear to have been affected significantly by underlying lithospheric structures. For example, the stretch of seamounts between Nintoku and Saga Seamounts, lies close to and potentially on top of the Shatsky Fracture Zone, and a majority of these seamounts all have an elliptical shape and are elongated in the same direction the fractures from the Shatsky Fracture Zone, as can be seen in Figure 3.27. There will ultimately be some error in determining the direction of the rift zones and elongations of these seamounts in this area due to the poor resolution bathymetric data which has been made available.

As with the Hawaii Seamount Chain, ‘cross track seamounts’ are seen at multiple points within this seamount chain. These are by the Tenji and Minnetonka Seamounts, with another potential one by the Lower Koko Seamount. They appear at the most ancient end of this seamount chain, (>65 Ma) meaning that it is hard to draw inferences as to what has potentially caused these due to the poor resolution bathymetric data available. These ‘cross-track’ seamounts do cover very long distances in the most northern parts of the Emperor seamount chain, one of which (including Tenji and Winnebago Seamounts) is nearly 200km long in total. Despite the poor-quality resolution of the bathymetric data, as with the mid-way seamounts, we have also likened the cross-track Emperor Seamounts to weaknesses within the oceanic crust, allowing volcanoes to emerge far from the volcanic chain’s ‘linear’ path.

One point within the Emperor Seamount Chain which has formed the basis of much debate about volcanic distributions is the Hawaii-Emperor Bend. The combination of small numbers of geological samples for chemical analysis and poor bathymetric data for this very old portion of the seamount chain at a point where major changes are present leads to further uncertainty surrounding the controls of volcano formation in the Hawaii-Emperor Bend. This further emphasises that this area without a doubt requires further study to fully understand the controls of volcano spacing in this area.

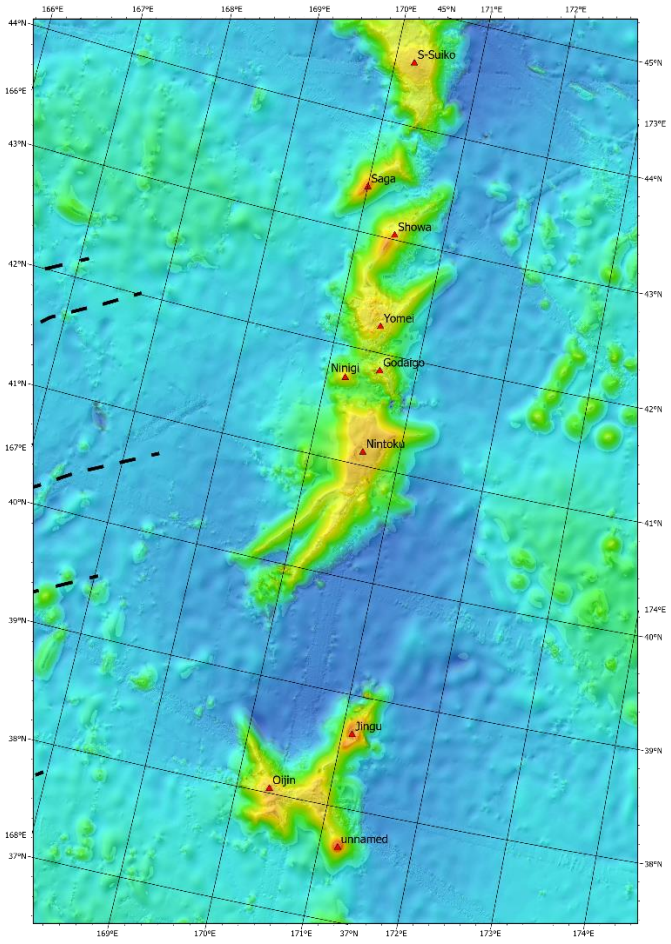

Figure 3.27: A Map showing the spatial relationships and morphologies of seamounts encompassing the Jingu and Suiko Seamounts. Red triangles represent individual volcanic edifices identified each of which labelled with the seamount's name. Black dashed lines represent the inferred position of the Shatsky Fracture Zone from Nakanishi et al., (1992a, 1992b, 1999).

3.2.2 Great Circle Distributions:

The Hough Transform was able to identify 12 potential alignments for the Emperor Chain, each of which had been rationalised and refined. Once these alignments were rationalised, 7 alignments were disregarded, leaving 5 optimal great circles encompassing the Emperor Seamount Chain (seen in Table 3.4 and Figure 3.28). The combined rms-misfit for all of these segments is 2.32km.

	Optimised misfit (km)	Length (km)	Point A Lon (°E)	Point A Lat (°N)	Point B Lon (°E)	Point B Lat (°N)	Azimuth (clockwise from N)
EMPEROR-01	8.5	193.8	172.424	31.633	172.009	33.787	002°
EMPEROR-02	8.9	191.8	171.714	32.130	171.432	34.104	004°
EMPEROR-03	7.7	434.9	171.936	34.744	171.026	38.696	000°
EMPEROR-04	1.9	482.3	170.622	41.020	170.155	45.212	007°
EMPEROR-05	5.7	417.1	169.153	47.652	167.465	50.551	352°

Table 3.4: Great Circle properties and rms-misfits for identified segments along the Emperor Seamount chain.

In contrast with the segmentation of the Hawaiian Chain, due to the poor resolution of available bathymetric data, lack of sampling and complexity of parts of this chain some of these segments are somewhat more speculative. For example, both of the segments, EMPEROR-01 and EMPEROR-02 encompass the seamounts which are involved with the Hawaii-Emperor Bend. This area of the seamount chain is highly debated, surrounding the controlling processes giving it its very distinct shape and appearance, therefore emphasising that these segments identified within this portion of the Emperor Seamount Chain must be treated with caution.

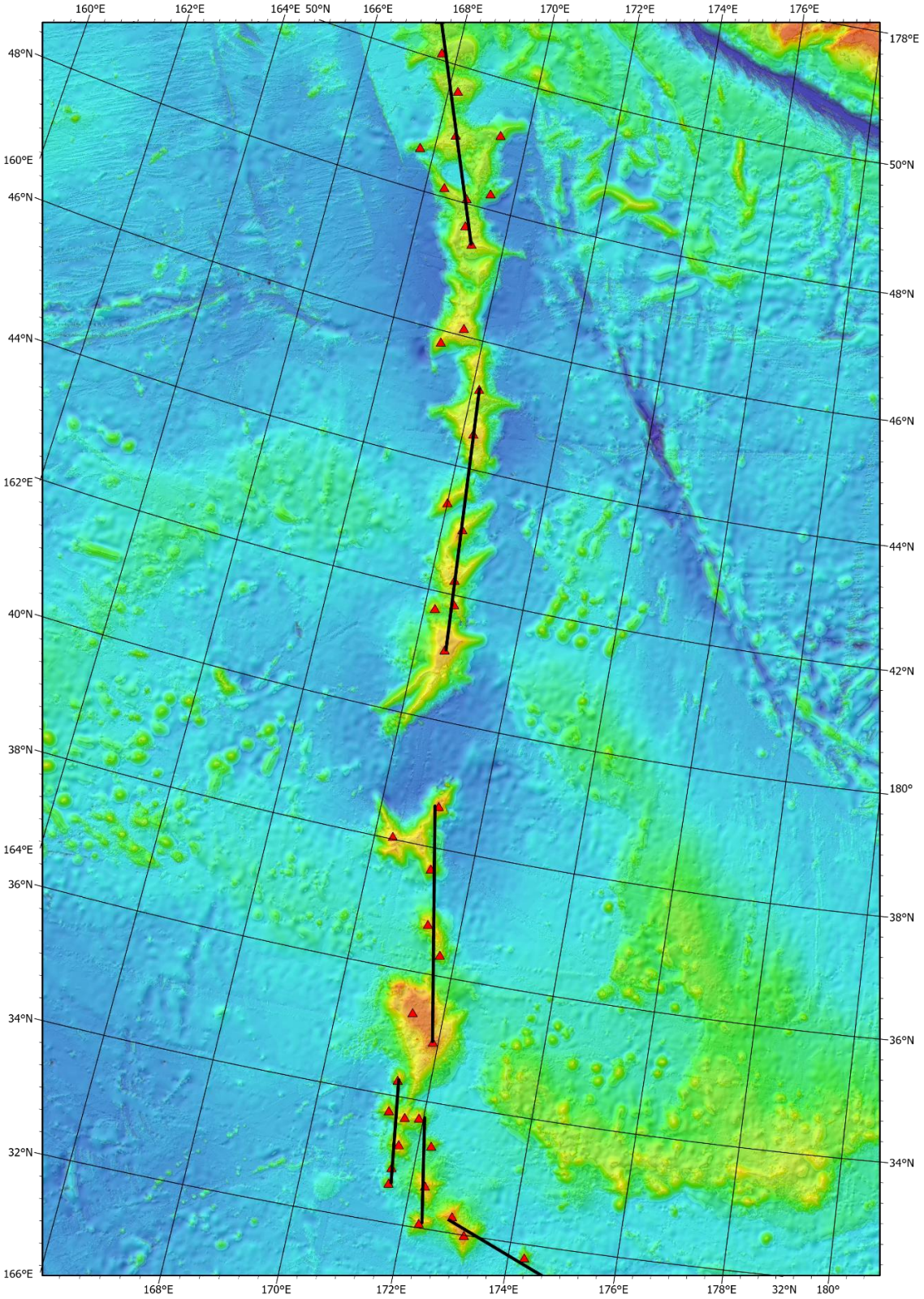

Figure 3.28: Map on a gnomonic projection demonstrating the segmentation of volcanoes within the Emperor Seamount Chain. Red triangles denote identified volcanic edifices, and black lines represent identified Great Circle Segments using the Hough Transform

3.2.3 Small Circle Distributions:

The distribution of volcanic centres along the Emperor Seamount chain has previously been analysed as representing a singular small circle Gaastra et al., (2022), and segmented small circles or en-echelon 'loci', as noted by Fiske and Jackson (1972), Jackson and Shaw (1975) and Jackson et al. (1975). Overall, the Emperor Chain has been tested as both a whole, singular small circle and as segmented small circles, the segments being comprising of the same volcanoes as the great circles were. The singular small circle gave an rms-misfit of 368.9km. In comparison, the segmented small circle model had rms-misfits between 0.06km and 21.2km and a combined misfit of 53.4km. All of the rms-misfits and properties of these segmented and singular small circles can be seen in Table 3.5.

	Misfit (km)	Radius (km)	Centre Latitude (°N)	Centre Longitude (°E)
EMPEROR-01	4.2	242.5	32.5624	169.7347
EMPEROR-02	8.3	248.6	33.0128	167.8771
EMPEROR-03	10.6	954.2	37.8841	182.0813
EMPEROR-04	9.7	935.2	42.0585	159.2293
EMPEROR-05	8.3	728.1	46.3460	159.6762

Table 3.5: Small circle properties and rms-misfits for identified segments along the Emperor Seamount Chain.

3.2.4 Great and Small Circle Distribution Comparison:

Figure 3.29 shows both ΔGC and ΔSC for the first segment identified within the Emperor Seamount chain (EMPEROR-01) situated on the Hawaiian Emperor Bend. As can be seen in Figure 3.29 this segment is one of few along the entire Hawaii-Emperor seamount chain where a great circle distribution is not best fitting for an identified segment where the ΔGC residuals do not best fit a random distribution about a straight line, and the ΔSC residuals are

not following an arcuate distribution. There is not a clear best-fitting model according to these residual graphs, emphasising the need for misfit statistics to determine between either a great or small circle fit.

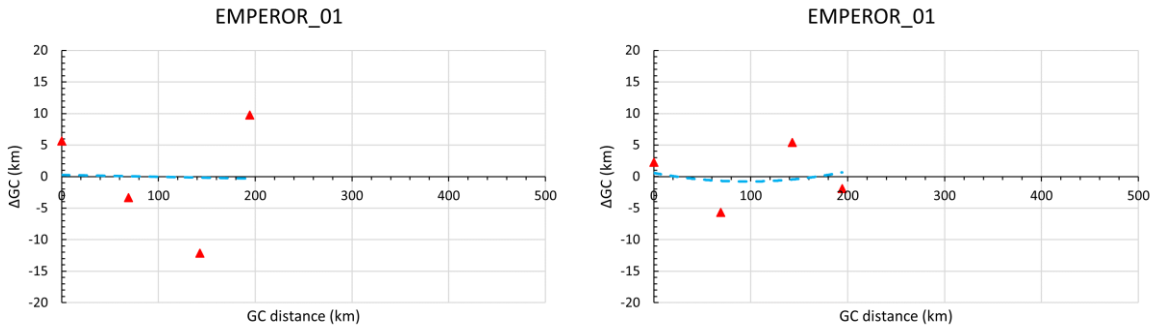

Figure 3.29: Residual plot showing the great circle and small circle distributions of volcanoes within the segment EMPEROR-01. Red triangles represent individual volcanic centres. The blue dashed line represents either the respective great circle or small circle the volcanoes are distributed along.

EMPEROR-02, is more ambiguous surrounding whether it best fits a great or small circle much like the segment HAWAII-10, as seen in Figure 3.30. The shapes produced form both the ΔGC and the ΔSC do not coincide with what is laid out in Figure 3.7 to be best fitting as a great circle. Due to this evidence , it is believed that the segment EMPEROR-02 is best described by a small circle distribution. However, due to uncertainties within these datasets and large misfits within both of these models the use of misfit statistics such as the AICc will help to determine between either a great or small circle fit for this segment. Furthermore, along the entire Hawaii-Emperor Seamount Chain, this is the only place (except for the active segments of Hawaii) where there are two parallel segments. In comparison to the two parallel segments in the Hawaii Chain, both EMPEROR-01 and EMPEROR-02 appear to have worse fitting ΔGC and ΔSC residuals.

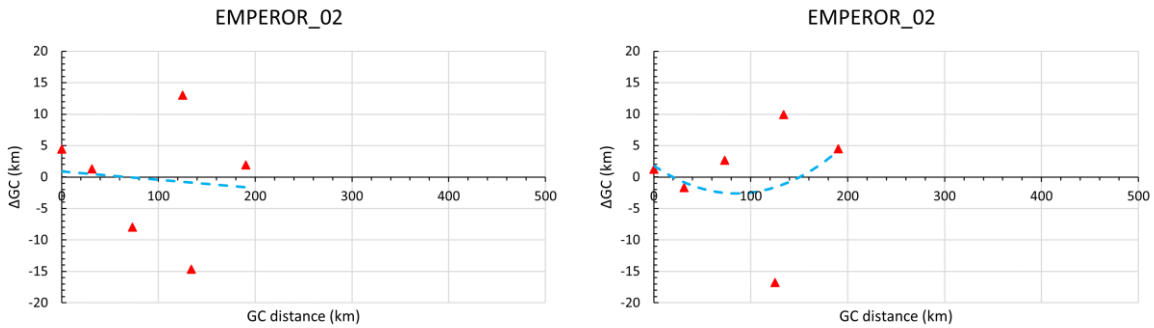

Figure 3.30 1:Residual plot showing the great circle and small circle distributions of volcanoes within the segment EMPEROR-02.

EMPEROR-03, can be best described by a great circle distribution. Panel A in figure 3.31 shows a relatively random ΔGC distribution surrounding a straight line, whereas Panel B shows a somewhat arced organisation of the volcanoes along this segment for the ΔSC. However this is not very clear and as previously mentioned with other segments, EMPEROR-03 would benefit from additional statistical analysis in order to determine the best fitting distribution of volcanoes which this segment encompasses.

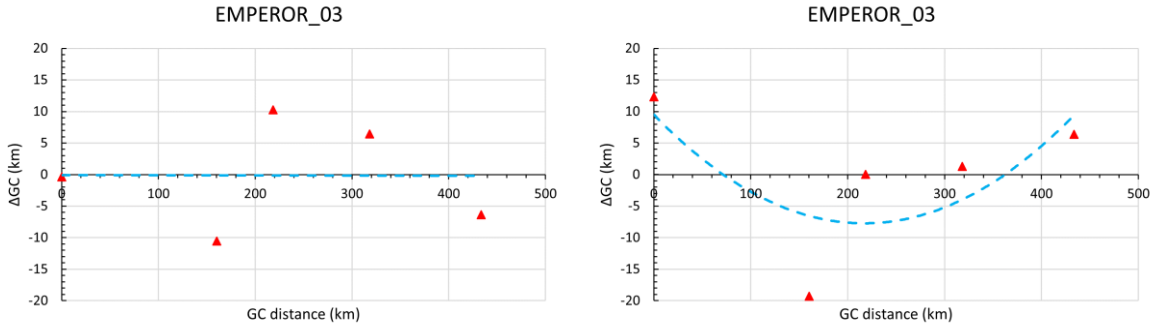

Figure 3.31 1: Residual plot showing the great circle and small circle distributions of volcanoes within the segment EMPEROR-03.

Looking at Panels A and B in Figure 3.32, it can evidently be seen that EMPEROR-04 fits a great circle distribution remarkably well. Within Panel A, the volcanoes are distributed randomly around a straight line with minimal misfit, whereas in Panel B, the volcanoes are

distributed with minimal misfit in an arced shape, showing that this segment of volcanoes is not described by a small circle distribution and in fact best described by a great circle.

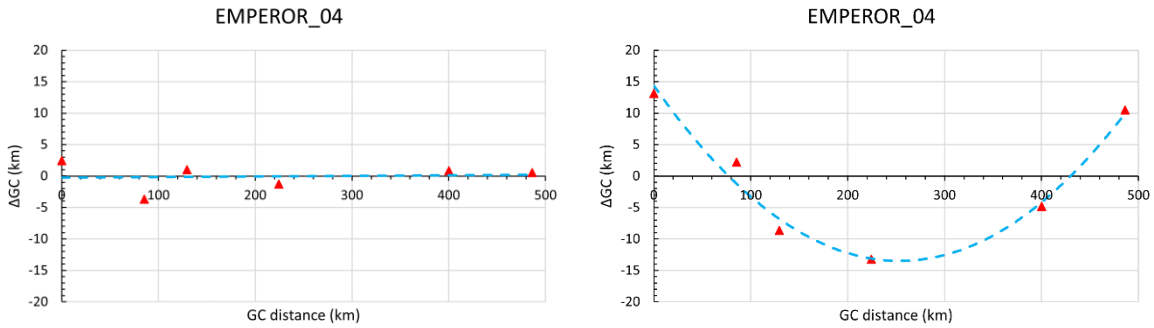

Figure 3.32 1: Residual plot showing the great circle and small circle distributions of volcanoes within the segment EMPEROR-04.

In Figure 3.33, the segment EMPEROR-05 can be seen to be following a random distribution surrounding a straight line for ΔGC, as seen in Panel A. The volcano with the greatest misfit along this distribution is (Suizei Seamount), lying ~12km off the best fitting line. Panel B within Figure 3.33 shows how the volcanoes within the segment EMPEROR-05 are distributed randomly along an arc for a ΔSC residual. These volcanoes are randomly distributed along this line, demonstrating that this organisation of volcanoes is not able to be described by a small circle distribution and that the best fitting organisation for these volcanoes is a segmented great circle.

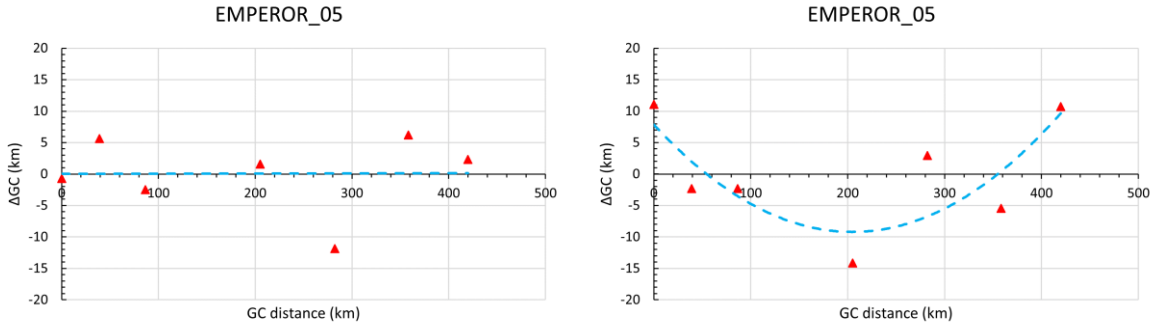

Figure 3.33 1: Residual plot showing the great circle and small circle distributions of volcanoes within the segment EMPEROR-05.

Further to this, drawing on results from Chapter 2.2, results from conducting the Akaike information criterion correction on the segments from the Emperor Seamount Chain have been compared in Table 3.6. As can be seen, every segment where the AICc was able to be calculated is better fitting with a segmented great circle distribution in comparison to segmented small circle. EMPEROR-01 has the worst fitting great circle distribution out of the five segments with an AICc value of 23.42, whereas EMPEROR-04 is the best fitting by a large amount with an AICc value of 11.50, 6.05 lower than the next best fitting segment, EMPEROR-05.

	Segmented GC	Segmented SC
EMPEROR-01[1]	23.42	-
EMPEROR-02	19.38	29.02
EMPEROR-03	18.88	40.27
EMPEROR-04	11.50	29.82
EMPEROR-05	17.55	26.89

Table 3.6: Comparison of AICc values for the Emperor seamount chain segments for both great and small circles. [1] Denotes a segment where the AICc is not available for small circles due to having too small a sample size of volcanoes.

3.2.5 Morphologies of Seamounts Along the Emperor Seamount Chain:

Both the orientation of rift zones and principal axes of elongation were plotted for each separate segment along the Emperor Seamount Chain. This was done in order to further understand if processes leading to segmentation of volcanoes could potentially impact individual edifices as well as well as to draw potential differences from the Hawaii Seamount Chain. In both Panel a and Panel b of Figure 3.34 both principal axes of elongation and submarine rift zones align poorly with the overall azimuth of the segment EMPEROR-01. As

can be seen in Panel a, the trend of submarine rift zones for this segment, in contrast to the Hawaii Seamount Chain, are all oblique to the orientation of the segment. Similar to the Hawaii chain, no volcanic elongations appear to be aligning with the segment's orientation, with two main preferred directions for elongation.

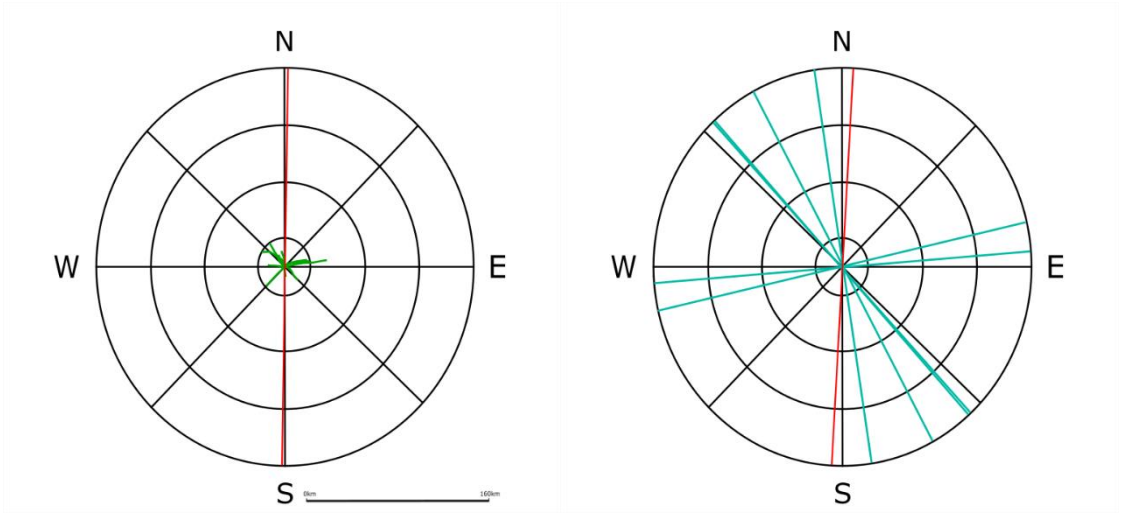

Figure 3.34 1: (a) Rose diagram showing the orientations of volcanic rift zones (green lines) compared to the overall azimuth of the segment (EMPEROR-01) which the volcanoes lie on (red line). (b) Rose diagram showing the orientation of principal axes of elongation (blue lines) for separate volcanic edifices in comparison to the overall azimuth of the segment (EMPEROR-01) which the volcanoes lie on.

In the segment EMPEROR-02, volcanic rift zones, much like in the segment EMPEROR-01, do not follow the same trend as the segment's azimuth, as can be seen in Panel a of Figure 3.35. The rift zones along this segment appear to be mostly perpendicular to the segment direction on its Western side whilst predominantly oblique to the segment on its Eastern side. Panel b of Figure 3.35 shows how principal axes of elongation along this segment have no preferential orientation, as opposed to previous segments where both the Emperor and Hawaii Seamount chains have preferred orientations.

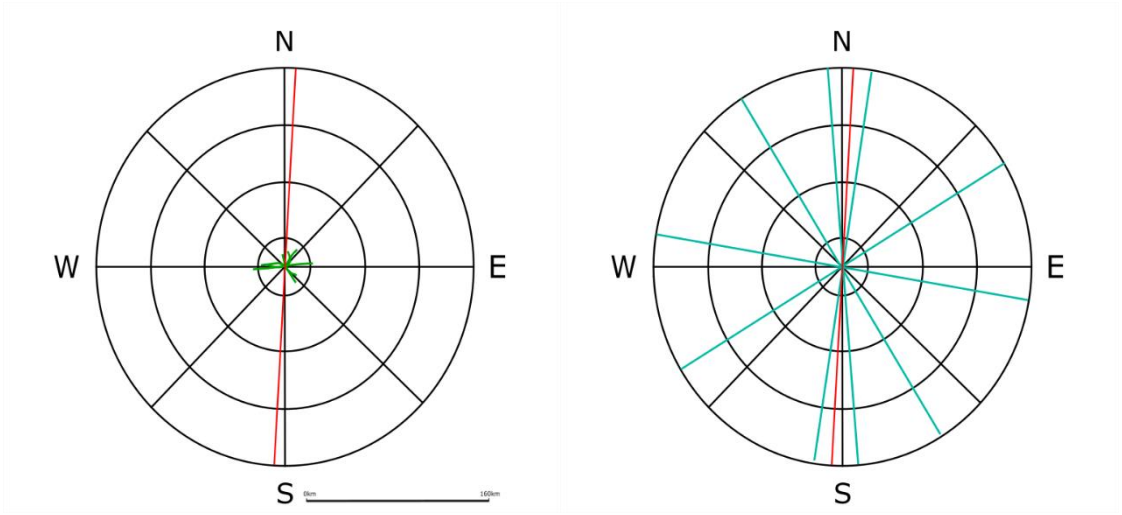

Figure 3.35 1: (a) Rose diagram showing the orientations of volcanic rift zones compared to the overall azimuth of the segment (EMPEROR-02) which the volcanoes lie on. (b) Rose diagram showing the orientation of principal axes of elongation for separate volcanic edifices in comparison to the overall azimuth of the segment (EMPEROR-02) which the volcanoes lie on.

Figure 3.36 Panel a demonstrates that in the segment EMPEROR-03, rift zones align a lot better with the segment in comparison to other segments within the Emperor seamount chain. However, as a whole, there is still a minimal number of rift zones aligning with the segment azimuth within EMPEROR-03, with the majority showing a preferred orientation between 20º and 90º. Principal axes of elongation along this segment mostly differ from what has been observed so far in the two prior segments. Panel b of Figure 3.36 shows that, excluding one measurement of elongation, all of the volcanoes' principal axes of elongations are preferentially aligned between 25º and 40º or 205º and 220º.

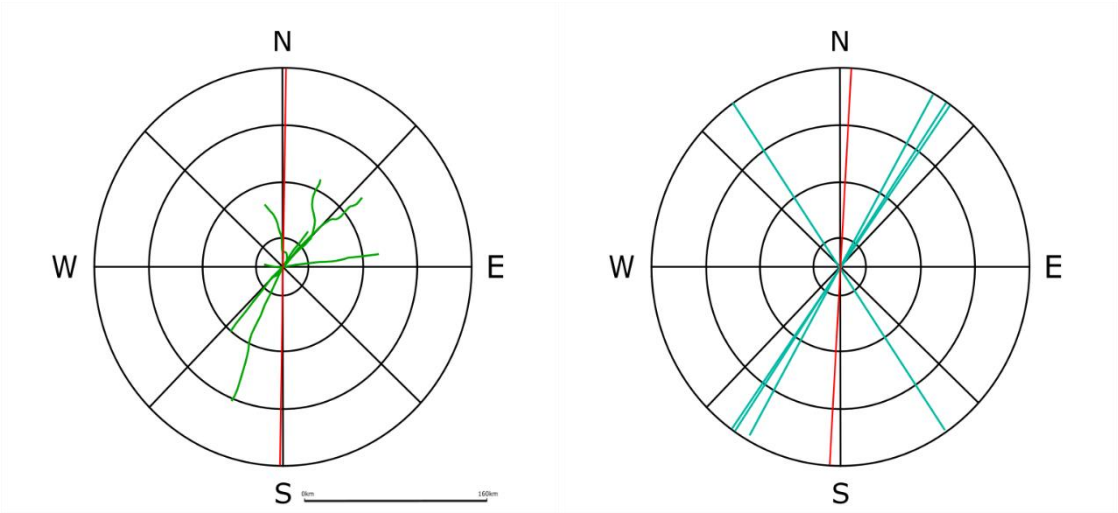

Figure 3.36 1: (a) Rose diagram showing the orientations of volcanic rift zones compared to the overall azimuth of the segment (EMPEROR-03) which the volcanoes lie on. (b) Rose diagram showing the orientation of principal axes of elongation for separate volcanic edifices in comparison to the overall azimuth of the segment (EMPEROR-03) which the volcanoes lie on.

The segment EMPEROR-04 is different from others within the Hawaii and Emperor Seamount Chains, as the Shatsky Fracture Zone is inferred to potentially underly it (Nakanishi et al., 1992b, 1999). Figure 3.37 demonstrates the average azimuth of the multiple fracture zones in this area. Additionally, it can be seen in Figure 3.37 that the length of rift zones within this segment are considerably larger than in other segments of the Emperor Seamount Chain, leading to the inference that this was a period where there was a considerably larger amount of active volcanism. Rift zones do not appear to adopt the segment orientation whilst they do appear to loosely adopt a similar azimuth to the underlying Shatsky Fracture zone. Furthermore, Panel b within Figure 3.37 shows that similar to the rift zones in this segment, principal axes of elongation do not align with the segment orientation at all whilst also loosely following the same azimuth as the Shatsky Fracture Zone (up to 30º off) whilst there are still some axes of elongation which do not follow this trend, a majority do loosely align with the Shatsky Fracture Zone.

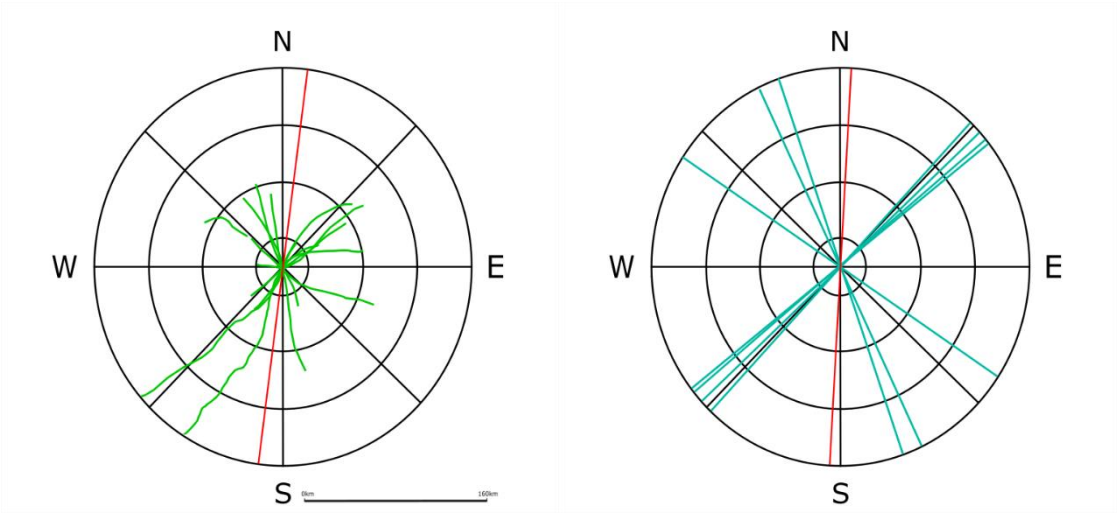

Figure 3.37 1: (a) Rose diagram showing the orientations of volcanic rift zones compared to the overall azimuth of the segment (EMPEROR-04) which the volcanoes lie on. (b) Rose diagram showing the orientation of principal axes of elongation for separate volcanic edifices in comparison to the overall azimuth of the segment (EMPEROR-04) which the volcanoes lie on. The pink line represents the average azimuth of the Shatsky fracture zone which underlies the segment of volcanoes.

Figure 3.38 illustrates that, similar to the first three segments in the Emperor seamount chain, volcanic rift zones do not appear to follow a trend similar to that of the segment which they lie on. The majority of the rift zones within this segment all lie oblique to perpendicular to the segment. Furthermore, whilst these rift zones also do change in propagation direction, they still do no align strongly with the segments orientation after this. Unlike previous segments from both the Hawaii and Emperor Seamount Chains, information surrounding principal axes of elongation for this segment has not been gathered. This is due both to the clustered nature of these large volume volcanoes, and the fact that they have been heavily eroded from subaerial and submarine processes making elongations of these volcanoes incredibly difficult to identify.

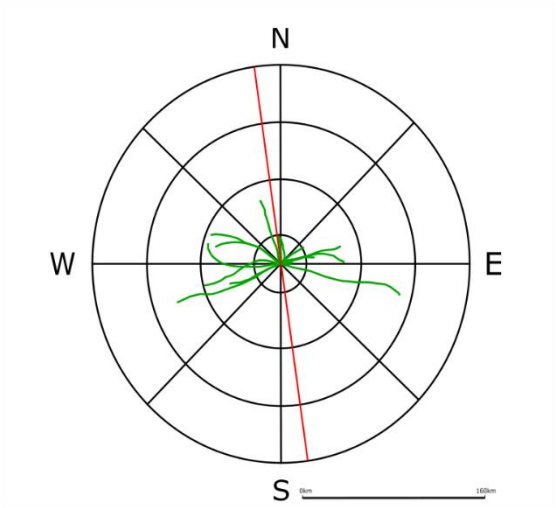

Figure 3.38 1: Rose diagram showing the orientations of volcanic rift zones compared to the overall azimuth of the segment (EMPEROR-05) which the volcanoes lie on.

Throughout the Emperor Seamount Chain, there is a very poor correlation between the orientation of individual segments of volcanoes identified and observed orientations of volcanic rift zones. Although something of a correlation between rift zone orientations and fracture zone azimuth could be drawn within the segment EMPEROR-04, it is not a strong enough correlation upon which to base conclusions. Elongations of seamounts within the Emperor Seamount Chain were significantly more variable in comparison to rift zones. Across the Emperor Seamount Chain there are segments where there appears to be no preference in axes of elongation as well as others where multiple preferential axes of alignment were found. Similar to the volcanic rift zones within this seamount chain, principal axes of elongation also align with the Shatsky Fracture Zone underlying one of the segments. Overall, it can be seen that the trends seen within the Emperor Seamount Chain are very different in comparison to the Hawaii Seamount Chain. This can hint towards potential separate causes for both the Hawaiian and Emperor Seamount Chains' segmentation or, more likely, differences in localised stresses or plate structure influencing the formation of these volcanoes.

3.3 Summary:

In summary, as can be seen from Table 3.7 a segmented great circle distribution is a significantly better explanation for the distribution of volcanoes along both the Hawaii and Emperor Seamount Chains. This table shows that small-circle distributions for the Hawaii-Emperor seamount chain produce significantly larger AICc results than Great circles. The Emperor Seamount Chain is the best fitting portion of the entire Hawaii-Emperor Seamount Chain, having under half (79.66) the AICc value that the Hawaii Seamount Chain does alone (189.89). There are 10 segments within the Hawaii Seamount Chain for which none of the 8 AICc statistics which were able to be calculated indicated that a small circle distribution was the best fitting of these. Likewise, within the 5 segments of the Emperor Seamount Chain none of the 4 segments where AICc statistics were able to be calculated for both small and great circles were best described by a small circle distribution. Additionally, for the Hawaii seamount chain alone, the Small Circle model produces an AICc statistic 132% larger than that of a Great Circle model, likewise, for the Emperor Seamount chain a Small Circle model produces an AICc value 154% higher than that of a Great Circle model. Combining both the Hawaii and Emperor Seamount chains would produce a small circle AICc statistic value 142% greater than what a great circle would. This large discrepancy between how well a Great Circle model and a Small Circle Model fit the distribution of volcanoes along the Hawaii Emperor Seamount chain only proves to reinforce that a great circle distribution is the model to describe the distribution of these volcanoes. Overall, we are able to present 12 of the 15 identified segments along the Hawaii-Emperor Seamount Chain which are best described by a great circle distribution utilising both the AICc statistic or residual graphs with the remaining three segments unable to be determined due to too few volcanoes lying on them to carry out AICc testing.

One of the more uncertain areas within the Hawaii-Emperor Seamount Chain is the Hawaiian-Emperor Bend, a highly complex area both morphologically and geodynamically,

resulting in much debate surrounding the cause of volcanism here. One of the three segments unable to be constrained to a great circle distribution belonged to the Bend, whilst one of the more uncertain results within the residual graphs also belonged to the Hawaii-Emperor Bend. This indicates that there are potentially large changes within the processes which create volcanism in this part of the Hawaii-Emperor seamount chain.

Overall, it is evident within the Hawaii-Emperor Seamount Chain that throughout time separate segments have formed, each of these segments being able to be defined by individual great circles as can be seen in Figure 3.6 and 3.28.

	Segmented SC	Single SC	Segmented GC
Hawaii Chain	251.43	210.69	189.89
Emperor Chain	122.47	92.79	79.66
Hawaii-Emperor Chain	375.21	287.67	265.54

Table 3.7: Comparison of AICc values of both single small circles and segmented great and small circles, for the Hawaii chain the Emperor chain, and them both combined.

Figure 3.39 shows a comparison of age ranges between individual segments along the first 10 segments of the Hawaii-Emperor Seamount Chain. Where segments of volcanoes are present, there are (mostly) well distinguished hiatuses between each segment, with the most prevalent either side of the seventh segment (HAWAII-07). The final segment displayed in Figure 3.39 shows a highly variable range in ages of volcanoes, which may be as a result of poor quality radiometric data, or an irregular and unexpected pattern of magmatism at this part of the Hawaii Seamount Chain. Excluding this volcano age, there is a very large age gap between this segment and the segment created after it. Both of these points further reinforce the need to examine this segment in more detail to explain its unexpected morphologies and age ranges.

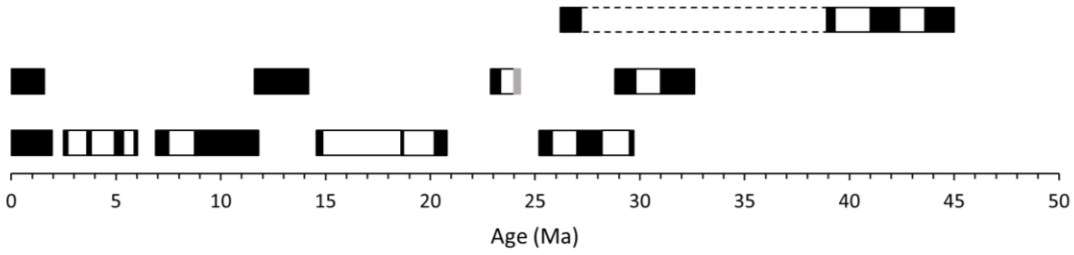

Figure 3.39: Timeline depicting the age ranges of individual segments within the Hawaii seamount chain. Each bar represents a separate segment. Black blocks depict known age ranges of volcanoes sitting on a certain segment. A grey block represents an estimated time for the last volcano of a segment where the age of only one seamount or volcano was available. The dashed edges of a box represent an uncertain period of time towards a potential anomalous radiometric age.

3.4 Key findings:

The key findings and results from this section are as follows:

- A segmented great circle distribution best describes volcano spacing in the Hawaii Seamount Chain in comparison to segmented small circle and single small circle distributions.
- Volcano spacing is significantly better fitting in the Hawaii Seamount Chain for volcanoes younger than 23 Ma.
- A segmented great circle distribution also best describes volcano spacing in the Emperor Seamount Chain in comparison to segmented and singular small circle distributions.
- The Emperor Seamount chain is closer fitting with a great circle distribution than the Hawaii Seamount Chain.

Chapter 4. Discussion

4.1 What best describes the distribution of volcanoes along the Hawaii-Emperor Seamount Chain:

Having completed quantitative analysis regarding how well different alignment models fit the Hawaii-Emperor Seamount Chain, it can be argued that a great circle distribution is the best fitting for this collection of volcanoes. Tables 3.3, 3.6 show that for each induvial segment, as well as the best way to describe volcano distribution in the Hawaii Emperor Seamount chain is by a great circle distribution. Further to this, Table 3.7 further reinforces these findings by demonstrating the large discrepancy between Small Circle and Great Circle models, with the Small Circle model producing AICc results for the entire Hawaii-Emperor seamount chain >140% larger than that of a Great Cricle model where the smallest values represent the best fitting. These results have the potential to point away from the fact that a rotating 'cap' (a tectonic plate moving about an axis of rotation which can be seen in Figure 1.3) over a fixed magma source (potentially a mantle plume) is able to work as the leading control of the distribution of volcanism. As discussed in section 1.2.1 this would create small circle volcano distributions. However, as shown through statistical analysis using the AICc a great circle model best describes the distribution of volcanoes here. Refinements to this model must therefore be made in order to allow for the propagation of magma through the lithosphere in order to create volcanoes with a great circle distribution. A propagating fracture such as that suggested by Fiske and Jackson (1972), Jackson et al. (1972, 1975) and Jackson and Shaw (1975), or other controls which may describe a small circle distribution or other non-great circle geometries can therefore be assessed as also not being leading controls of the distribution of ocean island volcanism.

Throughout this project, both the Emperor and Hawaii Seamount Chains have been treated as separate chains as a result of the large changes in plate tectonics resulting in their different and unique morphologies. However, it is also likely that these chains could be created through the same processes, operating at differing magnitudes or orientations. It has been

noted, through the use of the AIC statistic, that the Emperor Seamount Chain fits a segmented great circle distribution better than the volcanoes along the Hawaii Seamount Chain. Additionally, as previously noted, towards the youngest end of the Hawaii Seamount Chain (after ~23 Ma) the strength of the great circle distribution describing segments greatly increases, according to the AICc statistic. Both of these changes in the strength of fit for segmented great circle distributions could point towards a potential geodynamic control which may influence how closely magmatic loci follow a great circle distribution. However, due to the limitations of the AIC statistic with respect to small sample sizes (Figure 4.1), this observed change in values may be as a result of an increase in sample sizes for volcanic segments approaching the youngest end of the volcanic chain.

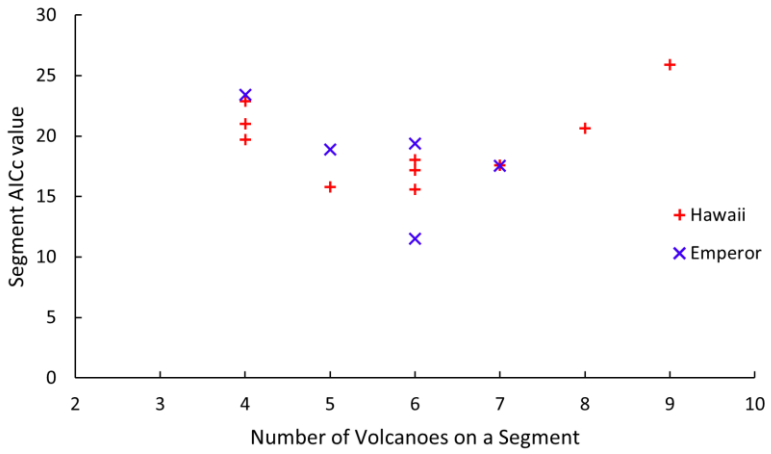

Figure 4.1: A plot of n vs AICc value for individual segments along the Hawaii-Emperor Seamount Chain.

As can be seen within Figures 4.2 and 4.3, both the Hawaii and Emperor Seamount Chains are separated into multiple segments, each of which with a unique azimuth and length. In the Hawaii Seamount Chain, the Hough Transform has identified two near-parallel segments within the Hawaiian archipelago which can be interpreted to represent both the Loa and Kea trends which are present within this portion of the Hawaii Seamount Chain. The segments within this seamount chain appear to flatten out, approaching 90º, until the fifth

segment, beginning with French Frigate Shoals where the segment azimuth aligns in a very similar way with the first two segments, between 310-315º. Additionally, at other points along this chain, the azimuths of multiple segments align very closely, one example being three segments aligning at angles between 288º and 294º. In contrast, excluding the final segment of the Emperor Seamount Chain, the azimuths of these segments all lie close to one another (between 000º and 007º). This raises questions as to whether there is an underlying variable which may influence the orientations of segments, especially considering the somewhat repetitive azimuths along the Hawaii Seamount Chain.

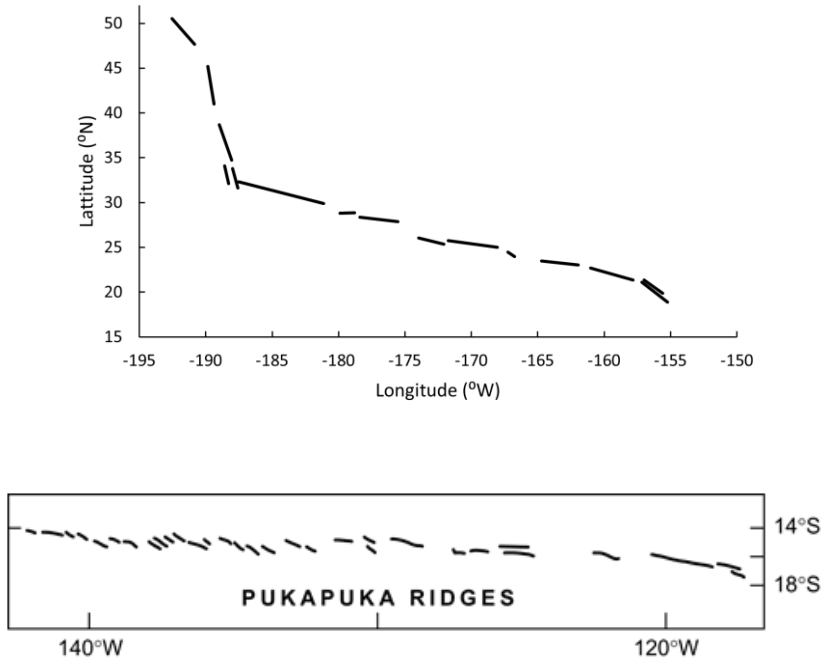

Figure 4.2: Map demonstrating the distribution of separate great circle segments along the Hawaii-Emperor Seamount Chain (top), in comparison to the en-echelon curved ridges identified in the Pukapuka Seamount Chain by Winterer and Sandwell (1987)(bottom).

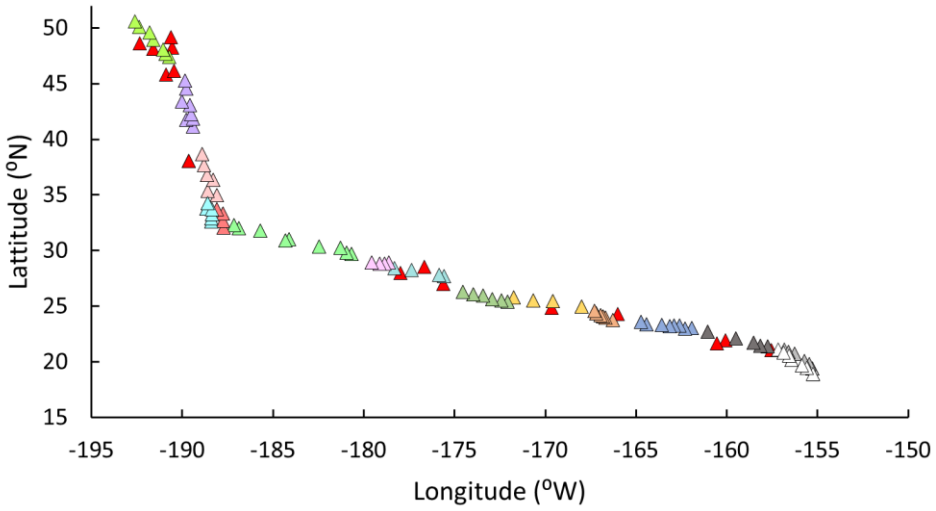

Figure 4.3: Map showing the distribution of volcanoes along the Hawaii-Emperor Seamount Chain, Red triangles represent volcanic edifices which have been excluded from spatial analysis (Chapter 3.1.1). Groups of different coloured triangles represent individual identified segments and the volcanoes that lie within them.

4.2 Controls over the formation of segments within ocean island chains:

Having recognised that a great circle distribution is the best fitting geometry for volcanoes along the Hawaii Seamount Chain, an explanation for this distribution is required. Multiple ideas which could potentially cause a regular aligned distribution of volcanoes are as follows: periodicity of mantle upwellings (i.e. pulsing) or deformation/instabilities/failures of mantle plumes in a repetitive periodicity; underlying palaeotectonic (or pre-existing) features causing a preferential alignment of volcanoes; neo-tectonic events at the edges of the plate, creating weaknesses within the plate to be exploited by magmatism. The term ‘neo-tectonic’ we use to refer to tectonic events which occur contemporaneous with magmatism which could potentially lead to a change in distribution of ocean island volcanoes. Palaeotectonic features refer to significantly older or ancient seafloor features which may influence the distribution of ocean island magmatism.

Turcotte and Oxburgh (1973)explored the idea of preexisting features within oceanic lithosphere influencing the formation of ocean island chains. They attribute thermal stresses from the cooling of the lithosphere and membrane stresses from changes in radii or curvature of tectonic plates, to the creation of ocean island chains. Following much observation, seamount chains such as the Pukapuka Chains are firmly believed to have been formed as a result of cracks within the lithosphere, allowing magma to arise forming en-echelon lines of volcanoes. However, one problem with this is that this hypothesis can struggle to explain the large topographic swell underneath the Hawaii Seamount Chain. This swell is commonly attributed to the upwelling of mantle material, uplifting the lithosphere to create the observed structure Lynch, (1999). As can be clearly seen in Figure 4.2 (a) in comparison to Figure 4.2 (b), the segments identified with in the Hawaii Seamount Chain clearly do not follow these morphologies, instead having much larger gaps between these lines of volcanoes.

An issue with the idea that pulsing plumes could cause the apparent segmentation of the Hawaii seamount chain, as provisionally identified by Whitehead (1982) is that this hypothesis cannot explain much of the observed seamount morphologies within the Hawaii-Emperor Seamount Chain. As previously mentioned, it has been hypothesized that the upwelling of mantle plumes varies throughout time, resulting from the plume ‘pulsing’. This pulsing is then a direct control on the observed volume of magma erupted and would also be a cause of the observed breaks in segmentation. One problem with this theory is that to describe or create a model for pulsing mantle plumes which encompasses an irregular pulsing through the mantle. This must also take into consideration different pulses having different volumes as well as interacting with the lithosphere differently to create the vast diversity in volcanism that is seen in the Hawaii-Emperor seamount chain today, such as parallel seamount chains, as well as changes in direction of volcanism. These particular models for the creation of ocean island chains evidently do not fit, firstly as a result of the limitations of the lab-controlled experiments which may not entirely reflect the reality of magma ascending

in the mantle, and secondly due to an inability to model such complex processes which may be occurring.

To explore why plate forces might be related to segmentation of volcanic chains, plate reconstructions were used along with ages of volcanic centres along the Hawaii-Emperor Seamount Chain. A comparison between tectonic events and ocean island segmentation was able to be completed, Figure 4.4 shows age ranges of segments as shaded boxes, where the shaded regions represent the ages of volcanoes within each segment as well as their errors. Throughout this 'segment timeline' there are numerous gaps or overlapping periods between different segments volcanic activity which could potentially represent periods in time where geodynamic processes change or reorganise to form separate well-aligned volcanic edifices. Age ranges of major tectonic events involving the pacific plate, selected from reconstructions of the Pacific plate, have been plotted against the 'segment timeline' (Figure 4.4). This aims to provide an explanation as to the driving geodynamic processes behind the observed segmentation of the Hawaii-Emperor Seamount Chain. A table showing all of the tectonic events is shown in Appendix C.

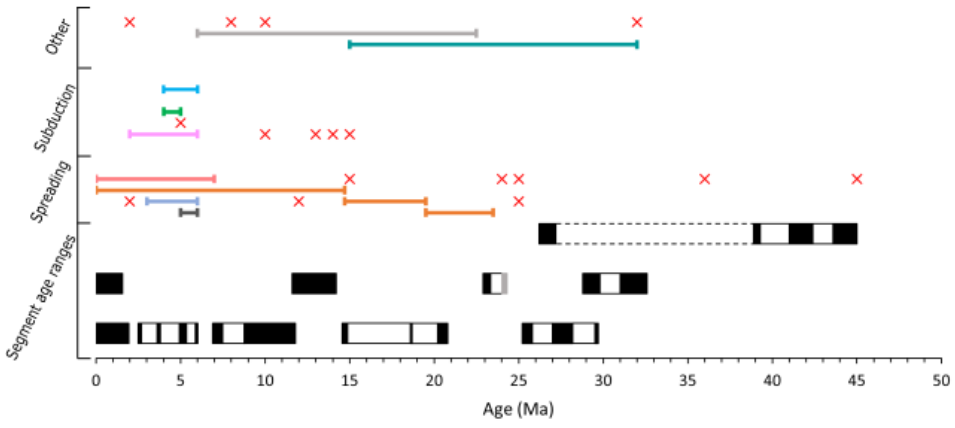

Figure 4.4: A timeline showing the comparison between age ranges of volcanic segments in to age ranges and dates of tectonic events surrounding the pacific plate, found using plate

reconstructions. Tectonic events have been classified into three different categories: Those related to seafloor spreading; those related to subduction zones; and other tectonic events (i.e. changes of pate motion). Red crosses and coloured bars denote separate tectonic events. Bars represent age ranges of volcanic segments, where the known ages of volcanoes within segments are shaded in black. In one instance only a single volcano within a segment has a radiometric age obtained, here an estimate of the age of the 'oldest' or furthest west volcanoes age has been made, however should be treated with caution. The dashed lines of one bar represents an age range of a segment which is somewhat uncertain, as this seamount is ~13Ma younger than the rest of the seamounts belonging to this segment, it is noted that this could be as a result of chemically altered samples before the radiometric dating has been done.

Figure 4.4, builds on Figure 3.39 from Chapter 3.3, to reveal a comparison between age ranges of segments and dates or date ranges of tectonic events related to the edges of the pacific plate. Each one of these events we classify as 'neo-tectonic,' i.e. occurring contemporaneously with the magmatism of the Hawaii-Emperor Seamount Chain. Appendix C, shows a full list of these events which have been plotted and a description of what each individual point refers to. One major point of interest which can be seen within Figure 4.4 are the three individual spreading events which are related to the genesis of the Cocos and Nazca plates. The first spreading event, begins at ~23 Ma, continuing until the second spreading event takes over at ~19.5 Ma, until the final spreading event begins at ~14 Ma. These spreading events coincide very well with the observed strengthening of the segmented great circle trend, after the Pearl and Hermes Atoll (segment HAWAII-08) . Many other events such as initiation of subduction and genesis or extinction of back arc spreading surrounding the West Pacific Margins have also been mapped onto Figure 4.4, some of these aligning with the changes in modelled to be occurring in the Eastern Pacific. Furthermore, throughout the history of the Hawaii-Emperor Seamount Chain, not only do these neo-tectonic events align with the strengthening of fit to a great circle distribution, they also align with times for the origin

and ends of individual segments. For example, 4 neo-tectonic events, related to both the East and West Pacific align with the break between segment 7 and 8, at ~ 25 Ma, as well as with segments 5 and 6 at ~15 Ma. These events are: the new Guinea Passive margin colliding with the leading edge of the East Philippines-Halmahera-New Guinea arc system at ~25 Ma; the stopping of the South Fiji Basin and Solomon Sea spreading at 24-25 Ma; the ceasing of spreading in the Shikoku Basin, Parce Vela Basin and South China Sea at ~15 Ma; and the Ayu trough opening in the Caroline plate Hall, (2002); Liu et al., (2017). Seven neo-tectonic events related with the West Pacific also align with segments 3 and 4, which are noted in Appendix C.

It is hypothesized that these multiple changes in the tectonics surrounding the Pacific, which will alter the tensional stress regimes within the Pacific plate have a controlling factor over the emplacement of volcanic edifices. This will focus upwelling magmatism over the Hawaiian plume into a central area of weakness, creating an aligned track of volcanoes on a moving plate. This, can help to explain why we observe a single track of volcanoes, opposed to scattered volcanism, over a large swell created by upwelling magma, including other factors such as volcanic conduits being affected by horizontal advection forces Olson and Singer, (1985).

4.3 Controls over volcano morphologies within ocean island segments:

Morphologies of seamounts within both the Hawaii and Emperor Seamount Chains are analysed in order to recognise if geodynamic controls which impact on the creation of volcanic segments also have an effect on the morphologies of seamounts which are observed along them. Overall, there appears to be no major changes of volcano elongation in comparison to their respective segment's orientation. Across both the Hawaii and Emperor volcano

elongations appear to be within a ~90º arc that lies oblique to the segment's azimuth. On only one instance does this trend appear to be broken, within the fourth segment of the Emperor Seamount Chain where a major fracture zone appears to potentially underly this segment. One explanation for this is that the major control over the morphologies of volcanic edifices are localised stresses within the plate created by volcanic loads, such as those suggested by Hieronymus and Bercovici (1999) and Fiske and Jackson (1972). However, a plate structure control, in this case fracture zones within oceanic lithosphere, appear to have a dominating contribution to the morphology of seamounts, as clearly seen within the segment EMPEROR-04 where seamount elongations begin to align with the Shatsky Fracture Zone.

Furthermore, as previously mentioned, Fiske and Jackson (1972) explore how gravitational forces and localised plate stresses affect the formation of volcanic rift zones (Figures 1.7 and 1.8) . They found that rift zones within 'isolated' volcanic edifices (those that are not proximal to influence of gravitational stresses from nearby volcanoes) within the Hawaiian archipelago align with the apparent direction of plate motion for that period. A similar method has been employed to compare the orientations of volcanic rift zones to segment orientations, opposed to the plate motion along the entire Hawaii-Emperor Seamount Chain. The first two segments follow very similar trends as to what was observed in Fiske and Jackson (1972), with large rift zones from 'clustered' volcanoes propagating oblique to the segment orientation and smaller rift zones from 'isolated' edifices aligning with the segment. In contrast, further along the Hawaii Seamount Chain, volcanic edifices are not as closely clustered in comparison to the subaerial domain of the chain. These observations would point towards a potential relationship between the volcanic rift zones for the remainder of the Hawaii Seamount Chain, and segment orientation. For the Hawaii Seamount Chain, it can be seen that, generally, a similar trend to the first two segments is present. Volcanic rift zones for the remaining eight segments all have longer rift zones, extending >70km in the extremer cases, which do not follow similar directions to the segments. However, some of these rift zones change their direction of propagation towards the direction of the segment. The smaller rift

zones within these segments can be from ~50% to ~10% shorter than the longest, however they do tend to align better with segment orientation.

Rift zones belonging to volcanoes lying within the identified segments along the Hawaii-Emperor Seamount Chain are believed to have a relationship with the stresses related to the formation and orientation of volcanic segments. Rose diagrams, seen within Chapters 3.1.5 and 3.2.5 show how the rift zones of volcanoes relate to the orientations of volcanic segments. They show that there is a minimal correlation between rift zone orientations closer to the volcano, whilst the further rift zones spread from a volcanoes magmatic centre the closer their orientations correlate to a segment's azimuth.

4.4 Final Observations:

Overall, a segmented great circle distribution for the Hawaii-Emperor Seamount Chain has been identified, with the Hawaii Seamount Chain consisting of 10 segments, and the Emperor Chain composed of 5, 2 of which belong to the Hawaii-Emperor Bend. The controls of this segmentation have been inferred to be linked to neo-tectonic events surrounding the Pacific plate. These events impact internal stresses within the Pacific plate, creating areas of weakness, above the Hawaii mantle plume, causing magma to be preferentially ejected to the surface at this point. Over time, these stresses change, causing the variations in azimuth observed in the segmentation of the Hawaii-Emperor Chain. This may also help to explain why over the Hawaiian swell, there appears to be only a single track (one volcano wide) of volcanoes opposed to the expected, more random distribution of volcanoes along this chain. The Emperor Seamount Chain is significantly better fitting to a great circle distribution in comparison to the Hawaii Seamount Chain, as previously mentioned. The stark change in closeness of fit to a great circle distribution between these seamount chains has been attributed to the tectonic changes which occurred leading to the formation of the Hawaii-Emperor Bend or the limitations of the statistical model utilised. Furthermore, it appears that

these controls over the segmentation of the Hawaii-Emperor Seamount Chain have no major controls over the morphologies of seamounts. It is believed that local stresses such as gravitational stresses created by the loading of volcanic edifices on oceanic lithosphere have a significantly greater impact on the formation of the seamounts.

There is no doubt lots of room for future work surrounding this hypothesis. There are large numbers of ocean island chains within the Pacific plate where controls surrounding the distribution of volcanism are fully understood, or very similar to the Hawaii-Emperor Seamount Chain. For example, the Louisville Seamount Chain, similar to Hawaii-Emperor, has a bend along its track which dates to a very similar time Gaastra et al., (2022) as the Hawaii-Emperor Bend. As well as this, the distributions of volcanoes along Puka-Puka and Crossgrain ridges are believed to be influenced by pre-existing features within the oceanic lithosphere (Lynch, (1999). In order to fully test this hypothesis, seamount chains within different domains must be tested using this method. As a result, it is proposed that in future, the Louisville and Puka-Puka Seamount Chains would benefit from being analysed utilising this method.

4.5 Limitations and Considerations:

Throughout this project there have been numerous variables which have had to be considered which have the potential to impact the outcomes of this project. Initially, the environment in which the area of study is within is extremely inhospitable, where the vast majority of the studied volcanoes are submerged within the Pacific Ocean. This problem is ultimately the leading cause of the largest limitation of this project, a lack of data. Whether it is bathymetric, geochemical, radiometric or core samples, there are large regimes within the Hawaii-Emperor Seamount Chain where there is poor quality data or no data at all due to the difficulty of gathering it or getting to it. Furthermore, as of 15th June 2006, the Papahānaumokuākea Marine National Monument had been established, one of the world's

largest protected areas, further restricting opportunities to gather data and sample along the Hawaii-Emperor Seamount Chain.

Due to these limitations, especially the creation of the Marine National Monument, data which is used for geochemical trends and radiometric ages are mostly reused from older studies of ocean island seamounts within the Hawaii-Emperor Seamount Chain. An issue with this is, due to this being older data, methods in calculating may not be as accurate as more modern methods. Even more simple problems, such as a greater proportion of K/Ar radiometric ages in comparison to Ar/Ar radiometric ages can cause problems as K/Ar dating is more sensitive to both clays and alteration within rocks.

Furthermore, another limitation to this project which needs to be considered is the use of the Akaike information criterion correction (AICc) for segments with low numbers of volcanoes in them. In order to see how well great circles fit a segment in comparison to small circle distributions without a bias resulting from adjustable parameters, the AICc has to be used. However, it has been noted that an AICc value for small circles cannot be produced for segments which have only four volcanoes along them. This is because, when trying to fit a small circle to a segment where $n = 4$, k has to be equal to 3 (the number of adjustable parameters for a small circle, its centre point location x and y coordinates and its radius). Looking at Eq. 4 in Chapter 2.2 it can easily be seen that for any segment where $n = 4$ and $k = 3$ it is not possible to calculate the AICc. As a result of this, there is not a way of comparing how well great circle distributions fit segments with small numbers of volcanoes to small circle distributions without bias for the adjustable parameters. In future attempts to constrain and compare great circle and small circle distributions of segments of volcanoes, the Bayesian Information Criterion (BIC) may be a different statistical model which could be used (Eqs 5,6 and 7) . The use of this statistic could potentially help to facilitate the comparison of smaller sample sizes of volcanoes along segments whilst also allowing for the comparison of larger numbers of volcanoes.

$$AICc = AIC + \frac{2k(k+1)}{n-k-1}$$

Eq. 5

$$BIC = n\ln\left(\widehat{\sigma_e^2}\right) + k\ln(n)$$

Eq. 6

Where:

$$\widehat{\sigma_e^2} = \frac{1}{n}\sum_{i=1}^{n}(x_i - \widehat{x_i})$$

Eq. 7

An advantage of using the BIC opposed to the AIC and AICc is that, whilst still being closely related to the AIC, the BIC is able to penalise against adjustable parameters more easily than the AIC Vrieze, (2012).

Chapter 5. Conclusion:

This project has built upon previous work utilising the Hough Transform and applied this technique in an attempt to order to recognise alignments of ocean island volcanoes in the Hawaii Seamount Chain. This project aimed to determine the best-fitting geometry of alignments identified along the Hawaii-Emperor Seamount Chain as well as providing a geodynamic model which best explains an orderly, segmented, and aligned Hawaii-Emperor Seamount Chain, with the scope to potentially provide a re-evaluation of mechanisms involved with the creation of ocean island volcanoes.

As previously mentioned, Natland and Winterer (2005) state that, the 'hypothesis of plates moving over fixed plumes is strongly dependant on the perceptions of alignment of volcanoes' along their chains. Although we propose a new outlook for the distributions and alignments of volcanoes along the Hawaii-Emperor Seamount Chain, this approach is strengthened by the quantitative means by which these alignments were identified, chosen and compared to one another, and the way in which other distributions of volcanoes were disregarded, in comparison to previous attempts to define alignments of volcanoes in the Hawaii-Emperor Seamount Chain, which were much more subjective Fiske and Jackson, (1972); Jackson et al., (1972, 1975); Jackson and Shaw, (1975).

Having completed spatial analysis and quantitative statistical analysis of models for both small circle and great circle distributions of volcanoes, the following conclusions have been drawn about this method and its results.

a) We have applied a spatial recognition method utilising the Hough Transform for the evaluation of different great and small circle distributions of ocean island volcanism. This method is repeatable and has produced results favouring segmentation at two different pacific seamount chains.
b) The best fitting geometry for volcanism in both the Hawaii and Emperor Seamount Chains (according to AICc statistical analysis) is described by a segmented great circle distribution, in comparison to both single and segmented small circle distributions.

c) For volcanoes which have formed within the Hawaii Seamount Chain after ~23 Ma the misfit (rms and AICc) for each segment demonstrates an even better correlation fit with great circles. Potential causes of this observation have been discussed and include the influence of the change in activity of a spreading centre on the West Pacific boundary.

d) The driving factor towards the segmentation of the Hawaii Emperor Seamount Chain is neo-tectonic events (tectonic events which are occurring contemporaneously with magmatism), where they affect internal stresses within the Pacific plate, focussing the distribution of volcanism into the observed segments.

e) 'Cross track' seamounts have been identified across both the Hawaiian and Emperor Seamount Chains and their formation is inferred to have been influenced by potential transform zones or weaknesses within the oceanic lithosphere which crosscut the general azimuth of the chains.

f) The Akaike Information Criterion Correction indicates that the closeness of fit for great circle segmentation in ocean island seamount chains favours the Emperor Seamount Chain more than the Hawaii Seamount Chain.

g) The Hawaii-Emperor Bend is potentially the one area where this method does not work at its best, however this is undoubtedly due to the highly complex geodynamic nature of this area.

h) Geodynamic processes which are thought to influence the formation of volcanoes towards great circle distributions are found to have minimal effect on the formation of volcanic edifices, where gravitational stresses are believed to be the driving control.

Bibliography:

Akaike, H., 1974, A new look at the statistical model identification: IEEE Transactions on Automatic Control, v. 19, p. 716–723, doi:10.1109/TAC.1974.1100705.

Anchieta, M.C., Wolfe, C.J., Pavlis, G.L., Vernon, F.L., Eakins, J.A., Solomon, S.C., Laske, G., and Collins, J.A., 2011, Seismicity around the Hawaiian Islands Recorded by the PLUME Seismometer Networks: Insight into Faulting near Maui, Molokai, and Oahu: Bulletin of the Seismological Society of America, v. 101, p. 1742–1758, doi:10.1785/0120100271.

Anderson, D.L., 2000, The thermal state of the upper mantle; No role for mantle plumes: Geophysical Research Letters, v. 27, p. 3623–3626, doi:10.1029/2000GL011533.

Andikagumi, H., Macpherson, C.G., and McCaffrey, K.J.W., 2020, Upper Plate Stress Controls the Distribution of Mariana Arc Volcanoes: Journal of Geophysical Research: Solid Earth, v. 125, doi:10.1029/2019JB017391.

Ballmer, M.D., Ito, G., Van Hunen, J., and Tackley, P.J., 2011, Spatial and temporal variability in Hawaiian hotspot volcanism induced by small-scale convection: Nature Geoscience, v. 4, p. 457–460, doi:10.1038/ngeo1187.

Brink, U. ten, 1991, Volcano spacing and plate rigidity: Geology, v. 19, p. 397, doi:10.1130/0091-7613(1991)019<0397:VSAPR>2.3.CO;2.

Burnham, K.P., and Anderson, D.R., 2004, Multimodel Inference: Understanding AIC and BIC in Model Selection: Sociological Methods & Research, v. 33, p. 261–304, doi:10.1177/0049124104268644.

Cebriá, J.M., Martín-Escorza, C., López-Ruiz, J., Morán-Zenteno, D.J., and Martiny, B.M., 2011, Numerical recognition of alignments in monogenetic volcanic areas: Examples from the Michoacán-Guanajuato Volcanic Field in Mexico and Calatrava in Spain: Journal of Volcanology and Geothermal Research, v. 201, p. 73–82, doi:10.1016/j.jvolgeores.2010.07.016.

Chaytor, J.D., Keller, R.A., Duncan, R.A., and Dziak, R.P., 2007, Seamount morphology in the Bowie and Cobb hot spot trails, Gulf of Alaska: Geochemistry, Geophysics, Geosystems, v. 8, p. n/a-n/a, doi:10.1029/2007GC001712.

Cheng, Q., Park, K.-H., Macdougall, J.D., Zindler, A., Lugmair, G.W., Staudigel, H., Hawkins, J., and Lonsdale, P., 2013, Isotopic Evidence for a Hotspot Origin of the Louisville Seamount Chain, *in* p. 283–296, doi:10.1029/GM043p0283.

Clague, D.A., Dalrymple, G.B., Wright, T.L., Klein, F.W., Koyanagi, R.Y., Decker, R.W., and Thomas, D.M., 1989, The Hawaiian-Emperor Chain, *in* The Eastern Pacific Ocean and Hawaii, North America, Geological Society of America, p. 187–287, doi:10.1130/DNAG-GNA-N.187.

Clouard, V., and Bonneville, A., 2001, How many Pacific hotspots are fed by deep-mantle plumes? Geology, v. 29, p. 695, doi:10.1130/0091-7613(2001)029<0695:HMPHAF>2.0.CO;2.

Coffin M, and Edholm O, 1993, Scratching the surface Estimating dimensions of large igneous provinces: GEOLOGY, v. 21, p. 515–518.

Courtillot, V., Davaille, A., Besse, J., and Stock, J., 2003, Three distinct types of hotspots in the Earth's mantle: Earth and Planetary Science Letters, v. 205, p. 295–308, doi:10.1016/S0012-821X(02)01048-8.

Davies, D.R., Rawlinson, N., Iaffaldano, G., and Campbell, I.H., 2015, Lithospheric controls on magma composition along Earth's longest continental hotspot track: Nature, v. 525, p. 511–514, doi:10.1038/nature14903.

Deschamps, A., and Lallemand, S., 2002, The West Philippine Basin: An Eocene to early Oligocene back arc basin opened between two opposed subduction zones: Journal of Geophysical Research: Solid Earth, v. 107, doi:10.1029/2001JB001706.

Dieterich, J.H., 1988, Growth and persistence of Hawaiian volcanic rift zones: Journal of Geophysical Research: Solid Earth, v. 93, p. 4258–4270, doi:10.1029/JB093iB05p04258.

Duda, R.O., and Hart, P.E., 1972a, Use of the Hough transformation to detect lines and curves in pictures: Communications of the ACM, v. 15, p. 11–15, doi:10.1145/361237.361242.

Duda, R.O., and Hart, P.E., 1972b, Use of the Hough transformation to detect lines and curves in pictures: Communications of the ACM, v. 15, p. 11–15, doi:10.1145/361237.361242.

Fiske R, and Jackson E, 1972, Orientation and growth of Hawaiian volcanic rifts: the effect of regional structure and gravitational stresses:, https://royalsocietypublishing.org/.

Frey, F.A., Huang, S., Xu, G., and Jochum, K.P., 2016, The geochemical components that distinguish Loa- and Kea-trend Hawaiian shield lavas: Geochimica et Cosmochimica Acta, v. 185, p. 160–181, doi:10.1016/j.gca.2016.04.010.

Gaastra, K.M., Gordon, R.G., and Woodworth, D.T., 2022, Quantification of Pacific Plate Hotspot Tracks Since 80 Ma: Tectonics, v. 41, doi:10.1029/2021TC006772.

Le Gall, B., Gernigon, L., Rolet, J., Ebinger, C., Gloaguen, R., Nilsen, O., Dypvik, H., Deffontaines, B., and Mruma, A., 2004, Neogene-Holocene rift propagation in central Tanzania: Morphostructural and aeromagnetic evidence from the Kilombero area: Geological Society of America Bulletin, v. 116, p. 490, doi:10.1130/B25202.1.

Griffiths, R.W., and Campbell, I.H., 1990, Stirring and structure in mantle starting plumes: Earth and Planetary Science Letters, v. 99, p. 66–78, doi:10.1016/0012-821X(90)90071-5.

Hall, R., 2002, Cenozoic geological and plate tectonic evolution of SE Asia and the SW Pacific: computer-based reconstructions, model and animations: Journal of Asian Earth Sciences, v. 20, p. 353–431, doi:10.1016/S1367-9120(01)00069-4.

Hall, R., 1997, Cenozoic plate tectonic reconstructions of SE Asia: Geological Society, London, Special Publications, v. 126, p. 11–23, doi:10.1144/GSL.SP.1997.126.01.03.

Harrison, L.N., Weis, D., and Garcia, M.O., 2017, The link between Hawaiian mantle plume composition, magmatic flux, and deep mantle geodynamics: Earth and Planetary Science Letters, v. 463, p. 298–309, doi:10.1016/j.epsl.2017.01.027.

Hieronymus, C.F., and Bercovici, D., 2001, A theoretical model of hotspot volcanism: Control on volcanic spacing and patterns via magma dynamics and lithospheric stresses: Journal of Geophysical Research: Solid Earth, v. 106, p. 683–702, doi:10.1029/2000JB900355.

Hieronymus, C.F., and Bercovici, D., 1999, Discrete alternating hotspot islands formed by interaction of magma transport and lithospheric flexure: Nature, v. 397, p. 604–607, doi:10.1038/17584.

Hieronymus, C.F., and Bercovici, D., 2000, Non-hotspot formation of volcanic chains: control of tectonic and flexural stresses on magma transport: Earth and Planetary Science Letters, v. 181, p. 539–554, doi:10.1016/S0012-821X(00)00227-2.

Holm, R.J., Rosenbaum, G., and Richards, S.W., 2016, Post 8 Ma reconstruction of Papua New Guinea and Solomon Islands: Microplate tectonics in a convergent plate boundary setting: Earth-Science Reviews, v. 156, p. 66–81, doi:10.1016/j.earscirev.2016.03.005.

Jackson, E.D., and Shaw, H.R., 1975, Stress fields in central portions of the Pacific Plate: Delineated in time by linear volcanic chains: Journal of Geophysical Research, v. 80, p. 1861–1874, doi:10.1029/JB080i014p01861.

Jackson, E.D., Shaw, H.R., and Bargar, K.E., 1975, Calculated geochronology and stress field orientations along the Hawaiian chain: Earth and Planetary Science Letters, v. 26, p. 145–155, doi:10.1016/0012-821X(75)90082-5.

Jackson, E., Silver, E., and Dalrymple, B., 1972, Hawaiian-Emperor Chain and its relation to Cenozoic circumpacific tectonics: GSA Bulletin, v. 83, p. 601–618.

Jicha, B.R., Garcia, M.O., and Wessel, P., 2018, Mid-Cenozoic Pacific plate motion change: Implications for the Northwest Hawaiian Ridge and circum-Pacific: Geology, v. 46, p. 939–942, doi:10.1130/G45175.1.

Keller, R.A., Fisk, M.R., and White, W.M., 2000, Isotopic evidence for Late Cretaceous plume–ridge interaction at the Hawaiian hotspot: Nature, v. 405, p. 673–676, doi:10.1038/35015057.

Kelley, C. et al., 2015, New Insights from Seafloor Mapping of a Hawaiian Marine Monument: Eos, v. 96, doi:10.1029/2015EO030235.

Koppers, A.A.P., Becker, T.W., Jackson, M.G., Konrad, K., Müller, R.D., Romanowicz, B., Steinberger, B., and Whittaker, J.M., 2021, Mantle plumes and their role in Earth processes: Nature Reviews Earth & Environment, v. 2, p. 382–401, doi:10.1038/s43017-021-00168-6.

Liu, Y. et al., 2023, Origin of microplates under oblique subduction system in New Guinea: Inferences from gravity and magnetic data: Gondwana Research, v. 120, p. 175–189, doi:10.1016/j.gr.2022.09.001.

Liu, S., Gurnis, M., Ma, P., and Zhang, B., 2017, Reconstruction of northeast Asian deformation integrated with western Pacific plate subduction since 200 Ma: Earth-Science Reviews, v. 175, p. 114–142, doi:10.1016/j.earscirev.2017.10.012.

Lonsdale, P., 1988, Geography and history of the Louisville Hotspot Chain in the southwest Pacific: Journal of Geophysical Research, v. 93, p. 3078, doi:10.1029/JB093iB04p03078.

Lynch, M.A., 1999, Linear ridge groups: Evidence for tensional cracking in the Pacific Plate: Journal of Geophysical Research: Solid Earth, v. 104, p. 29321–29333, doi:10.1029/1999JB900241.

MacDonald, G.A., 1955, Hawaiian Volcanoes during 1952: U.S. Geological Survey Bulletin, v. 1021, p. 15–108.

Mahony, S.H., Wallace, L.M., Miyoshi, M., Villamor, P., Sparks, R.S.J., and Hasenaka, T., 2011, Volcano-tectonic interactions during rapid plate-boundary evolution in the Kyushu region, SW Japan: Geological Society of America Bulletin, v. 123, p. 2201–2223, doi:10.1130/B30408.1.

Meschede, M., and Barckhausen, U., 2000, Plate tectonic evolution of the Cocos-Nazca spreading center, doi:10.2973/odp.proc.sr.170.009.2000.

Michon, L., Saint-Ange, F., Bachelery, P., Villeneuve, N., and Staudacher, T., 2007, Role of the structural inheritance of the oceanic lithosphere in the magmato-tectonic evolution of Piton de la Fournaise volcano (La Réunion Island): Journal of Geophysical Research: Solid Earth, v. 112, doi:10.1029/2006JB004598.

Miller, M.S., and Kennett, B.L.N., 2006, Evolution of mantle structure beneath the northwest Pacific: Evidence from seismic tomography and paleogeographic reconstructions: Tectonics, v. 25, doi:10.1029/2005TC001909.

Morgan, W.J., 1972, Plate Motions and Deep Mantle Convection, *in* p. 7–22, doi:10.1130/MEM132-p7.

Morgan W, 1971, Convection Plumes in the Lower Mantle: Academic Press.

Morgan W, 1972, Deep Mantle Convection Plumes and Plate Motions: The American Association of Petroleum Geologists Bulletin, v. 56, p. 203–213.

Nakamura, K., 1982, Why do long rift zones develop better in Hawaiian volcanoes - a possible role of thick oceanic sediments: Arquipélago. Série Ciências da Natureza, p. 59–73.

Nakanishi, M., Sager, W.W., and Klaus, A., 1999, Magnetic lineations within Shatsky Rise, northwest Pacific Ocean: Implications for hot spot-triple junction interaction and oceanic plateau formation: Journal of Geophysical Research: Solid Earth, v. 104, p. 7539–7556, doi:10.1029/1999JB900002.

Nakanishi, M., Tamaki, K., and Kobayashi, K., 1992a, A new Mesozoic isochron chart of the northwestern Pacific Ocean: Paleomagnetic and tectonic implications: Geophysical Research Letters, v. 19, p. 693–696, doi:10.1029/92GL00022.

Nakanishi, M., Tamaki, K., and Kobayashi, K., 1992b, Magnetic anomaly lineations from Late Jurassic to Early Cretaceous in the west-central Pacific Ocean: Geophysical Journal International, v. 109, p. 701–719, doi:10.1111/j.1365-246X.1992.tb00126.x.

Natland, J.H., and Winterer, E.L., 2005, Fissure control on volcanic action in the Pacific, *in* Plates, plumes and paradigms, Geological Society of America, doi:10.1130/0-8137-2388-4.687.

Niu, Y., 2021, Lithosphere thickness controls the extent of mantle melting, depth of melt extraction and basalt compositions in all tectonic settings on Earth – A review and new perspectives: Earth-Science Reviews, v. 217, p. 103614, doi:10.1016/j.earscirev.2021.103614.

Olson, P., and Christensen, U., 1986, Solitary wave propagation in a fluid conduit within a viscous matrix: Journal of Geophysical Research, v. 91, p. 6367, doi:10.1029/jb091ib06p06367.

Olson, P., and Singer, H., 1985, Creeping plumes: Journal of Fluid Mechanics, v. 158, p. 511–531, doi:10.1017/S0022112085002749.

Olson, P., and Yuen, D.A., 1982, Thermochemical plumes and mantle phase transitions: Journal of Geophysical Research, v. 87, p. 3993, doi:10.1029/JB087iB05p03993.

Pacey, A., Macpherson, C.G., and McCaffrey, K.J.W., 2013, Linear volcanic segments in the central Sunda Arc, Indonesia, identified using Hough Transform analysis: Implications for arc

lithosphere control upon volcano distribution: Earth and Planetary Science Letters, v. 369–370, p. 24–33, doi:10.1016/j.epsl.2013.02.040.

Peive, A.A., 2007, Linear volcanic chains in oceans: Possible formation mechanisms: Geotectonics, v. 41, p. 281–295, doi:10.1134/S0016852107040024.

Perez-Torrado, F.J., Carracedo, J.C., Guillou, H., Rodriguez-Gonzalez, A., and Fernandez-Turiel, J.L., 2023, Age, duration, and spatial distribution of ocean shields and rejuvenated volcanism: Fuerteventura and Lanzarote, Eastern Canaries: Journal of the Geological Society, doi:10.1144/jgs2022-112.

Regelous, M., Hofmann, A.W., Abouchami, W., and Galer, S.J.G., 2003, Geochemistry of Lavas from the Emperor Seamounts, and the Geochemical Evolution of Hawaiian Magmatism from 85 to 42 Ma: Journal of Petrology, v. 44, p. 113–140, doi:10.1093/petrology/44.1.113.

Richards, F.D., Kalnins, L.M., Watts, A.B., Cohen, B.E., and Beaman, R.J., 2018, The Morphology of the Tasmantid Seamounts: Interactions Between Tectonic Inheritance and Magmatic Evolution: Geochemistry, Geophysics, Geosystems, v. 19, p. 3870–3891, doi:10.1029/2018GC007821.

Richards M, Duncan R, and Courtillot V, 1989, Flood Basalts and Hot-Spot Tracks Plume Heads and Tails: Science, p. 103–107.

Rose, J., and Koppers, A.A.P., 2019, Simplifying Age Progressions within the Cook-Austral Islands using ARGUS-VI High-Resolution ^{40} Ar/ ^{39} Ar Incremental Heating Ages: Geochemistry, Geophysics, Geosystems, v. 20, p. 4756–4778, doi:10.1029/2019GC008302.

Sasaki, T., Yamazaki, T., and Ishizuka, O., 2014, A revised spreading model of the West Philippine Basin: Earth, Planets and Space, v. 66, p. 83, doi:10.1186/1880-5981-66-83.

Schubert, G., Olson, P., Anderson, C., and Goldman, P., 1989, Solitary waves in mantle plumes: Journal of Geophysical Research, v. 94, p. 9523, doi:10.1029/JB094iB07p09523.

Scott, G.A.J., and Rotondo, G.M., 1983, A model to explain the differences between Pacific plate island-atoll types: Coral Reefs, v. 1, p. 139–150, doi:10.1007/BF00571191.

Steinberger, B., 2000, Plumes in a convecting mantle: Models and observations for individual hotspots: Journal of Geophysical Research: Solid Earth, v. 105, p. 11127–11152, doi:10.1029/1999JB900398.

Tatsumoto, M., 1978, Isotopic composition of lead in oceanic basalt and its implication to mantle evolution: Earth and Planetary Science Letters, v. 38, p. 63–87, doi:10.1016/0012-821X(78)90126-7.

Turcotte, D.L., and Oxburgh, E.R., 1973, Mid-plate Tectonics: Nature, v. 244, p. 337–339, doi:10.1038/244337a0.

Utkin, V.P., 2006, Role of strike-slip faulting of the oceanic lithosphere in the formation of pacific volcanic belts: Doklady Earth Sciences, v. 409, p. 692–696, doi:10.1134/S1028334X06050023.

Vidal, V., and Bonneville, A., 2004, Variations of the Hawaiian hot spot activity revealed by variations in the magma production rate: Journal of Geophysical Research, v. 109, p. B03104, doi:10.1029/2003JB002559.

Vogt, P.R., 1974, Volcano spacing, fractures, and thickness of the lithosphere: Earth and Planetary Science Letters, v. 21, p. 235–252, doi:10.1016/0012-821X(74)90159-9.

Von Veh, M.W., and Németh, K., 2009, An assessment of the alignments of vents based on geostatistical analysis in the Auckland Volcanic Field, New Zealand: Géomorphologie : relief, processus, environnement, v. 15, p. 175–186, doi:10.4000/geomorphologie.7664.

Vrieze, S.I., 2012, Model selection and psychological theory: A discussion of the differences between the Akaike information criterion (AIC) and the Bayesian information criterion (BIC).: Psychological Methods, v. 17, p. 228–243, doi:10.1037/a0027127.

Wadge, G., and Cross, A., 1988, Quantitative methods for detecting aligned points: An application to the volcanic vents of the Michoacan-Guanajuato volcanic field, Mexico: Geology, v. 16, p. 815, doi:10.1130/0091-7613(1988)016<0815:QMFDAP>2.3.CO;2.

Walker, G.P.L., 1999, Volcanic rift zones and their intrusion swarms: Journal of Volcanology and Geothermal Research, v. 94, p. 21–34, doi:10.1016/S0377-0273(99)00096-7.

Weis, D., Garcia, M.O., Rhodes, J.M., Jellinek, M., and Scoates, J.S., 2011, Role of the deep mantle in generating the compositional asymmetry of the Hawaiian mantle plume: Nature Geoscience, v. 4, p. 831–838, doi:10.1038/ngeo1328.

White, R.S., 1993, Melt production rates in mantle plumes:, https://royalsocietypublishing.org/.

Whitehead, J.A., 1982, Instabilities of fluid conduits in a flowing earth — are plates lubricated by the asthenosphere?, https://academic.oup.com/gji/article/70/2/415/558450.

Whitman, J.M., Harrison, C.G.A., and Brass, G.W., 1983, Tectonic evolution of the Pacific Ocean since 74 ma: Tectonophysics, v. 99, p. 241–249, doi:10.1016/0040-1951(83)90106-3.

Wilson, J.T., 1963, A POSSIBLE ORIGIN OF THE HAWAIIAN ISLANDS: Canadian Journal of Physics, v. 41, p. 863–870, doi:10.1139/p63-094.

Winterer, E.L., and Sandwell, D.T., 1987, Evidence from en-echelon cross-grain ridges for tensional cracks in the Pacific plate: Nature, v. 329, p. 534–537, doi:10.1038/329534a0.

Wu, J., Suppe, J., Lu, R., and Kanda, R., 2016, Philippine Sea and East Asian plate tectonics since 52 Ma constrained by new subducted slab reconstruction methods: Journal of Geophysical Research: Solid Earth, v. 121, p. 4670–4741, doi:10.1002/2016JB012923.

Appendix:

Appendix A: Volcanic centres database

Seamount Name	Longitude	Latitude	Age (Ma)	Error (Ma)	Method	Citation
Loihi / Kamaʻehuakanaloa	-155.2531552	18.9152653	0	\	observation	Observation
Kilauaea	-155.280901	19.4140917	0	\	observation	Observation
Mauna Loa	-155.5910276	19.47026	0.54			Evernden et al (1964)
Hualalai	-155.868498	19.6911279	0.4	0.3		Funkhouser et al (1968)
Mauna Kea	-155.469583	19.820247	0.375	0.05	K/Ar	Porter et al (1977)
Kohala	-155.716923	20.085498	0.4	0.02	K/Ar	McDougall and Swanson (1972)
Mahukona	-156.4196061	20.1565929	0.65	0.036		Garcia et al (2012)
Haleakala	-156.2504541	20.7088972	0.86	0.03	K/Ar	McDougall (1964)
West Maui	-156.5896457	20.8925311	1.32	0.04	K/Ar	McDougall (1964)
Kaho'olawe	-156.56878	20.559999	1.03	0.18	K/Ar	Naughton et al (1980)

Lana'i	-156.8752313	20.817232	1.28	0.04	K/Ar	Bonhommet et al (1977)
East Molokai	-156.850654	21.133918	1.52	0.05		McDougall (1964)
West Molokai	-157.165939	21.1362415	1.89	0.06		McDougall (1964)
Penguin Bank	-157.5476689	21.0527287	1.5			Xu et al (2014)
Ko'olau	-157.7400595	21.3904824	2.6	0.1		McDougall (1964)
Wai'anae	-158.1432673	21.4484615	3.71	0.1		Doell and Dalrymple (1973)
Ka'ena	-158.5374799	21.7039129	5			Sinton et al (2014)
Kaua'i	-159.5003171	22.0855944	5.14	0.2	K/Ar	McDougall (1964)
Ni'ihau	-160.0887874	21.9126449	4.89	0.11		Clague and Dalrymple (1987)
Ka'ula	-160.5413293	21.6512867	4	0.2		Garcia et al (1986) - origin of Hawaiian Phonolites
Middle Bank	-161.049922	22.7071623	5.95	0.08		Jicha, Garcia, and Wessel (2018)
Nihoa	-161.9252245	23.0620755	7.2	0.3	K/Ar	Dalrymple et al (1974)

West Nihoa	-162.2880118	22.9797773	8.19	0.03		Jicha, Garcia, and Wessel (2018)
East Twin Banks	-162.6137505	23.2529034	9.01	0.07		Jicha, Garcia, and Wessel (2018)
Twin Banks	-162.9185746	23.2448838	9.2	0.07		Garcia et al (1986)
West Twin Banks	-163.1478405	23.1944955	9.6	1.6		Garcia et al (1987)
Keoea	-163.5725398	23.2905576	-	-	-	
SE Necker	-164.4072642	23.3741451	-	-	-	
Necker / Mokumanamana	-164.7099275	23.5724918	10.3	0.4	K/Ar	Dalrymple et al (1974)
Kanehunamoku	-166.0159832	24.2934842	13.4	0.04		Jicha, Garcia, and Wessel (2018)
French Frigate Shoals	-166.2694425	23.7345367	12	0.4		Dalrymple et al (1974)
Brooks Bank (1)	-166.6982694	23.9784622	13	1.2		Garcia et al (1986)
Brooks Bank (2)	-166.821017	24.1037227	-	-	-	
Brooks Bank (3)	-166.9613143	24.1979179	-	-	-	

St Rogatien Bank	-167.1753933	24.341303	-	-	-	
unnamed	-167.2918415	24.5919463	-	-	-	
Gardner Pinnacles	-168.0087244	24.9883974	14.11	0.16	-	Jicha, Garcia, and Wessel (2018)
Raita Bank	-169.5714663	25.4475911	18.05	0.05		Jicha, Garcia, and Wessel (2018)
unnamed	-169.6529079	24.8448613	-	-	-	
Maro Reef / Nalukakala	-170.6607148	25.4907643	-	-	-	
Laysan Island / Kauo	-171.7331573	25.780867	19.9	0.3	K/Ar	Dalrymple et al (1981)
East Northampton	-172.0604511	25.3940513	23.11	0.23		Jicha, Garcia, and Wessel (2018)
West Northampton	-172.4087583	25.5089021	-	-	-	
unnamed	-172.9259013	25.6482645	-	-	-	
Pioneer Tablemount	-173.436707	25.9738916	-	-	-	

Lisianski Island / Papa'apoho	-173.9708866	26.070721	-	-	-	
unnamed	-174.5288257	26.2905223	-	-	-	
unnamed	-175.5835708	27.7138758	-	-	-	
Bank 9	-175.6038208	27.020902	-	-	-	
Pearl and Hermes / Holoikauaua	-175.8557853	27.8439291	24.9	0.3		O'Connor and Steinberger et al (2013)
Ladd Seamount	-176.6654879	28.5346856	0			
Midway	-177.3863004	28.2413208	27	0.6		Dalrymple et al (1977)
Nero Seamount	-177.9734006	27.9676621	-	-	-	
Kure Atoll	-178.3217118	28.4336663	29			Carson et al (1995)
Turnif	-178.6247564	28.9023538	29.3	0.5		O'Connor and Steinberger et al (2013)

Academician Berg	-178.8597661	28.8435274	31			Clague et al (1975)
unnamed	-179.1313792	28.8277608	-	-	-	
Helsley	-179.5637696	28.9095046	31.9	0.7		O'Connor and Steinberger et al (2013)
unnamed	179.3170811	29.6884119	-	-	-	
Townstead and Cromwell	179.0694708	29.7939811	26.7	0.5	K/Ar	Clague et al (1975)
Hancock	178.7106402	30.2688116	0			
De Veuster	177.547509	30.3640279	0			
Colahan	175.8994736	31.0260913	39.1	0.2	Ar/Ar	Sharp and Clague (2006)
unnamed	175.6843446	30.921368	0			
Abbott	174.2928737	31.7967286	41.7	0.7	Ar/Ar	O'Connor et al 2013
East Kammu	173.1291965	32.0064768	43.6			O'Connor and Steinberger et al (2013)
West Kammu	172.8533817	32.271042	44.3	0.7	Ar/Ar	O'Connor and Steinberger et al (2013)
Daikakuji	172.2787296	32.0822666	47.7	0.5	Ar/Ar	O'Connor et al 2013

Yuryaku	172.2612937	32.6833318	47.8	0.7	Ar/Ar	Oconnor et al 2013
Goshirakawa	171.596301	32.6299102	-	-	-	
Gosanjo	171.5945425	32.8813749	-	-	-	
Toba	171.6413184	33.258396	-	-	-	
Genji	172.2341412	33.3236943	-	-	-	
Kinmei	171.3393129	33.7628719	48.2	0.2	Ar/Ar	Sharp and Clague (2006)
Taisho	171.9128752	33.7303444	-	-	-	
Lower Koko	171.651582	33.7008999	50.4			Sharp and Clague (2006)
unnamed	171.3870402	34.2621021	-	-	-	
Koko	171.8936605	34.9593829	49.59	2.42	Ar/Ar	Koopers et al (2019)
N Koko	171.4102402	35.3626995	52.9	0.8	Ar/Ar	Sharp and Clague (2006)
unnamed	171.7023272	36.3445914	-	-	-	
unnamed	171.3614841	36.7919808	-	-	-	
unnamed	171.2000136	37.665108	-	-	-	
Oijin	170.3482265	38.0530165	55.2	0.7	K/Ar	Dalrymple et al (1980) conventional and AR/AR ages

Jingu	171.1083242	38.6685478	55.4	0.9	K/Ar	Dalrymple and Garcia (1980)
Nintoku	170.581753	41.1278012	56.41	0.6	K/Ar	Dalrymple et al (1980) conventional and AR/AR ages
Ninigi	170.2097844	41.7354788	-	-	-	
Godaigo	170.5791045	41.8602777	-	-	-	
Yomei	170.4817694	42.2411671	-	-	-	
Showa	170.4211392	43.0513324	-	-	-	
Saga	169.9977584	43.409639	-	-	-	
S-Suiko	170.222013	44.5580191	59.6	0.6		Saito and Ozima (1975&1977)
N-Suiko	170.1413796	45.2622036	61.3	0.3	Ar/Ar	Sharp and Clague (2006)
unnamed	169.1100056	45.8288377	-	-	-	
Jimmu	169.532653	46.1274126	-	-	-	
unnamed	169.2867071	47.4235246	-	-	-	
unnamed	169.061896	47.6729725	-	-	-	

unnamed	168.953194	48.0818896	-	-	-	
unnamed	169.4534483	48.2525257	-	-	-	
Minnetonka	168.4114756	48.1533831	-	-	-	
Winnebago	167.6751101	48.6399081	-	-	-	
Tenji	168.3887706	48.9756917	-	-	-	
unnamed	169.3834346	49.1612763	-	-	-	
Suizei	168.2044737	49.628833	-	-	-	
Hanzei	167.6389461	50.1184847	-	-	-	
Detroit	167.4040522	50.5931157	77.79	1.4	Ar/Ar	Duncan and keller (2004)

Table showing locations, radiometric ages with their errors and the method by which this radiometric age was gathered.

GET BIBLIOGRAPHY FOR APPENDIX A

Appendix B: Geometric fitting

Appendix B.1: Hough Transform code.

The code utilised for the application of the Hough Transform spatial analysis, from Andikagumi et al 2020, modified in order to discriminate against large RMS misfitting segments which have been identified.

```
clc;
close all
close all hidden

% input
[ num , txt ] = xlsread('Seamount_Database_1.xlsx') ; % Dataset Name
lon = num (63:83 ,1) ;
lat = num (63:83 ,2) ;
names = txt (63:83);

ts = 180; % theta steps DEFAULT = 180
rs = 200; % rho steps DEFAULT = 200
nv = 4; % number of volcanoes in a line DEFAULT = 5
%MAXDISTANCE = 200; % maximum distance between two volcanoes
```

```
A = num2str(180/ts);
result01 = ['Theta increment: ', A , ' degree(s) '];

B=num2str(nv);
result02 = ['Minimum volcanoes each line : ', B ];
disp ( result01 ) ; disp ( result02 ) ; fprintf ('\n') ;

% conversion
lonr = lon .* (pi /180) ;
latr = lat .* (pi /180) ;


%% GNOMONIC PROJECTION

lonc = (max ( lonr ) +min ( lonr ) ) /2; latc = (max ( latr ) +min ( latr ) ) /2; %centre
properties

sinxc = sin( lonc ) ; sinyc = sin( latc ) ;
cosxc = cos( lonc ) ; cosyc = cos( latc ) ;

for i = 1: numel ( lonr ) % gnomonic calculation

    cosc ( i ) = sinyc * sin ( latr ( i ) ) + cosyc * cos ( latr ( i ) ) * cos (lonr ( i ) - lonc ) ;
    k ( i ) = 1/ cosc ( i ) ;
```

```
    long ( i ) = 1 * k ( i ) * cos ( latr ( i ) ) * sin ( lonr ( i ) - lonc ) ;
    latg ( i ) = 1 * k ( i ) * ( cosyc * sin ( latr ( i ) ) - sinyc * cos ( latr ( i ) ) * cos( lonr ( i )
- lonc ) ) ;

end

figure (1) ;
hold on ;
plot ( long , latg ,'^r','MarkerFaceColor','red') ;
pbaspect ([1 1 1]) ; grid on ; grid minor ; axis equal ;
C = min( long ) -0.02;
D = max( long ) +0.02;
xlim([C D]);
E = min( latg ) -0.02;
F = max( latg ) +0.02;
ylim([E F]) ;
title ('Hough Transform Line Detection ') ;
xlabel ('Longitude ') ; ylabel ('Latitude ') ;
%set(gca, 'YDir','reverse')
text ( long,latg,names,'VerticalAlignment','bottom','HorizontalAlignment','left')

%% HOUGH TRANSFORM

mintheta = 0;
maxtheta = 180;
```

```
for i = 1: numel ( long ) % max rho
    maxd ( i ) = sqrt ( long ( i ) ^2 + latg ( i ) ^2) ;
end

maxrho = max ( maxd ) ;

thetad = linspace (0 ,1 , ts +1) * maxtheta ;
thetar = linspace (0 ,1 , ts +1) *( pi) ;
rho = linspace ( -1 ,1 , rs +1) * maxrho ;

hough = zeros ( rs +1 , ts +1) ;
houghvol = zeros ( rs +1 , ts +1 , numel ( long ) ) ;

for i = 1: numel ( long ) %rho and theta calculation
    for j = 1: numel ( thetar )

        rho2 = long ( i ) *cos ( thetar ( j ) ) + latg ( i ) *sin ( thetar ( j ) ) ;
        rhoel = ( rs /2+1) + round (( rho2 ) /(2* maxrho /( rs +1) ) ) ;
        hough ( rhoel , j ) = hough ( rhoel , j ) + 1; % Hough matrix
        houghvol ( rhoel ,j , i ) = houghvol ( rhoel ,j , i ) + 1;
    end
end

figure (2) % plot Hough Matrix
```

```
imagesc ( thetad , rho , hough ) ; c = colorbar ;
xlabel ('\theta ( degree )') ; ylabel ('\rho') ;
title ('Hough Transform Lines on \rho and \theta system') ;
c.Label.String = 'Number of Volcanoes ';

httop = hough >= nv ; % matrix that has more than nv points

n = 1; % theta and rho matrix index

for i = 1 : ts +1 % extracting top theta and rho in real scale
   for j = 1 : rs +1
      if httop (j , i ) == 1
         toptheta ( n ) = i * (( pi) /( ts +1) ) ;
         toprho ( n ) = ( j * ( maxrho *2/( rs +1) ) ) - maxrho ;
         for k = 1 : numel ( long )
            topvol (n , k ) = houghvol (j ,i , k ) ;
         end
         n = n + 1;
      end
   end
end

f = waitbar (0 ,  'Processing ... ','Name','Small Circle Annealing Simulation ') ;
```

```
%tab1 = cell(numel(toptheta),numel(lon)); %create a table to store names of volcs in
all segments

for i = 1 : numel ( toptheta ) % plotting and calculating lines with > nv points
    m = 1;

    for k = 1 : numel ( long )
        if topvol (i , k ) == 1
            lonv ( m ) = long ( k ) ;
            latv ( m ) = latg ( k ) ;
            namev ( m ) = names ( k ) ;
            lonht ( m ) = lonr ( k ) ;
            latht ( m ) = latr ( k ) ;
            m = m +1;
        end
    end


    for j = 1 : numel ( lonv )
        if lonv ( j ) == min ( lonv )
            lonp (1) = lonv ( j ) ;
            latp (1) = latv ( j ) ;
            lonpr (1) = lonht ( j ) ;
            latpr (1) = latht ( j ) ;
        elseif lonv ( j ) == max ( lonv )
```

```
            lonp (2) = lonv ( j ) ;
            latp (2) = latv ( j ) ;
            lonpr (2) = lonht ( j ) ;
            latpr (2) = latht ( j ) ;
        end


        for count = 1 : numel ( lonht ) - 1  % using calcdist function to calculate distance between volcs

            [DISTRAD , DISTKM] = calcdist (lonht( count ), latht ( count ), lonht ( count + 1), latht (count + 1));

            DIST(count) = DISTKM;


        end

    end

    [ distradAB , distkmAB ] = calcdist ( lonpr (1) , latpr (1) , lonpr (2) , latpr (2) ) ;
    [ azradAB , azdegAB ] = calcaz ( lonpr (1) , latpr (1) , lonpr (2) , latpr (2) ) ;


    sumxtd2 = 0;
```

```
    for l = 1 : numel ( lonht )
        [ distradAD( l ) , distkmAD( l ) ] = calcdist ( lonpr (1) , latpr (1) , lonht ( l ) , latht (
l ) ) ;
        [ azradAD( l ) , azdegAB( l ) ] = calcaz ( lonpr (1) , latpr (1) , lonht ( l ) , latht ( l )
) ;
        [ xtdrad( l ) , xtdkm(l)  ] = calcxtd ( distradAD ( l ) , azradAB , azradAD ( l ) ) ;

        sumxtd2 = sumxtd2 + xtdkm ( l ) * xtdkm ( l ) ;
    end

    sumxtd = sqrt ( sumxtd2 / numel ( xtdkm ) ) ;

    G = num2str ( i );
    result1 = ['Line ', G ];
    H = num2str (toprho ( i ) );
    I = num2str (toptheta ( i ) * ( 180/pi ) );
    result2 = ['phi = ', H , ' ; theta = ', I ];
    J = num2str ( numel ( lonht ) );
    result3 = ['Number of volcanoes included : ', J ];
    result4 = namev;
    K = num2str (sumxtd);
    result5 = ['RMS Misfit = ', K , ' km '];
```

```
    disp ( result1 ) ; disp ( result2 ) ; disp ( result3 ) ; disp ( result4 ) ; disp ( result5 ) ;
fprintf ('\n') ;

    waitbar ( i / numel ( toptheta ) ,f ) ;

    maxi = 0;

    if numel (namev) > maxi

        maxi = numel(namev);

    end

    RMS(i,:) = sumxtd;

  % if DIST < MAXDISTANCE;

      if sumxtd < 20  % outputting best RMS lines

          figure (1)
          hold on
          plot ( lonp , latp ,'LineWidth' ,1) ;
  % else

      %disp('distance between volcanoes too long');
```

```
    end
  %end


end
```

```
function [ distrad , distkm ] = calcdist ( XA , YA , XB , YB ) % Calculate Distance
Function

s1 = ( sin (( YA - YB ) /2) ) ^2;
s2 = cos( YA ) * cos ( YB ) *( sin (( XA - XB ) /2) ) ^2;
distrad = 2* asin ( sqrt ( s1 + s2 ) ) ;
distkm = distrad *(180.0*60.0/ pi) *1.852;

function [ azrad , azdeg ] = calcaz ( XA , YA , XB , YB ) % Calculate Course Function

azrad = mod ( atan2 (sin( XA - XB ) *cos( YB ) ,cos( YA ) *sin( YB ) -sin( YA ) *cos(
YB ) *cos( YA - YB ) ) ,2* pi) ;
azdeg = 360 -( azrad *(180/ pi) ) ;
```

```
function [ xtdrad , xtdkm ] = calcxtd ( distradAD , azradAB , azradAD ) % Calculate
Cross Track Distance Function

xtdrad = asin (sin ( distradAD ) *sin ( azradAD - azradAB ) ) ;
xtdkm = xtdrad *(180.0*60.0/ pi) *1.852;
```

Appendix B.2: Linear transformations and correction code.

Code used for the correction, fitting and application of linear transformations to great circle segments previously identified. Modified from Andikagumi et al 2020, in order to show 'true shape' residual graphs of individual great circle segments.

```
%% INPUT
clc;
close all
close all hidden

[num,txt] = xlsread('Test.xlsx'); %Dataset Name
fprintf('Test\n\n');

lon = num(:,1);
lat = num(:,2);
vname = txt;
```

```
%annealing parameters
maxiter = 100000; %up to 10,000,000 depending on simulation time allowed

%conversion
lonr = lon .* (pi/180);
latr = lat .* (pi/180);

XA = lonr(1); YA = latr(1); %Point 1 Initial
XB = lonr(numel(lonr)); YB = latr(numel(latr)); %Point 2 Initial

XAdeg = XA * (180/pi); YAdeg = YA * (180/pi); %Point 1 & 2 for plotting purpose
XBdeg = XB * (180/pi); YBdeg = YB * (180/pi);
xlineINT = [XAdeg;XBdeg]; ylineINT = [YAdeg;YBdeg];

%% INITIAL CALCULATION

[distradAB,distkmAB] = calcdist(XA,YA,XB,YB);
[azradAB,azdegAB] = calcaz(XA,YA,XB,YB);

sumxtd = 0;
resultI = zeros (10,2);

    for i = 1 : numel(lonr)
        [distradAD(i),distkmAD(i)] = calcdist(XA,YA,lonr(i),latr(i));
```

```
        [azradAD(i),azdegAD(i)] = calcaz(XA,YA,lonr(i),latr(i));
        [xtdrad(i),xtdkm(i)] = calcxtd(distradAD(i),azradAB,azradAD(i));
        [atdrad(i),atdkm(i)] = calcatd(distradAD(i),xtdrad(i));
        sumxtd = sumxtd + (xtdkm(i)*xtdkm(i));

        resultI(i,1) = xtdkm(i);
        resultI(i,2) = atdkm(i);
    end

sumxtd = sqrt(sumxtd/numel(xtdkm));
bestxtd = sumxtd;
bestdistkm = distkmAB;

%Initial Output
result00 = ['Initial Segment Properties'];
result01 = ['Segment length (km) = ', num2str(distkmAB)];
result02 = ['Azimuth (deg) = ', num2str(azdegAB)];
result03 = ['Total Misfit (km) = ', num2str(sumxtd)];
result04 = ['XA = ', num2str(XAdeg), '; YA = ', num2str(YAdeg),';'];
result05 = ['XB = ', num2str(XBdeg), '; YB = ', num2str(YBdeg),';'];
disp(result00); disp(result01); disp(result02); disp(result03); disp(result04);
disp(result05);

fprintf('\n%-20s %10s %10s\n','Volcano','XTD','ATD');
for j = 1 : numel(lonr)
```

```
fprintf('%-20s %10.5f %10.5f \n',char(vname(j)),resultI(j,:));
end

%% SIMULATED ANNEALING

XP = XA; YP = YA; XQ = XB; YQ = YB;
XPcurr = XA; YPcurr = YA; XQcurr = XB; YQcurr = YB;
XPbest = XP; YPbest = YP; XQbest = XQ; YQbest = YQ;

%set search boundary
range = 0.5 * (pi/180);
XPmin = XP - range; XPmax = XP + range; YPmin = YP - range; YPmax = YP +
range;
XQmin = XQ - range; XQmax = XQ + range; YQmin = YQ - range; YQmax = YQ +
range;

f = waitbar(0,'Processing...','Name','Line Fitting Simulated Annealing');

for k = 1 : maxiter
    r = rand;
    if (r <= 0.25) %randomise XP
        XP = XPcurr + (rand - 0.5) * 0.001;
        XP = max([XP XPmin]); XP = min([XP XPmax]);
    elseif (r > 0.25) && (r <= 0.5) %randomise YP
        YP = YPcurr + (rand - 0.5) * 0.001;
```

```
    YP = max([YP YPmin]); YP = min([YP YPmax]);
elseif (r > 0.5) && (r <= 0.75) %randomise XQ
    XQ = XQcurr + (rand - 0.5) * 0.001;
    XQ = max([XQ XQmin]); XQ = min([XQ XQmax]);
else %randomise YQ
    YQ = YQcurr + (rand - 0.5) * 0.001;
    YQ = max([YQ YQmin]); YQ = min([YQ YQmax]);
end

[distradPQ,distkmPQ] = calcdist(XP,YP,XQ,YQ);
[azradPQ,azdegPQ] = calcaz(XP,YP,XQ,YQ);

modxtd = 0;
resultMOD = zeros (10,2);

for i = 1 : numel(lonr)
    [distradPR(i),distkmPR(i)] = calcdist(XP,YP,lonr(i),latr(i));
    [azradPR(i),azdegPR(i)] = calcaz(XP,YP,lonr(i),latr(i));
    [xtdradMOD(i),xtdkmMOD(i)] = calcxtd(distradPR(i),azradPQ,azradPR(i));
    [atdradMOD(i),atdkmMOD(i)] = calcatd(distradPR(i),xtdradMOD(i));
    modxtd = modxtd + (xtdkmMOD(i)*xtdkmMOD(i));

    resultMOD(i,1) = xtdkmMOD(i);
    resultMOD(i,2) = atdkmMOD(i);
end
```

```
modxtd = sqrt(modxtd/numel(xtdkmMOD));


if modxtd < sumxtd
    XPcurr = XP;
    YPcurr = YP;
    XQcurr = XQ;
    YQcurr = YQ;
else
    if ((rand * (sumxtd - modxtd)) < (1000 / k))
        XPcurr = XP;
        YPcurr = YP;
        XQcurr = XQ;
        YQcurr = YQ;
    end
end


if (modxtd < bestxtd)
    XPbest = XP;
    YPbest = YP;
    XQbest = XQ;
    YQbest = YQ;
    bestiter = k;
    bestxtd = modxtd;
    bestdistkm = distkmPQ;
```

```
        bestazdeg = azdegPQ;
        bestresultMOD = resultMOD;
    end
    waitbar(k/maxiter,f);
end

delete(f)

XPdeg = XPbest * (180/pi); YPdeg = YPbest * (180/pi);
XQdeg = XQbest * (180/pi); YQdeg = YQbest * (180/pi);
xlineMOD = [XPdeg;XQdeg]; ylineMOD = [YPdeg;YQdeg];

%Final Output
fprintf('\n');
result10 = ['Modified Segment Properties'];
result11 = ['Segment length (km) = ', num2str(bestdistkm)];
result12 = ['Azimuth (deg) = ', num2str(bestazdeg)];
result13 = ['Total Misfit (km) = ', num2str(bestxtd)];
result14 = ['Best Iteration = ', num2str(bestiter)];
result15 = ['XP = ', num2str(XPdeg), '; YP = ', num2str(YPdeg),';'];
result16 = ['XQ = ', num2str(XQdeg), '; YQ = ', num2str(YQdeg),';'];
disp(result10); disp(result11); disp(result12); disp(result13); disp(result14);
disp(result15); disp(result16);

fprintf('\n%-20s %10s %10s\n','Volcano','XTD','ATD');
```

```
for l = 1 : numel(lonr);
fprintf('%-20s %10.5f %10.5f \n',char(vname(l)),bestresultMOD(l,:));
end
dist = (0:7000);
x = zeros(1, 7001);

f = figure('Windowstate','maximized');
subplot(2,1,1)
hold on;
plot(lon,lat,'^r','MarkerFaceColor','red');
plot(xlineINT,ylineINT,'LineWidth',2);
plot(xlineMOD,ylineMOD,'--','LineWidth',2);
pbaspect([1 1 1]); grid on; grid minor; axis equal;
xlim([min(lon)-0.2 max(lon)+0.2]);
ylim([min(lat)-0.2 max(lat)+0.2]);
title('Line Fitting from Simulated Annealing');
xlabel('Longitude'); ylabel('Latitude');
legend('Volcano','Initial Line','Best Fit Line');
text ( lon,lat,vname,'VerticalAlignment','bottom','HorizontalAlignment','left')
hold off

%figure showing true shape of segment
subplot(2,1,2)
hold on
```

```
%plot(bestresultMOD(1:numel(vname),2),bestresultMOD(1:numel(vname),1),'^r','Mar
kerFaceColor','red');
title('True shape of Segments');
xlabel('GC Distance (km)'); ylabel('\Delta GC (km)');
plot(dist,x,'black')
xlim([min(dist) max(bestresultMOD(:,2))+10]);
ylim([min(bestresultMOD(1:numel(vname),1))-1
max(bestresultMOD(1:numel(vname),1))+1]);
legend('Volcano','Best Fit Line')

pause(1)

%f.position



function [distrad,distkm] = calcdist(XA,YA,XB,YB)  % Calculate Distance Function

s1 = (sin((YA-YB)/2))^2;
s2 = cos(YA)*cos(YB)*(sin((XA-XB)/2))^2;
distrad = 2*asin(sqrt(s1+s2));
distkm  = distrad*(180.0*60.0/pi)*1.852;

function [azrad,azdeg] = calcaz(XA,YA,XB,YB)  % Calculate Course Function
```

```
azrad = mod(atan2(sin(XA-XB)*cos(YB),cos(YA)*sin(YB)-sin(YA)*cos(YB)*cos(YA-YB)),2*pi);
azdeg = 360-(azrad*(180/pi));

function [xtdrad,xtdkm] = calcxtd(distradAD,azradAB,azradAD)  %Calculate Cross Track Distance Function

xtdrad = asin(sin(distradAD)*sin(azradAD-azradAB));
xtdkm = xtdrad*(180.0*60.0/pi)*1.852;

function [atdrad,atdkm] = calcatd(distrad,xtdrad) %Calculate Along Track Distance Function

atdrad = acos(cos(distrad)/cos(xtdrad));
atdkm = atdrad*(180.0*60.0/pi)*1.852;
```

Appendix B.3: Small circle identification code.

Code used for the identification of small circles for given segments. Taken directly from Andikagumi et al 2020.

```
% Input


clc;
close all
close all hidden


clear ;
[ num , txt , raw ] = xlsread ('Test.xlsx') ;
vlon = num (: ,1) ;
vlat = num (: ,2) ;
vname = txt(:,1) ;
nvol = numel ( vlon ) ;
lon = vlon;
lat =vlat;


% Parameters


maxiter = 200000;
minrad = 5;
maxrad = 10000;


%% Initial Process


% Convert to Radians
```

```
sumlon = 0;
sumlat = 0;

for i = 1: nvol
    vlon ( i ) = vlon ( i ) *( pi /180) ;
    vlat ( i ) = vlat ( i ) *( pi /180) ;
    sumlon = sumlon + vlon ( i ) ;
    sumlat = sumlat + vlat ( i ) ;
end

% Generate Random Parameters for Initial Small Circle

lonSC = sumlon / nvol + ( rand - 0.5) *0.1;
latSC = sumlat / nvol + ( rand - 0.5) *0.1;
radSC = rand * 50;

% Initial Current Small Circle Parameters

currlonSC = lonSC ;
currlatSC = latSC ;
currradSC = radSC ;

% Initial Best Small Circle Parameters

bestlonSC = lonSC ;
```

```
bestlatSC = latSC ;

bestradSC = radSC ;

bestiter = 0;


[ currdist , currmisfit ] = calcdist ( vlon , vlat , lonSC , latSC , radSC , nvol ) ;

[ bestdist , bestmisfit ] = calcdist ( vlon , vlat , lonSC , latSC , radSC , nvol );


% Write Initial Distance


x00 = 'Initial Small Circle ';

A = num2str (sqrt (bestdist / nvol));

x01 = ['RMS: ', A];

B = num2str ( bestlatSC * 180.0/ pi);

x02 = ['Lat: ', B ];

C = num2str ( bestlonSC * 180.0/ pi);

x03 = ['Lon: ', C ];

D = num2str ( bestradSC );

x04 = ['Rad: ', D ];


clc ; disp ( x00 ) ; disp ( x03 ) ; disp ( x02 ) ; disp ( x04 ) ; disp ( x01 ) ;


%% Simulated Annealing Loop


f = waitbar (0 ,  'Processing ... ','Name',' Small Circle Annealing Simulation') ;
```

```
for k =1: maxiter
    r = rand ;
    if ( r <= 0.33333) % randomise radius
        radSC = currradSC + ( rand - 0.5) * 5.0;
        radSC = max ([ radSC minrad ]) ;
        radSC = min ([ radSC maxrad ]) ;

    elseif ( r > 0.33333) && ( r <= 0.66667) % randomise longitude
        lonSC = currlonSC + ( rand - 0.5) * 0.01;

        if ( lonSC > 180)
        lonSC = lonSC - 360;

        elseif ( lonSC < -180)
        lonSC = lonSC + 360;

        end

    else % randomise latitude
    latSC = currlatSC + ( rand - 0.5) * 0.01;

    if ( latSC > 90)
        latSC = 180 - latSC ;

    elseif ( latSC < -90)
```

```
    latSC = ( -180) - latSC ;
end

end

[ dist , misfit ] = calcdist ( vlon , vlat , lonSC , latSC , radSC , nvol ) ;

if ( dist < currdist )
    currradSC = radSC ;
    currlonSC = lonSC ;
    currlatSC = latSC ;
    currdist = dist ;
    currmisfit = misfit ;

else
    if (( rand * ( dist - currdist ) ) < (1000 / k ) )
        currradSC = radSC ;
        currlonSC = lonSC ;
        currlatSC = latSC ;
        currdist = dist ;
        currmisfit = misfit ;
    end
end

if dist < bestdist
```

```
        bestlonSC = lonSC ;
        bestlatSC = latSC ;
        bestradSC = radSC ;
        bestdist = dist ;
        bestiter = k ;
        bestmisfit = misfit ;
    end

    waitbar ( k / maxiter , f ) ;

end

delete ( f )

x10 = 'Best Fit Small Circle ';
E = num2str ( sqrt ( bestdist / nvol ));
x11 = ['RMS: ', E ];
F = num2str( bestlatSC *180.0/ pi);
x12 = ['Lat: ', F  ];
G = num2str ( bestlonSC *180.0/ pi);
x13 = ['Lon: ', G ];
H = num2str ( bestradSC );
x14 = ['Rad: ', H ];
I = num2str ( bestiter );
x15 = ['Iteration : ', I ];
```

```
J = num2str ( nvol );
x16 = ['n Volcanoes : ', J ];

fprintf ('\n') ;
disp ( x10 ) ; disp ( x13 ) ; disp ( x12 ) ; disp ( x14 ) ; disp ( x11 ) ; disp ( x15 ) ; disp (
x16 ) ;

fprintf ('\n% -20s %10 s\n','Volcano ','XTD ') ;
for j = 1 : numel ( vlon )
fprintf ('% -20s %10.5 f\n' , char ( vname ( j ) ) , bestmisfit ( j ) ) ;
end

function [ dist , misfit ] = calcdist ( vlon , vlat , lonSC , latSC , radSC , nvol )
% Calculate Distance Function

dist = 0;
misfit = zeros ( size ( vlon ) ) ;

for j =1: nvol

vlonTemp = vlon ( j ) ;
vlatTemp = vlat ( j ) ;
s1 = (sin (( latSC - vlatTemp ) /2) ) ^2;
s2 = cos( latSC ) * cos( vlatTemp ) *( sin (( lonSC - vlonTemp ) /2) ) ^2;
d1 = 2* asin ( sqrt ( s1 + s2 ) ) ;
```

```
d = d1 *(180.0*60.0/ pi) *1.852 - radSC ;

dist = dist + d * d ;

misfit ( j ) = d ;


end
```

Appendix C: Tectonic event timings

	Start Time (Ma)	End Time (Ma)	Citation
plate motion change of the Philippine plate to become more oblique motion relative to Japan	2		1
subduction direction NW to WNW of Philippine plate	2		1

Ontong Java Plateau and Solomon Islands have hard collision	5Ma	4Ma	2
subduction ceased along the southern edge of the Solomon Sea	5Ma		3
more trench normal subduction of Philippine plate	6	2	4
Woodlark basin created from back arc spreading	6Ma	5Ma	3
Banda Sea back arc spreading ~ 6Ma and formed between 3 and 6 MA	6 MA	3 Ma	3
Australian plate subducted northward and bismarak sea was gradually formed as a back arc basin	6	4	5
Seafloor spreading at the Mariana trough commences	7Ma	0	6
Izu Bonin arc change of motion direction from its previous clockwise rotation for past ~43Ma	8Ma		7
Reversal of subduction polarity occurred and produced new subduction zone at present NBT (New Britain Trench)			2
development of the new Hebrides arc	10 Ma		3
orth Fiji Basin spreading from ~12Ma	12 Ma		3
Collision of Caroline Island Ridge causing the westward migration of southern end of Mariana arc	13Ma		7

Izu Bonin spreading decreased	14 Ma		4
ceasing of spreading in shitoku basin, Parce Vela basin and south China sea	15 Ma		4
Ayu Trough opening in the Caroline Plate	~15 Ma		3
roughly constant northward reorientation of spreading ridges?	22.5	6	8
Three separate spreading events for the creation of Cocos and Nazca tectonic plates.	A - ~23Ma; B – 19.5; C- 14.7	19.5Ma, 14.7Ma; 0	9
Solomon Sea Spreading stopped	24		3
South Fiji Basin Spreading stopped	25		3
New Guinea passive margin collided with the leading edge of the east Philippines-Halmahera-New Guinea arc system			10
development of oceanic crust in S China sea due to pull forces of subducting slabs	~32Ma		10
extrusion of indo-china	32	15	10
Caroline sea nucleated and began spreading N-S.	~36Ma		6
West Philippine stopped spreading	36Ma	30Ma	11,12
pacific Kula spreading fully ceases	41.1	40.1	13
Final India and Eurasia collision in the East of India	41.7	39.1	13
acceleration of Australia relative to Antarctica ~4x	43.4	33.7	13

Pacific plate subducted beneath the Australian plate along the western Melanesian-North Solomon Trench.	~45Ma		2
Antarctic pacific change in direction	47.3	43.4	13
rifting of south America from Antarctic peninsula and the start of the opening of the drake passage	48	45.7	13
opening of Tasman gateway?	50	46	13
change of direction of sea spreading (pacific) from ENE-WSW to E-W	51.8	45.7	13
ending of majority of spreading in Tasman sea	53.98		13
pacific-kula spreading changes direction	57.1		13
Sea floor spreading commenced at west Philippine basin	58Ma	51Ma	6

References are: 1. (Mahony et al., 2011); 2. (Liu et al., 2023) and references within; 3. (Hall, 2002); 4. (Liu et al., 2017); 5. (Holm et al., 2016); 6. (Wu et al., 2016) and references within; 7. (Miller and Kennett, 2006); 8. (Whitman et al., 1983); 9. (Meschede and Barckhausen, 2000); 10. (Hall, 1997); 11. (Sasaki et al., 2014); 12. (Deschamps and Lallemand, 2002); 13. (Gaastra et al., 2022).